UNIVERSITY OF SÃO PAULO
FACULTY OF PHILOSOPHY, SCIENCES AND LITERATURE
POSTGRADUATE IN PHYSICS APPLIED TO MEDICINE AND BIOLOGY

X-Ray Detectors Based on the Radiolytic Synthesis of Metal Nanoparticles

(Detectores de raios-X baseados na síntese radiolítica de nanopartículas metálicas)

LUIZ HENRIQUE DOS SANTOS NUNES

Dissertation presented to Faculty of Philosophy, Sciences and Literature (FFCLRP) from the University of São Paulo (USP), as part of the requirements to hold the Master of Science degree.

Ribeirão Preto–SP

2022

LUIZ HENRIQUE DOS SANTOS NUNES

X-Ray Detectors Based on the Radiolytic Synthesis of Metal Nanoparticles

Dissertation presented to Faculty of Philosophy, Sciences and Literature (FFCLRP) from the University of São Paulo (USP), as part of the requirements to hold the Master of Science degree.

Field of Study:
Physics Applied to Medicine and Biology.

Supervisor:
Éder José Guidelli

Corrected Version

The original version is found at FFCLRP/USP.

Ribeirão Preto–SP

2022

Luiz Henrique dos Santos Nunes
X-Ray Detectors Based on the Radiolytic Synthesis of Metal Nanoparticles. Ribeirão Preto–SP, 2022.
91p. : il.; 30 cm.

Dissertação apresentada à Faculdade de Filosofia, Ciências e Letras
de Ribeirão Preto da USP, como parte das exigências para
a obtenção do título de Mestre em Ciências,
Área: Física Aplicada à Medicina e Biologia.
Supervisor: Éder José Guidelli

1. Dosimetry. 2. Nanoparticles. 3. Plasmons.

Luiz Henrique dos Santos Nunes

X-Ray Detectors Based on the Radiolytic Synthesis of Metal Nanoparticles

Dissertation presented to Faculty of Philosophy, Sciences and Literature (FFCLRP) from the University of São Paulo (USP), as part of the requirements to hold the Master of Science degree.

Ribeirão Preto–SP, 21 de novembro de 2018:

Supervisor:
Éder J. Guidelli

Professor
Convidado 1

Professor
Convidado 2

Ribeirão Preto–SP
2022

Agradecimentos

Agradeço a todos que contribuíram de alguma forma para a realização deste projeto, das mais variadas formas, por sempre me lembrarem que a ciência de forma alguma é individual.

Devo eterna gratidão ao meu orientador **Prof. Dr. Éder José Guidelli**, por me aceitar como aluno e confiar a mim um projeto. Mais ainda pelas várias oportunidades, como orientador e como professor, que eu recebi ao longo desses últimos semestres. Não tenho dúvida de que foram transformadoras.

Aos meus colegas de bancada, de laboratório ou mesmo da pausa do café, eu agradeço por toda a disponibilidade para ajudar e pela paciência de me aturar durante a realização do projeto. Meu muito obrigado a **Bassam Bachour**, **Mileni Isikawa**, **Jeferson Oliveira**, **Iara Lima**, **Natasha Policei**, **Gabriel Lobo**, **Mariana Chaves** e a todos os que conviveram comigo (e me impactaram) de alguma forma

Aos técnicos e funcionários do Departamento de Física, que sempre foram solícitos às minhas necessidades, e pacientes às minhas dúvidas, agradeço a todo o suporte prestado, em especial nas condições a que estivemos sujeitos desde a pandemia.

Por último, eu devo minha honra e gratidão aos meus pais **José Alcides Aquino Nunes** e **Sandra Regina dos Santos Nunes**, que, mesmo sendo tão distantes da Física, me forneceram a principal base para que eu pudesse me aventurar nessas águas: a de que a educação e a disciplina são a principal ferramenta de que podemos dispor. Sem eles, nenhum passo dado até aqui seria possível.

LHN

"As palavras são testemunhas que muitas vezes
falam mais alto que os documentos"
(Eric Hobsbawm, A era das revoluções)

Resumo

NUNES, L. H. S. **Detectores de raios-X baseados na síntese radiolítica de nanopartículas metálicas**. 2022. 103p. Dissertação de Mestrado (Programa de Pós-Graduação em Física Aplicada à Medicina e Biologia) - Faculdade de Filosofia, Ciências e Letras, Universidade de São Paulo, Ribeirão Preto - SP, 2022.

Feixes de raios-X são largamente aplicados em diagnóstico e tratamento, uma vez que suas propriedades relacionadas à interação com tecidos no corpo são desejáveis para imagens e radioterapia. Nos dois casos, a medida da dose é de grande importância para chegar à melhor eficiência na aplicação, evitando efeitos indesejáveis decorrentes da exposição a altas doses. Vários dosímetros têm sido desenvolvidos para atender a esse requisito. Nesse contexto, dosímetros baseados em nanopartículas são uma boa alternativa para a medida de dose, uma vez que apresentam vantagens como equivalência a tecidos biológicos e instrumentação simples. A ideia básica de um dosímetro baseado em nanopartículas é sintetizá-las através da irradiação, para possibilitar a correlação entre a dose e a intensidade da banda de absorção das nanopartículas, gerada pelo fenômeno de LSPR.

Nessa dissertação, alguns dosímetros baseados na síntese radiolítica de nanopartículas de prata e ouro foram desenvolvidos, para possibilitar a medida de baixas doses envolvidas em radioterapia e imagens de raios-X. A síntese foi realizada por differentes métodos combinando uma reação química com a irradiação, para formar as nanopartículas e correlacionar sua concentração com a dose absorvida. As nanopartículas de prata produziram um dosímetro multimodal baseado na síntese microfluídica de AgNP, o que permitiu a detecção da dose por meio de spectroscopia UV-visível e de fluorescência, com sensibilidades de 9.2 10^{-3} e 3.4 a.u./Gy para doses de até 0.75 Gy, constituindo resultados excepcionais comparados à literatura. Além disso, essa técnica permitiu estudos sobre a formação das nanopartículas, incluindo o controle dos processos de nucleação e crescimento. O dosímetro baseado em nanopartículas de ouro (AuNP) foi efetivo para detecção de doses até 10 Gy. O estudo da influência dos parâmetros químicos e radiolíticos da síntese confirmou a geração de sementes por templating, com o subsequente crescimento sendo relacionado à irradiação, produzindo assim um dosímetro com sensitividade 0.07 a.u./Gy. A análise do sinal de UV-vis para diferentes energias mostro uque, para doses mais altas, a nucleação e formação de novas nanopartículas é favorecida em relação ao crescimento das já existentes. Além disso, a distribuição de tamanho se mostrou uma forma alternativa de medir a dose, mesmo que sua influência seja restrita a feixes de altas energias.

Palavras-chave: dosimetria. nanopartículas. plasmons.

Abstract

NUNES, L. H. S. **X-Ray Detectors Based on the Radiolytic Synthesis of Metal Nanoparticles**. 2022. 103p. Thesis (Master Degree - Postgraduate program in Physics Applied to Medicine and Biology) - Faculty of Philosophy, Science and Letters, University of São Paulo, Ribeirão Preto - SP, 2022.

X-ray beams are widely applied to diagnosis and treatment, since their properties related to the interaction with the tissues in the body are desirable to imaging and radiation therapy. For both applications, the dose assessment is of great importance, in order to achieve the best efficiency in the imaging/therapy avoiding the undesirable effects of the exposition to high doses. A lot of dosimeters have been developed to attend this requirement. In this context, the nanoparticle-based dosimeters are a good alternative to dose assessment, since they present advantages as tissue equivalence and simple instrumentation requirements. The main idea of a nanoparticle-based dosimeter is to synthesize the nanoparticle upon the irradiation, in order to correlate the dose with the absorbance band intensity of the nanoparticles, due to the LSPR phenomena.

In this thesis, some dosimeters based on the radiolytic synthesis of silver and gold nanoparticles were developed, in order to measure the low doses involved in the radiation imaging and therapy with x-rays. The synthesis was carried out by different methods combining a chemical reduction with an irradiation procedure in order to successfully form the nanoparticles and correlate their concentration to the absorbed dose. The silver nanoparticles generated a multimodal dosimeter based on microfluidic synthesis of AgNP, that allows the detection of the dose by UV-vis and fluorescence spectroscopies, with sensitivities of 9.2 10^{-3} and 3.4 a.u./Gy for doses up to 0.75 Gy, which are remarkable results compared to the literature. Besides that, this technique provides some insights about the nanoparticles formation, including the control of the nucleation and growth processes. The dosimeter based on gold nanoparticles (AuNP) was found to be effective to assess doses up to 10 Gy. The study of the chemical and radiolytic parameters of the synthesis confirmed the generation of seeds by templating, with a further growth related to the irradiation, leading to a dosimeter with sensitivity of 0.07 a.u./Gy. The analysis of the UV-vis signal for different energies spotlighted that, at higher doses, the nucleation and formation of more nanoparticles is favored over the growth. Moreover, the size distribution was found to be an alternative way to analyze the dose, but its influence is limited to higher energies, in the order of 160 kVp beam quality.

Keywords: dosimetry. nanoparticles. plasmons.

List of figures

List of tables

List of abbreviations and acronyms

AA	Ascorbic acid.
ABS	Absorption spectroscopy.
AgNC	Silver nanoclusters.
AgNP	Silver nanoparticles.
AuNP	Gold nanoparticles.
CTAB	Bromide cetiltrimetilamonium.
DLS	Dynamic light scattering.
DNA	Deoxyribonucleic acid.
FLS	Fluorescence spectroscopy.
FWHM	Full width at half maximum.
HVL	Half value layer.
LSPR	Localized surface plasmon resonance.
MDC	Minimum detectable change.
MDD	Minimum detectable dose.
MNP	Metal nanoparticle
NC	Nanocluster.
PSD	Particle size distribution.
SEM	Standard error measurement.
TEM	Transmission electron microscopy.
UV-vis	UV-visible spectroscopy.

List of symbols

A	Particle area.
Ag^n	n-valent silver ion.
$AgNO_3$	Silver nitrate.
Au^n	n-valent gold ion.
c	Light speed.
c_{crit}	Critic concentration.
c_∞	Equilibrium concentration.
ϵ	Molar absorptivity.
ε_m	Surroundings dielectric function.
$\varepsilon(\omega)$	Nanoparticle dielectric function.
$\varepsilon_1(\omega)$	Nanoparticle real dielectric function.
$\varepsilon_2(\omega)$	Nanoparticle imaginary dielectric function.
Gy	Gray.
$HAuCl_4$	Chloroauric acid.
$I_0(\omega)$	Light original intensity.
$I(\omega)$	Light attenuated intensity.
κ	Wavenumber module.
L	Optical length.
λ	Wavelength.
Na_3Ct	Sodium citrate.
R	Particle radius.
$\sigma_{ext}(\omega)$	Extinction coefficient.
μ	Linear attenuation coefficient.
μ/ρ	Mass attenuation coefficient.

V_0	Particle volume.
$\chi^{DS}(\omega)$	Drude-Sommerfeld electric susceptibility.
$\chi^{IB}(\omega)$	Interband transition electric susceptibility.

Sumário

1

Introduction

Since the diagnostic and treatment employing ionizing radiation were developed, x-rays tubes operating with voltages in the range of tens of kilovolts (kV), sometimes refereed as orthovoltage tubes, have been used for imaging and therapy purposes (4). Nowadays, kV x-rays tubes in the range of 50 to 300 kVp are widely applied on superficial and intraoperative radiation therapy (5). Moreover, recent techniques are being developed on deeper treatments, including the use of enhancement agents and more sophisticated sources (6).

The main goal in all radiological treatments is to achieve the greatest efficacy with the lowest damage, which is possible by controlling the dose absorbed by the tissue (7). In all the applications, and especially in the therapeutic ones, the control of the dose given to the patient is, therefore, of vital importance. To overcome this necessity, several devices can be used to monitor and control the dose on a patient, the so-called dosimeters (8). All of the dosimeters are based on the same idea: a measurable change in a physical or chemical property of a given material caused by its interaction with the ionizing radiation (9, 10).

In this context, many dosimeters have been developed in the last decades. The ion chambers became the most common approach and they turned to the main method, used as a reference not only for the characterization of x-rays and gamma-rays sources but also for the calibration of other dosimeters. However, as they need a high voltage power supply to work, they are avoided for *in vivo* applications, which includes the therapy procedures (11, 12). The dosimeters based on field effect transistors present this limitation as well. Solid state detectors can also be used for *in vivo* applications but requires constant calibrations. Thus, many researches focus on developing new dosimeters with the required properties to be employed in the several therapeutic and/or diagnostic techniques . These devices must be simple and employable to the doses commonly used in radiation therapy.

1.1 Nanoparticles

The nanoparticles consists of structures with dimensions in the range from 1 to 100 nm, that present unique properties differing both from atomic/molecular entities and the bulk materials. These properties allow the nanoparticles to be applied in a lot of fields, such as the food industry, electronics, and biomedicine. One of the wider applications of nanoparticles in medicine is for sensing devices. The changes of a given nanoparticle property upon a chemical or physical stimulus is the basis for the sensing applications. For a nanoparticle-based dosimeter, one possible approach is to synthesize the nanoparticles upon irradiation with ionizing radiation. The metal nanoparticles (MNPs), based on transition metals, like Au, Ag, Cu or Pt can be formed in this process. As the nanoparticles are synthesized, their concentration increases and the extinction coefficient, associated with the localized surface plasmon resonance (LSPR), raises. Therefore, the detection of an absorbance band is an indication of the dose absorbed by the dispersion.

1.2 Overview of the thesis

The aim of the work was to develop dosimeters based on the optical properties of metal nanoparticles. Synthesis of silver and gold nanoparticles were developed combining chemical and radiolytic steps. The absorbance and the fluorescence emission were studied and correlated with the absorbed dose. Also, the particle size was analyzed via dynamic light scattering and transmission electron microscopy.

The results for silver nanoparticles (AgNP) are presented and analyzed in Chapter 4. It covers the development of synthetic routes to obtain the AgNP and the subsequent optimization of the results to find the best parameters dosimetric applications. The applicability of a multimodal dosimetry based on these nanoparticles was presented and discussed. The gold nanoparticles (AuNP) were studied based on a well-controlled radiolytic synthesis, as presented in the Chapter 5. The gold nanoparticles were studied in order to infer about the absorbed dose in terms of absorbance and particle size.

2

Theoretical aspects

This chapter will discuss the synthesis and properties of metal nanoparticles. A general overview about nanoparticles will be shown and the main synthesis routes for our applications will be presented and detailed. After that, the properties of noble metal nanoparticles will be presented. Finally, the chapter will discuss about how these properties could be applied for dosimetric purposes by correlating the absorbed dose with the signal produced on UV-vis Absorbance Spectroscopy (ABS), Dynamic Light Scattering (DLS) and Fluorescence Spectroscopy (FLS).

2.1 Nanoparticles synthesis

There are many routes to produce nanostructures, including chemical reduction (13), sol-gel process (14), nanolitography (15, 16) and vapour deposition (17). These techniques are commonly divided in two groups, depicted in Figure 1, according to the size of primary and intermediate materials. The first group is called *top-down*. The top-down techniques consist in routes in which microcrystalline materials are fragmented to yield a nanocrystalline material. These approaches are easily scaled-up but the size distribution produced in a top-down route usually lacks uniformity, as the synthesis cannot be controlled to produce narrow size distributions (18). On the other hand, the *bottom-up* methods are techniques in which the atoms, ions or molecules of a compound are used as the base of the nanostructures. These entities are stimulated to bond to each other, and coalesce, producing the nanoparticles. The bottom-up approaches are controllable and can produce particles with defined size. Also, as these methods are based on application of different kind of energies (magnetic, mechanical, thermal, etc.) or chemical reactions, the nanoparticles shape, composition and properties can be precisely controlled (1).

The bottom-up approaches are based on the growing of nanoparticles from a precursor solution. This process occurs basically in three steps (19, 20). On the first step, the ionic entities are reduced, leading to the formation of monomers. Then, the monomers

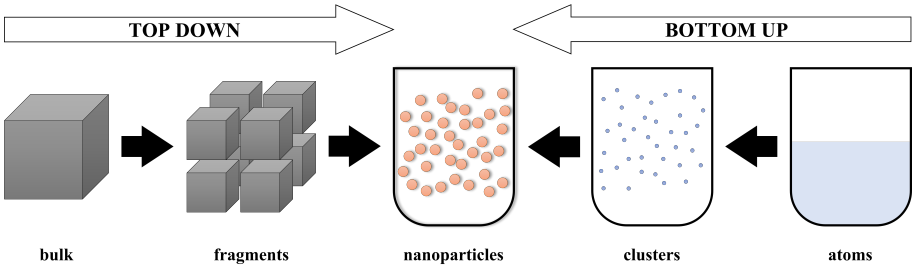

Figure 1 – Types of methods for nanoparticle production: Top-down and Bottom-up. Adapted from (1)

bind to each other, forming small particles, called nucleus. These nuclei act as seeds to the growth process. On the last step, the formed nuclei attract the monomers to the surface, growing into nanoparticles. The concentration of the species is described by the LaMer diagram, as presented in Figure 2. There is a huge increasing on nuclei quantity until the critical concentration (c_{crit}) is achieved. Then, as the nuclei agglomerate and form the nanoparticles, their concentration reduces until reaching an equilibrium value (c_{∞}) (2).

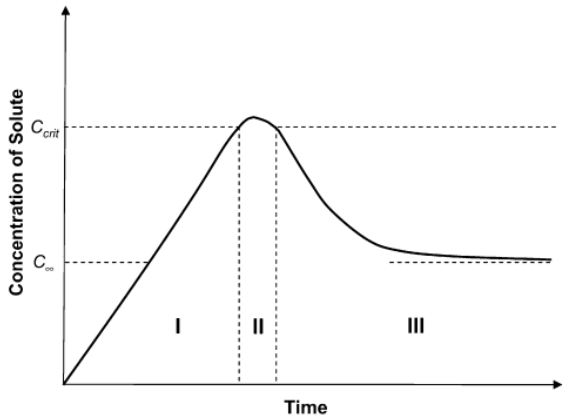

Figure 2 – LaMer diagram, presenting the two steps of nanoparticles synthesis in terms of solute concentration. Adapted from (2)

The nucleation and growth of the nanoparticles can be done by a lot of methods (some of them cited earlier). In all these approaches, a stimulus is used to promote the reduction of the ions on solution. The stimulus can be a chemical reaction (21), an electric signal (22), a laser irradiation (23) or ionizing radiation (24). The energy or charge provided by these stimuli is capable of reducing the metal ions and promote the nanoparticle formation.

2.1.1 Chemical synthesis

The metal nanoparticles synthesis by chemical routes occurs through a redox reaction. The ions of the reducing agent interact with the cations, leading them to their neutral form, as shown in equation 2.1 (24). As the neutral atoms are produced, they tend to form clusters of units to tens of atoms. If a sufficient quantity of clusters is formed, they can grow into nanoparticles by attracting more neutral atoms or aggregating with other clusters, as presented on equation 2.2.

$$M^+ + R^- \rightarrow M^0 \tag{2.1}$$

$$\begin{aligned} M^0 + M^0 &\rightarrow M_2 \\ M^0 + M^+ &\rightarrow M_2^+ \\ M_n + M^0 &\rightarrow M_{n+1} \end{aligned} \tag{2.2}$$

One of the main methods for nanoparticles synthesis by chemical reduction is the one developed by Turkevich (25). The sodium citrate is used both as a reducing and capping agent, responsible for the reduction of the metal ions of gold (Au^+) or silver (Ag^+), which came from the respective diluted metal salts. According to Pillai et al. (26), the formation of silver clusters occurs in the following steps, shown in equation 2.3: the silver ions are reduced, the neutral atoms form dimmers which, in turn, form complexes with the citrate.

$$\begin{aligned} Ag^+ + e_{aq}^- \rightarrow Ag^0 \rightarrow (Ag)_2^+ \xrightarrow{citrate} [(Ag)_2^+ ... (citrate)^-] \\ (Ag)_2^+ ... (citrate)^- \rightarrow \textit{citrate capped nanocluster} \end{aligned} \tag{2.3}$$

For gold nanoparticles synthesis, a common method works through the reduction of chloroauric acid ($HAuCl_4$). This precursor generates gold trivalent ions (Au^{+3}), which can be reduced to Au^0 by a chemical reaction, as first presented by Turkevich et al. in 1951 (25). Some of these methods are carried our direct in liquid-phase (27). Other ones are made using a structure to guide the reaction properly (28). Pushpavanam et al. have studied a method in which the cetyltrimethylammonium bromide (CTAB) is used as a template for the growth of the nanoparticles. One of the properties of that lipid is binding to specific planes of gold crystal (specially (111) plane). This allows to the crystal to grow in different directions (29), producing anisotropic nanoparticles. Our synthesis was inspired in this work.

2.1.2 Radiolytic synthesis

The synthesis of metallic nanoparticles can be carried out by an irradiation process instead of a chemical reaction. The ion reduction, in this case, is provided by the ionizing radiation itself (30). As the photons hit the solution, they react with the solvent (in most cases, the water), producing the so-called radiolytic ions, such as hydrated electrons (e_{aq}) or hydrogen and hydroxyl radicals (31). Some of these species act as a reducing agent themselves, leading the metallic ions distributed on solution to the neutral form. Therefore, the radiation creates the reducing agents (R^-) on Equation 2.1 and leads to the growth, as shown in Equation 2.2. According to the dose absorbed by the solution, a control of the synthesis and the concentration of the nanoparticles could be expected (24, 32). The whole process is summarized in Equation 2.4

$$\begin{aligned} H_2O &\xrightarrow{kV} H\bullet + H_3O^+ + OH\bullet \\ (H\bullet + H_3O^+ + OH\bullet) + Ag^+ &\rightarrow Ag_0 \\ nAg_0 &\xrightarrow{growth} AgNP \end{aligned} \tag{2.4}$$

The radiolytic route presents some advantages among the reduction methods. First of all, as the pressure and temperature are not major factors, the synthesis can be carried with ambient conditions for pressure and temperature with high reproducibility (33). Moreover, in absence of oxygen, the main reducing agent in this case is the solvated electron generated during the irradiation process, which has a very negative redox potential (34), enabling the reduction of the metal ion to the zero valence and, consequently, leading to the formation of highly dispersed nanoparticles (35). Also, by controlling both adsorbed dose and dose rate, it is possible to control the size of the produced nanoparticles (36). Therefore, this radiolytic approach had been proved to be an efficient and low-cost method to synthesize nanoparticles (36, 37).

2.1.3 Microfluidic synthesis

The microfluidic approaches are those based on the use of microfluidic reactors, which are devices built by using pieces on the micrometer scale. The main idea on using a microreactor is to carefully control mass and energy transfers inside the system (38). Their size leads to a high surface-to-volume ratio (for a cylindrical tube, this ratio is 2/r, with r being the radius of the tube), which enables a high heat transfer. Therefore, a microfluidic device could be used to control both the heat and the mass transfer during the reaction (39).

The main advantage of these routes is that the fine control of the synthesis parameters lead to the control and reproducibility of the nanoparticles (40). Compared to conventional batch methods, the microfluidic approach produce nanoparticles with smaller average size (due to the rapid reaction) (41) and lower polydispersity (due to the control of synthesis parameters) (42). As a consequence, not only the size of the nanoparticle is much more controlled but also its crystal structure (43). This approach is used to synthesize noble metal nanoparticles so far (44, 45).

2.1.4 Combining chemical and radiolytic approaches

As the advantages of chemical and radiolytic approaches were describe in the previous sections, an integrated synthesis method was developed aiming to use these advantages, by applying both strategies combined. The chemical step, in this case, is able to produce the seeds that would grow into nanoparticles in the radiolytic step.

As discussed earlier, the citrate reduction method is able to produce capped nanoclusters with a relatively small quantity of atoms. If this approach is used in the microfluidic model, the size and shape of these clusters could be controlled and then, with an x-ray or γ-ray source, they could grow into nanoparticles, as the radiation reduces the ions. The silver nanoparticles produced on this project following this method are relatively simple to produce, as the precursor generates ions with +1 valence. The reduction is easily carried by the radiolytic species produced in solution.

The combination of the microfluidic and the radiolytic approaches could be a great option to synthesize nanoparticles that can be useful for dosimetry. The former technique can control the seeds formed and limit the reactant consumption and the latter can generate the nanoparticles in a radiation dose dependent way, which would allow applications in dosimetry.

The synthesis of gold nanoparticles is more complicated, as the precursor (chloroauric acid) produces trivalent gold ions (Au^{+3}), which are not easily reduced to Au^0 (46), requiring several chemical steps to reduce the trivalent ions to their monovalent form (Au^{+1}), which has a lower reduction potential and can be reduced to the neutral form with just a single electron (47). As it happens, the nanoparticles grow from the neutral atoms.

The radiolytic synthesis of gold nanoparticles using CTAB as a template can be summarized as follows: when the gold precursor is diluted, H^+ and $AuCl_4^-$ ions are generated (Equation 2.5). As the CTAB is added to the reaction medium, the $AuCl_4^-$ is converted to $AuBr_4^-$ in a ion exchange process (48). This leads to the formation of [CTA]-[$AuBr_4$] complexes (Equation 2.6) (49). Finally, a reducing agent (in our case the ascorbic acid) is added to the solution and the gold ion is reduced to Au^{+1}. In other words,

the complex is modified to [CTA]-[$AuBr_2$] (Equation 2.7) (50, 49). Finally, the gold is reduced to its neutral form through the irradiation step (Equation 2.8). As the gold atoms are formed, they coalesce into nanoparticles, as represented on Equation 2.2.

$$HAuCl_4 \xrightarrow{dilution} H^+ + AuCl_4^- \tag{2.5}$$

$$AuCl_4^- + 4\ CTAB \rightarrow [CTA]^+ - AuBr_4^- + 4\ Cl^- + 3\ CTA^+ \tag{2.6}$$

$$CTA^+ - AuBr_4^- + C_6H_8O_6 \rightarrow CTA^+ - AuBr_2^- + C_6H_8O_6 + 2\ H^+ + 2\ Br^- \tag{2.7}$$

$$CTA^+ - AuBr_2^- \xrightarrow{X-ray} Au_0 + CTA^+ + 2\ Br^- \tag{2.8}$$

2.2 Metal nanoparticles properties

Once they are synthesized, the nanoparticles can be detected in solution either by electron microscopy, in which we can - literally - see them, or by UV-visible spectroscopy. The last one is possible since the metal nanoparticles present a property called localized surface plasmon resonance (LSPR), that occurs only for nanostructures (51).

2.2.1 Localized Surface Plasmon Resonance (LSPR)

The localized surface plasmon resonance (LSPR) effect is what give color to nanoparticles solutions and allow us to see their formation on naked eye. The LSPR occurs due to the collective oscillation of the electrons on the nanoparticles surface. Therefore, the LSPR effect occurs due to the coherent oscillation of the plasmons in a nanoparticle (1, 51). It was mathematically described by Gustav Mie in 1908 (52), who solved the Maxwell equations considering a spherical metal particle smaller than the visible light wavelength interacting with an incident radiation. The model is described below (1, 51).

Consider a light wave in the UV-visible range with a wavelength λ interacting with a metal particle of radius R much smaller than the light wavelength ($2R \ll \lambda$), as presented in Figure 3. Both the particle and the surrounding medium are supposed to be homogeneous and well represented by their bulk optical dielectric functions, $\varepsilon(\omega)$ and ε_m, respectively, which are independent of the particle size (51, 53). As the particle interacts with the light, the electron cloud of the metallic cluster oscillates with a frequency

which depends on the dielectric functions. For noble metals, $\varepsilon(\omega)$ is governed both by the collective oscillation of free electrons in the conduction band and/or interband transitions (1).

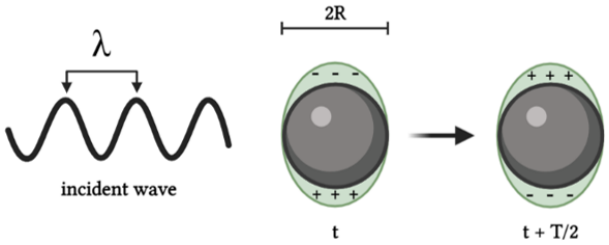

Figure 3 – Localized surface plasmon resonance (SPR) phenomena. *Created in BioRender.com*

The first contribution is described by the Drude-Sommerfeld model, which express the effect of n free electrons per unit volume oscillating by the external field influence. The contribution of this phenomena is expressed in terms of the electric susceptibility χ^{DS}. The electrons in deeper levels contribute to the dielectric function giving an additive contribution χ^{IB} to the susceptibility, due to the effect of their interband transitions (54). In that way, the value of the dielectric function can be expressed as $\varepsilon(\omega) = 1 + \chi^{DS}(\omega) + \chi^{IB}(\omega)$. Both contributions add complex quantities to the dielectric function, which can thus be written as $\varepsilon(\omega) = \varepsilon_1(\omega) + i \cdot \varepsilon_2(\omega)$ (1, 54).

When the external light (i.e. the external field) reaches the particle, it can interact with the free electron cloud, especially the ones on particle surface. Consequently, when the light has a frequency equal to ω_{MAX}, it is found in resonance with the electron cloud and interact with it in a constructive interference The plasmons, at this condition, strongly absorb and/or scatter the light. This phenomenon is called *Localized surface Plasmon Resonance* (LSPR) (51, 54).

The LSPR phenomena can be described in terms of the extinction coefficient of the light, $\sigma_{ext}(\omega)$, which describes, based on particle and medium characteristics, the capability of the particle to absorb and scatter the incident light. As the particle is smaller than the wavelength of the light ($2R \ll \lambda$), it is possible to consider that the system is in the so-called *quasi-static regime*. In this condition, multipoles oscillations can be eliminated, accounting only to the dipole one (1). In this case, the value of $\sigma_{ext}(\omega)$ can be expressed by the Equation 2.9, in which $\varepsilon(\omega) = \varepsilon_1(\omega) + i \cdot \varepsilon_2(\omega)$ is the complex dielectric function of the particle, ε_m denotes the dielectric function of the medium, $V_0 = (4\pi/3)R^3$ is the particle volume and $|\kappa| = \omega/c$ is the wavenumber module of the light (1, 54).

$$\sigma_{ext}(\omega) = 9\frac{\omega}{c}\varepsilon_m^{3/2}V_0\frac{\varepsilon_2(\omega)}{[\varepsilon_1(\omega) + 2\varepsilon_m]^2 + \varepsilon_2(\omega)^2} \tag{2.9}$$

According to Equation 2.9, the value of $\sigma_{ext}(\omega)$ is maximum if $\varepsilon_1(\omega) = -2 \cdot \varepsilon_m$, in

case of $\varepsilon_2(\omega)$ being sufficiently small or independent to ω, which is valid for the majority of monovalent metals (1). When that condition is satisfied, the extinction coefficient will be maximum and, in a spectral analysis, will be seen as a peak in a spectrum obtained by electronic spectroscopy in the UV-visible range, which corresponds to the SPR absorption peak (54, 55).

2.2.2 Fluorescence from very small metal nanoparticles

The metal nanoparticles, in general, present the LSPR as the most noticeable optical property. However, if they are sufficiently small (smaller than 2 nm), they are in the nanocluster range (56). The nanoclusters (NCs) could be seen as an intermediate state between metal molecules and nanoparticles (57). Due to their limited size, these structures present unique properties, such as molecular-like gaps (58), relatively strong photoluminescence (59) and catalytic properties (60). For imaging and sensing purposes, the most interesting property is the fluorescence in the visible or infrared regions (61, 62). In fact, the wavelength in which the emission peak occurs depends not only on the excitation energy but also on the characteristics of the NCs, such as size, shape, composition and ligands used for capping (63).

The origin of fluorescence from NCs is not fully understood, as it varies according to the components of the clusters (57). There are two main accepted explanation to this phenomenon. The first one relies on the size of the particles. If they are small enough, the energy states on the metal core could achieve some quantization state, due to the small quantity of interacting atoms (64, 65). Therefore, the fluorescence occurs due to molecular transitions in the core (66). The second explanation is based on the interaction of the core with the capping agent in the shell. As a consequence, the fluorescence changes for each capping agent, as their own energy states are different (67, 68).

The main problem for metal NCs, especially silver, is that these structures are very unstable (56), easily coalescing into nanoparticles (69). To overcome this disadvantage, many routes for synthesis of nanoclusters employs organic molecules as capping agents or templates for the growth, as charged polymer molecules (70), proteins (71), and DNA (72). As discussed earlier, the use of a given molecule leads to changes on synthesis process and, consequently, impact the size and shape of the produced nanoclusters. Thus, with the same core material, it is possible to achieve nanoclusters with different emission frequencies (67).

2.3 Nanoparticle-based dosimeters

The dosimeters based on nanoparticles synthesis relate the amount of particles produced with the radiation dose absorbed by the precursor solution. Alternatively, it could be possible to study the influence of dose on nanoparticles characteristics, such as size and shape, for instance, and develop a dosimeter based on the dose-dependent size and morphological variations. In this work, we have investigated the possibility of three different characterization techniques to infer about the absorbed dose by the colloidal dispersion: UV-vis and florescence spectroscopy and dynamic light scattering (DLS).

2.3.1 Dosimeter based on UV-vis spectroscopy (ABS)

When the light hits a material, the effects can be divided into three categories: absorption, transmission, and scattering. The first one occurs if the material absorbs the energy of the incident photon. The scattering effect happens when the light direction is modified by the interaction with the matter. If no significant interaction occurs, the light is transmitted (73, 74). The proportion in which each effect occurs depends on the nanoparticles properties (75, 76).

It is possible to determine the amount of light transmitted or absorbed by a material by illuminating a sample with a known intensity $I_0(\omega)$ and measuring the light intensity $I(\omega)$ after passing through the sample, as presented in Figure 4 (77). Both intensities are represented as a function of their frequency ω. In an absorption spectrometer, a combination of a gas light source and a prism allows the scanning of the transmitted light with ultraviolet and visible frequencies (78).

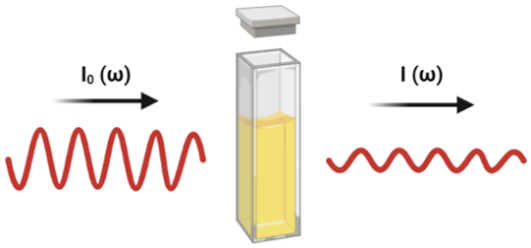

Figure 4 – Scheme of absorption spectroscopy. *Created in BioRender.com*

The absorbance of the given sample can be calculated by the equation 2.10. Also, its value can be related by the Lambert-Beer's Law, presented in Equation 2.11. According to the equation, the absorbance is proportional to the concentration c of the material and the length L of the sample, which is, for a liquid, the size of the sample cell. The quantity

ϵ is called *molar absorptivity* and its value is characteristic for each material, independent of the samples size or concentration (77, 78).

$$A = log_{10}\left(\frac{I_0(\omega)}{I(\omega)}\right) \tag{2.10}$$

$$A = c \cdot L \cdot \epsilon \tag{2.11}$$

When the metal nanoparticles are present in solution, an absorbance peak centered on LSPR frequency appears in the spectrum. As the concentration increases, the peak becomes more intense (79). Due to this relationship, a dosimeter based on the LSPR peak intensity (absorbance) in a UV-vis spectrum is possible. In fact, many authors have studied this kind of dosimeter, which can be understood as a variation of the Fricke Dosimeter (24, 32, 50)

However, this approach for metal nanoparticles dosimeter is limited because the LSPR peak intensity is dependent not only on nanoparticles concentration but also on their size, shape and composition, including the precursor metal salt and the agents used to reduce and stabilize the particles (80). Therefore, this approach produces a *relative* dosimeter, i.e., a calibration curve of dose and LSPR peak intensity is required.

2.3.2 Dosimeter based on fluorescence spectroscopy (FLS)

Before the light get absorbed by a material, they interact in a way that the photons have their paths deflected, one or multiple times. This event, called "light scattering", is responsible for the possibility of detection of the scattered light in several directions. This means that it is possible to separate this signal from the absorption, just by choosing a different angle for detection. As the previous phenomena, the scattering is influenced by the material itself and by the wavelength (or the frequency) of the incident light, providing specific information about the material, like a fingerprint.

Besides the light interactions with matter, the fluorescence is the one characterized by the absorption of the incident photon by an atom or a molecule (or a nanoparticle) followed by the transition of the entity to an excited state. When the relaxation occurs, and the molecule returns to the fundamental state, a scattered photon is emitted. This photon generally has just a fraction of energy of the incident one, which means that its characteristic wavelength is greater than the original photon. Figure 5 summarizes this process.

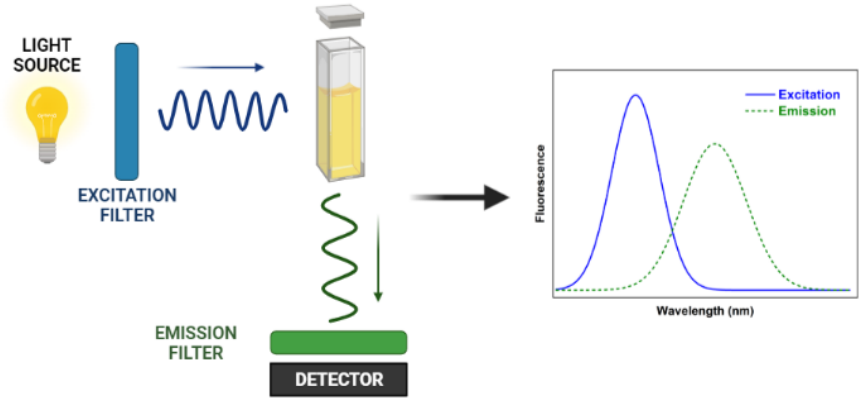

Figure 5 – Scheme of a fluorescence spectroscopy, in which the sample is excited (continuous line) and emmits with higher wavelengths (dash lines)

The wavelength in which the emission spectra is centered provides information about the nature of the studied entity. As discussed, it depends on the excitation spectra as well as on the materials preparation. The intensity of the band in the emission spectra gives information about the amount of particles present in solution. For our dosimetric purposes, it is the most interesting value.

However, the same limitation present on the absorption spectroscopy discussion is valid here: the size, shape, and composition of the nanoparticles influence on the result, which means that the results are valid specifically for our synthesis, requiring a calibration in relation to a standard dosimetric method.

3

Methodology

3.1 Silver nanoparticles synthesis

3.1.1 Synthesis without heating

The silver nanoparticles were produced following the citrate method. Silver nitrate ($AgNO_3$) was used as the precursor and the trisodium citrate ($Na_3C_6H_5O_7$, abbreviated as Na_3Ct) was used as the reducing agent. For the first experiments, 50 mL of a 1 mmol/L $AgNO_3$ was mixed with 1.0 mL of a solution of Na_3Ct in a concentration of 1% in weight, following the method proposed in (24). The mixture was prepared at room temperature, under stirring. Then, the solution was divided in 1.5 mL eppendorfs and irradiated with x-rays. The irradiation was performed on a Magnum X-ray source operating with 48 kVp and 0.2 mA, leading an x-ray beam with 10 keV effective energy. In this approach, three samples were not irradiated (0 Gy) and three other ones received a 50 Gy dose, with 2.054 Gy/min dose rate.

Nanoparticles were synthesized with varying concentrations of reactants to verify their influence on the nanoparticles properties. Table 1 presents the employed concentrations. These values were also used on the following experiments, in which the influence of a heating process was studied.

Table 1 – Precursor solutions for silver nanoparticles synthesis

Dispersion	$[AgNO_3]$ **(mmol.L^{-1})**	$[Na_3Ct]$ **(% wt)**
1	1	1%
2	1	5%
3	2	5%

3.1.2 Synthesis with conventional heating

The same reactants used in the previous section and the same concentrations presented in Table 1 were used. Here, 50 mL of the $AgNO_3$ solution was added to a 3-neck flask, and heated, under stirring, until the water boiling temperature ($100°C$). The temperature inside the flask was monitored with a thermocouple and the system was heated by evolving the flask in a heating blank. Then, 1.0 mL of the Na_3Ct solution was added and the system was kept under stirring during 5 minutes. Subsequently, the solution was transferred to a 50 mL tube on an ice-bath. As the system reached the room temperature, the solution was collected and divided into the eppendorfs. The Figure 6 summarizes this procedure.

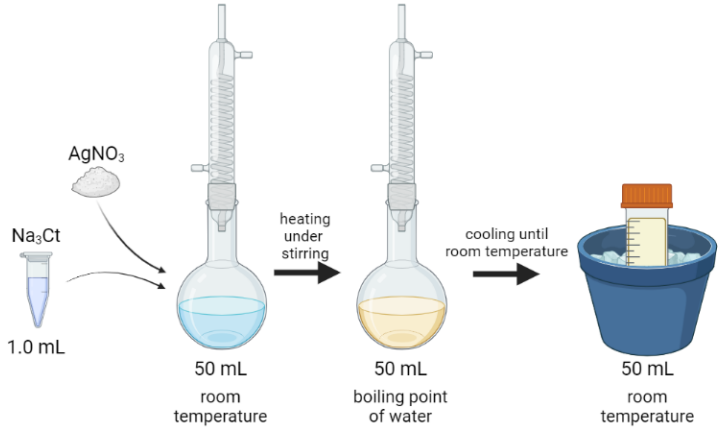

Figure 6 – Methodology for silver nanoparticles synthesis with conventional heating during the chemical step. *Created in BioRender.com*

The irradiation procedure was carried out, in triplicate, in the same instrument and with the same conditions of the previous measurements, including the dose (0 or 50 Gy), the dose rate (2.054 Gy/min).

3.1.3 Synthesis with microfluidic heating

The last approach used for heating the precursor solution was based on the use of a pair of microfluidic reactors. Our system was similar to the setting presented in Figure 7. Two syringe pumps were used to inject the components through the microtubes. The $AgNO_3$ solution was injected with a 1000 μL/min infusion rate, while the Na_3Ct was infused with 60 μL/min, resulting in reaction time of 14 s in the heated and 12 s in the cooled reactors. The concentrations of the infused solutions were the same as in the first two methods.

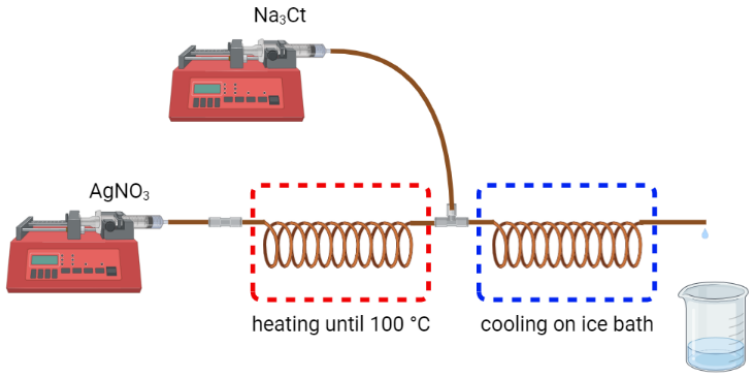

Figure 7 – Methodology for silver nanoparticles synthesis employing a microfluidic reactor during the chemical step. *Created in BioRender.com*

3.1.4 Construction of the microfluidic reactors

The microfluidic reactors were designed to improve the temperature control during the synthesis. The main requirements for this method is that the silver nitrate must be heated alone up to 100 $^{\circ}C$ and the mixture with sodium citrate must be cooled down to room temperature. As a consequence, our system employed two pumps (one for each reactant) and two microchannels (one for each step).

The first reactor was designed as follows: a 1.5 m PEEK®teflon microtube was wrapped around an iron piece with an internal heating element connected to a voltage source, as shown in figure 8. As the system is turned on, electrical current flows through the heating element, leading to heat generation. The microtube is also heated and, due to its large surface-area, the flowing solution inside has its temperature raised. During all the time, the temperature was monitored with a thermocouple. The microreactor was evolved with a thick layer of glass wool and a layer of fabric to avoid heat losses. On both layers, some holes were made to pass the inlet and outlet tubes (the extremities of the microtubes), the sensor of the thermocouple and the cables of the circuit on the iron piece.

The second reactor, used to cool the solution after the mixing the heated Ag precursor with the reducing agent, was much more simple to design. A plastic tube was immersed on a beaker with ice and a thermometer to control the temperature. The acceptable temperature range was defined as 0 - 5 ^{circ}C. Every time the temperature passed over to 5 $^{\circ}C$, more ice was added to the beaker, to keep the system on the acceptable range. The reactors were connected to each other and to the syringe pumps with plastic connectors.

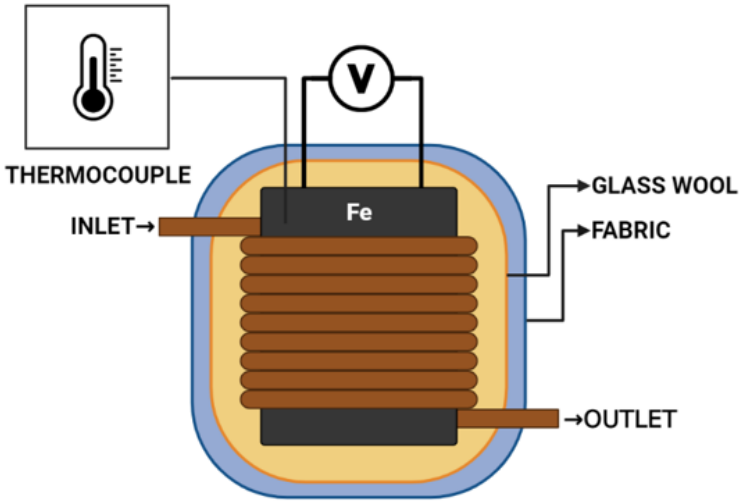

Figure 8 – Scheme of the microreactor used on the microfluidic approaches. *Created in BioRender.com*

3.1.5 Irradiation conditions

As mentioned above, the solutions were irradiated mainly with a Magnum X-ray source, with tube volage 48 kVp, effective energy 10 keV and current of 0.2 mA. However, for some experiments, different irradiation conditions were employed. In this case, as different beam energies were needed, the samples were irradiated with an Isovolt Titan E-160M-2 GE (refereed as 'Titan tube'). The energy and current were controllable.

The beam characterization was made before the irradiation of the samples. The effective energy was calculated for each used voltage, from 60 to 160 kV. The half-value layer (HVL) was obtained with a PTW Electrometer system and high-purity aluminum plates. Then, the total attenuation coefficient (μ) was calculated, in cm^{-1}, by Equation 3.1. Accounting for the aluminum density (2.7 g/cm^3), the mass attenuation coefficient (μ/ρ) was obtained, in cm^2/g, by Equation 3.2. Finally, with the expected values for μ/ρ obtained in the NIST XCOM website (3), the effective energy for each voltage was obtained by interpolation. Table 2 shows all these calculated data and Figure 9 presents the mass attenuation coefficient for aluminum as a function of the beam effective energies

$$\mu = \frac{0.693}{HVL} \tag{3.1}$$

$$\left(\frac{\mu}{\rho}\right)_{Al} = \frac{\mu}{\rho_{Al}} \tag{3.2}$$

Table 2 – Calculations of the effective energy for each voltage in the Titan tube

Voltage	**HVL**	μ **(cm^{-1})**	μ/ρ **(cm^2/g)**	**Effective energy**	**Dose rate**
60 kV	0.19	3.65	1.35	29.04 keV	0.4 Gy/min
80 kV	0.24	2.89	1.07	31.05 keV	0.7 Gy/min
100 kV	0.30	2.31	0.86	34.87 keV	1.0 Gy/min
120 kV	0.37	1.87	0.69	37.76 keV	1.3 Gy/min
160 kV	0.50	1.39	0.51	42.75 keV	2.1 Gy/min

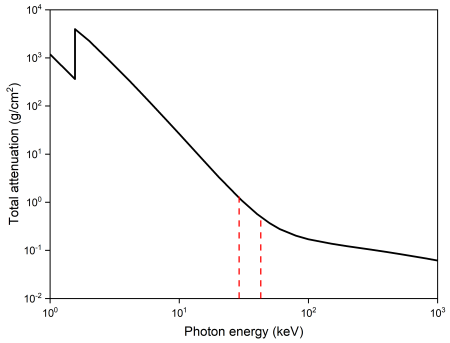

Figure 9 – Mass attenuation coefficients for aluminum, emphasizing the work region. Data obtained from (3)

With this beam, all irradiations were carried out with a 30 cm source-to-sample (SSD) distance. The samples were placed in a watch glass under the radiation source, alligned with the center of the tube irradiation field. The nominal dose rate for each voltage, which was measured for SSD = 100 cm, was corrected by the inverse square law. The real dose rate, considering a tube current of 10 mA is presented in the last column of the table 2.

3.2 Gold nanoparticles synthesis

3.2.1 Checking the viability of the synthesis

The gold nanoparticles synthesis followed the route presented by Pushpavanam et al. (50). The main advantage of this route is the unnecessity of heating, which enables us to use a little quantity of precursor. Consequently, the cost of this approach is diminished as the required quantity of gold is not high.

This synthesis works with the chloroauric acid ($HAuCl_4$) as the gold precursor, the ascorbic acid ($C_6H_8O_6$, abbreviated to AA) as the reducing agent and the cetyltrimethylammonium bromide (CTAB) as the template. Here, the CTAB molecules form a micelle, with the hydrophilic part outside and the hydrophobic part inside it. 37.5 μL of $HAuCl_4$ 10 mM and 750 μL of CTAB 50 mM were mixed at room temperature. At this point, the

solution achieved a yellow color. A 50 Gy dose was given at this stage. The irradiation was performed with the Magnum X-ray source and 2.054 Gy/min dose rate.

After that, the unirradiated samples were mixed with 750 μL of AA 10 mM. The solution became immediately colorless. This sample was then also irradiated with 50 Gy with the same x-ray tube. The final solution was deep purple, indicating formation of large nanoparticles.

The characterization of the nanoparticles was performed by absorption spectroscopy, to observe the LSPR band. Also, the size of the nanoparticles was measured by dynamic light scattering.

3.2.2 Optimizing the parameters for the gold nanoparticles synthesis

The reaction and irradiation parameters were varied to verify their influence on the gold nanoparticles formation. For each case, only irradiations with 50 Gy were taken. Table 3 shows all the parameters studied. The variations of the dose rate were obtained on the 48 kVp Magnum X-ray source, by changing the SSD, whereas the beam voltage optimization experiments were made with the Titan X-ray tube.

As in the previous experiments, UV-vis spectroscopy and dynamic light scattering were employed to analyze the samples.

Table 3 – Parameters for gold nanoparticles synthesis optimization

Parameter	**Interval**
Concentration of $HAuCl_4$	1 to 10 mM
Concentration of Ascorbic acid	2 to 10 mM
Dose rate	0.274 to 3.254 Gy/min
Beam voltage	60 to 160 kV

3.3 Characterization

3.3.1 Uv-vis spectroscopy (ABS)

UV-vis spectroscopy, was performed in an Ultrospec 2100 pro UV-visible spectrometer. The spectra were collected in the 300 - 900 nm interval, thus including all the visible, near ultraviolet and near infrared range. All the samples, without any dilution or purification, were placed on quartz cuvettes with 10 mm length. Ultrapure water was used as reference.

3.3.2 Fluorescence spectroscopy (FLS)

The fluorescence spectra were recorded on a Hitachi F7000 fluorescence spectrometer. The excitation spectrum was collected with emission fixed at 380 nm (81). Since 240 nm was found to be the best excitation wavelength, the emission spectroscopy measurements were carried out in the 265-445 nm emission interval, to avoid the peaks related to the water Raman scattering and the harmonic from the incident light, respectively. For all samples, a quartz cuvette with 2 mm optical length was employed.

3.3.3 Dynamic light scattering (DLS)

The DLS measurements, used to obtain the hydrodynamic size of the nanoparticles, were collected on a Zetasizer Nano of Malvern Instruments. All the samples were diluted 50x before the measurement (24 μL of the original solution in 1.2 mL of water). The solutions were added in acrylic cuvettes with 10 mm optical length. For the silver nanoparticles, the refractive index was n = 0.135 and the absorption was k = 3.99. For gold nanoparticles, the respective values were n = 0.20 and k = 3.32.

3.3.4 Transmission electron microscopy (TEM)

Microscopic images were recorded with a Hitachi HT7700 transmission electron microscope Hitachi HT7700. The solutions were diluted 20x (750 uL of the original solution in 1.5 mL of water), dropped on the surface of copper TEM grids and dried overnight.

The size distributions from the TEM images were obtained as follows. First of all, a treatment on the images was carried out, to enhance the contrast between the particles and the surrounding. To this end, the images were treated with a Bandpass filter, followed by a Minimum filter of 1.0 radius. As the nanoparticles were highlighted in the image, the threshold was adjusted and then the nanoparticles were found by the Particle Analyzer function. The minimal acceptable circularity was set to 0.70, as the spherical nanoparticles are desirable but not completely achieved.

4

Dosimetry based on the synthesis of silver nanoparticles

In this chapter, the main results about silver nanoparticles synthesis will be presented and the relevant discussions developed. The results will be divided according to the development of our synthetic protocol. The silver nanoparticles were synthesized by a reduction method. The silver nitrate ($AgNO_3$) was used as the precursor agent, and the sodium citrate (Na_3Ct) was used as reducing agent. The components were mixed at a controlled temperature and irradiated with X-ray beams.

4.1 Development of synthesis protocol

In this section, the synthesis route was developed from the assumption that the reduction would be accelerated by the x-ray beam. The importance of a heating process before the irradiation was tested, aiming the formation of the particles. After that, the optimized protocols were employed for dosimetric applications with doses from 0.25 to 50 Gy.

4.1.1 Effect of heating the precursor solution

On the subsequent results, the concentration of the precursor and the reducing agents were varied to produce three samples, according to the Table 4.

Table 4 – Precursor solutions for silver nanoparticles synthesis

Solution	$[AgNO_3]$	$[Na_3Ct]$	**Line color**
1	1 mmol.L^{-1}	1%	red
2	1 mmol.L^{-1}	5%	blue
3	2 mmol.L^{-1}	5%	green

Figure 10 shows the UV-vis spectra for the chemical synthesis, without heating and irradiation. Figure 10(d) shows the average spectra for each tested sample. Any well defined absorption band was detected in these spectra, indicating the absence of nanoparticles when the synthesis were carried under these conditions.

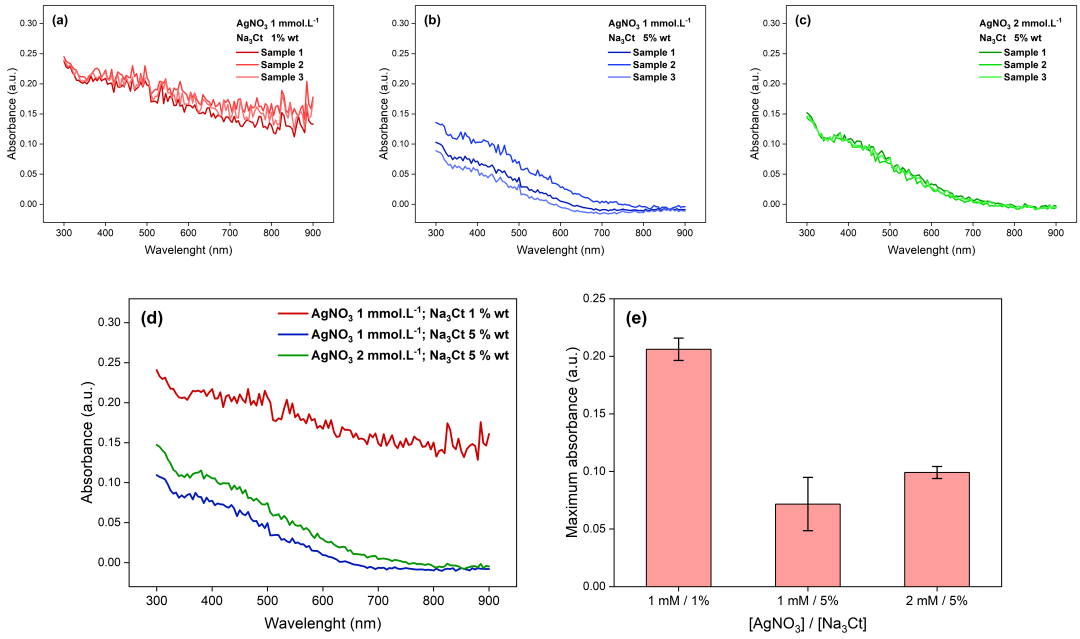

Figure 10 – UV-vis spectra for samples without heating or irradiation processes with $AgNO_3$ and Na_3Ct concentrations of (a) 1 mmol.L^{-1} / 1% wt; (b) 1 mmol.L^{-1} / 5% wt and (c) 2 mmmol.L^{-1} / 5% wt. (d) Average spectra and (e) maximum absorbance for each sample

Figure 11 show the spectra obtained with the same samples, after an irradiation with 50 Gy. When the samples are irradiated, an absorption peak appears, indicating the formation of nanoparticles. However, the absorbance intensity is relatively high in all spectra and there is a plateau between 800 and 900 nm, for example, presenting up to 16% noise on the curves). Furthermore, the plateau after the plasmon band, which is expected to decrease to absorbance values around 0 for sample with uniform and well dispersed nanoparticles, increases in intensity upon increasing the concentration of both reactants (either Ag or Na3Ct). Therefore, these results suggest that the effect of the radiation on the synthesis, when used isolated, is a disorderly formation of the nanoparticles and a possible aggregation process.

The polydispersity can be qualitatively inferred by the width of LSPR bands. The higher the polydispersity, the larger the absorption band. The bands obtained with these methods were fitted by a Gaussian distribution, not considering the portion before the band (300 to 350 nm), in order to obtain the full width at half maximum (FWHM). The FWHM values obtained for the bands in Figure 11(d) were 195, 302 and 197 nm, for the red, blue and green lines, respectively. The increase in sodium citrate led to a

more polydispersed sample, which can be explained by a disordely reduction of silver and capping of the particles. The addition of more silver nitrate produced a less polydispersed solution. This behavior can be attributed to the increase in the nucleation rate, due to the higher availability of silver in dispersion. These values will be compared with the results obtained with a combination of heating and irradiation process, in order to infer about the role of each method on the size distribution.

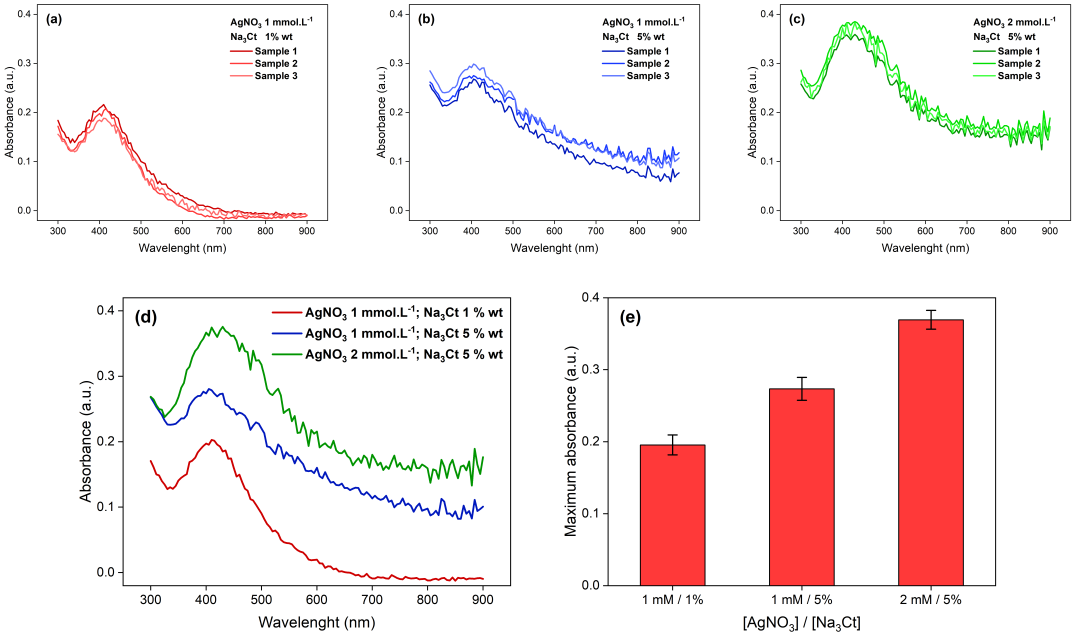

Figure 11 – UV-vis spectra for samples just irradiated with 50 Gy, with $AgNO_3$ and Na_3Ct concentrations of (a) 1 mmol.L^{-1} / 1% wt; (b) 1 mmol.L^{-1} / 5% wt and (c) 2 mmmol.L^{-1} / 5% wt. (d) Average spectra and (e) maximum absorbance for each sample

4.1.2 Synthesis of AgNP with conventional heating

A heating step was added to the synthesis before the irradiation. The samples were heated in a 3-neck flask until the water boiling point and then cooled to room temperature. Irradiated and non-irradiated samples were compared.

Figure 12 shows the spectra obtained for the samples produced only by heating as well as the average spectra and the maximum absorbance for each concentration of these samples. There are distinctive bands for all concentrations, indicating that the heating is sufficient to catalyze the nucleation process. The fact that the second sample, which has the highest $[Na_3Ct]$:$[AgNO_3]$ ratio, generated the lower and wider absorbance band suggests that the capping effect of citrate limits the growing process. This synthesis is generally carried out with a longer time of heating. In this case, there is not a significant difference between the absorbance of each sample.

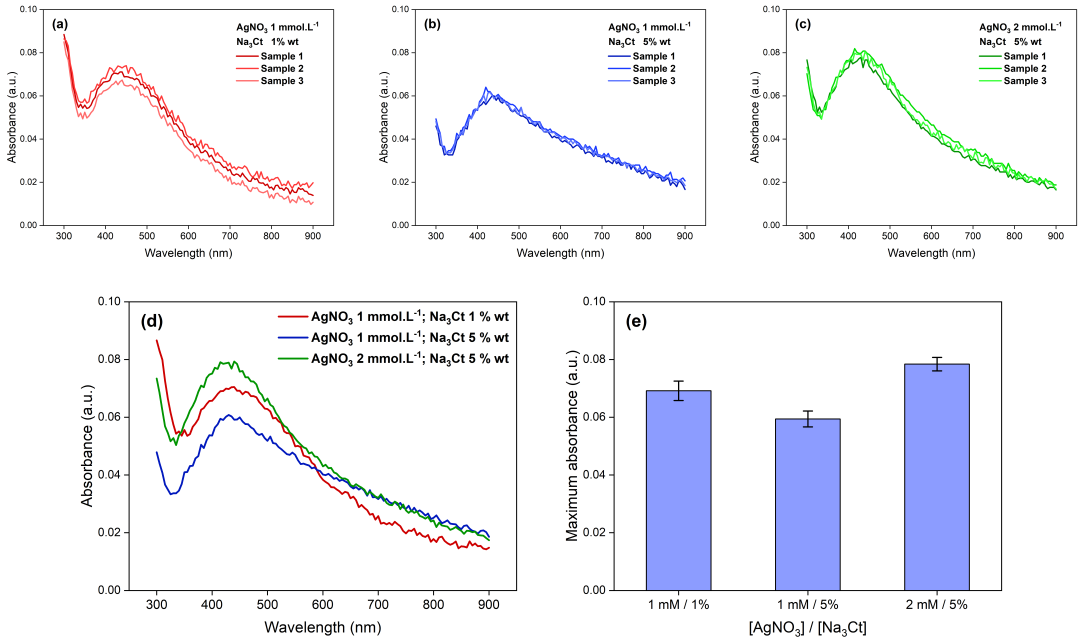

Figure 12 – UV-vis spectra for samples heated but non-irradiated, with $AgNO_3$ and Na_3Ct concentrations of (a) 1 mmol.L^{-1} / 1% wt; (b) 1 mmol.L^{-1} / 5% wt and (c) 2 mmmol.L^{-1} / 5% wt. (d) Average spectra and (e) maximum absorbance for each sample

The size distributions were examined in terms of the FWHM. For this case, the width obtained for red, blue and green lines were 302, 292 and 289 nm. These values are higher than the obtained for the particles synthesized only with radiation. The heating, at least with the short time employed, is not so effective in generating a less polydisperse distribution of nanoparticles. This result, and the lower absorbance intensity compared to the bands in Figure 11, lead to the conclusion that, in this approach, the nucleation is highly catalyzed but a lower amount of particles is produced, which can be an indication of the viability of the heating as an intermediate process.

Figure 13 shows the absorbance spectrum for each sample that was heated and irradiated. Well defined bands are detected for all samples, especially for those ones with lower $[Na_3Ct]$:$[AgNO_3]$ ratio, supporting the conclusion that the capping agent is limiting the growth. For all samples, the absorbance increased compared to the results in figure 12. This indicates that the irradiation process resulted in nanoparticles growth.

Compared to the results presented in Figure 11, the absorbance is lower when the sample is irradiated after heating. This result suggests that, without heating, a disordered formation of nanoparticles take place, consuming the silver precursor and limiting the amount of particles that can be produced, probably because few nuclei are formed in non-heated samples. It is worth noting that the bands in Figure 13 are better defined than the bands in Figure 11, and their backgrounds are closer to zero. These results suggest that the heat/irradiation combination leads to narrower size distributions than the obtained

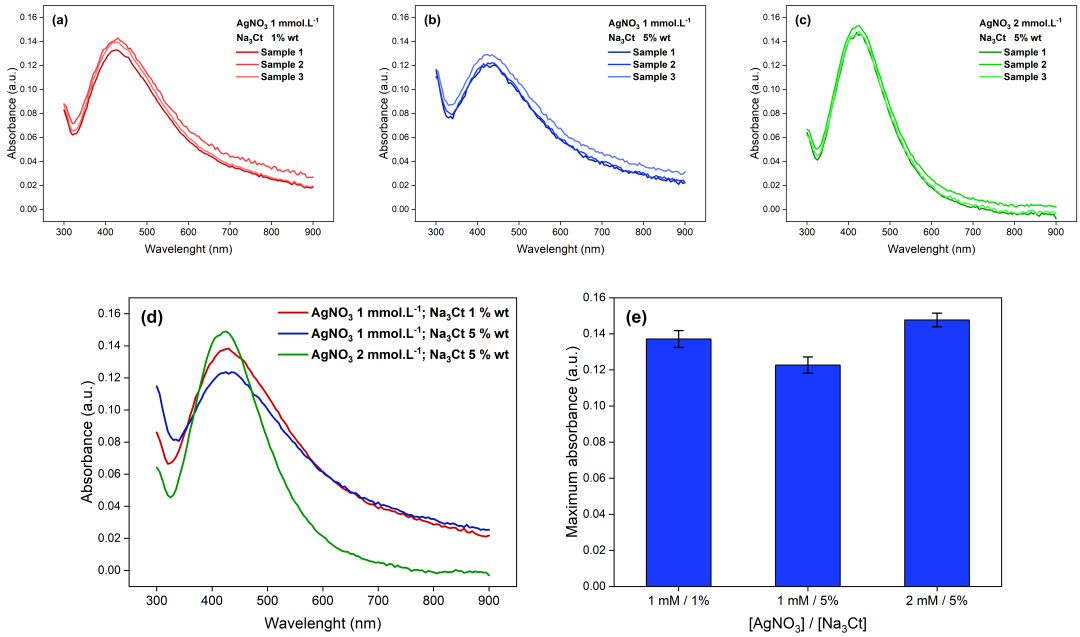

Figure 13 – UV-vis spectra for samples heated and irradiated, with $AgNO_3$ and Na_3Ct concentrations of (a) 1 mmol.L^{-1} / 1% wt; (b) 1 mmol.L^{-1} / 5% wt and (c) 2 mmmol.L^{-1} / 5% wt. (d) Average spectra and (e) maximum absorbance for each sample

when only the irradiation takes place. This is supported by the smaller FWHM obtained for these samples (225, 260 and 167 nm for red, blue and green lines). Consequently, the combination of heating with irradiation makes the samples more suitable for dosimetric purposes.

4.1.3 Synthesis of AgNP with microfluidic heating

The conventional heating process was substituted by the microfluidic approach in order to achieve a better control of the solution heating and cooling, avoiding temperature gradients, that are common in the flask. The same procedures were developed, allowing a direct comparison of the results. Figure 14 shows the absorbance spectra obtained with the samples heated in the microfluidic reactor until the boiling point of water and then immediately cooled down. The average spectra and the maximum absorbance are also shown in this figure.

The absorbance presented by these samples is incredibly low at the plasmonic region, indicating that any nanoparticle is formed without irradiation. This result suggests that the nucleation is taking place during the quick heating step while the growing process is avoided by the fast cooling allowed by the microfluidic reactor. Therefore, we expect that the growth will occur exclusively after irradiation of the seeds formed in the microreactor.

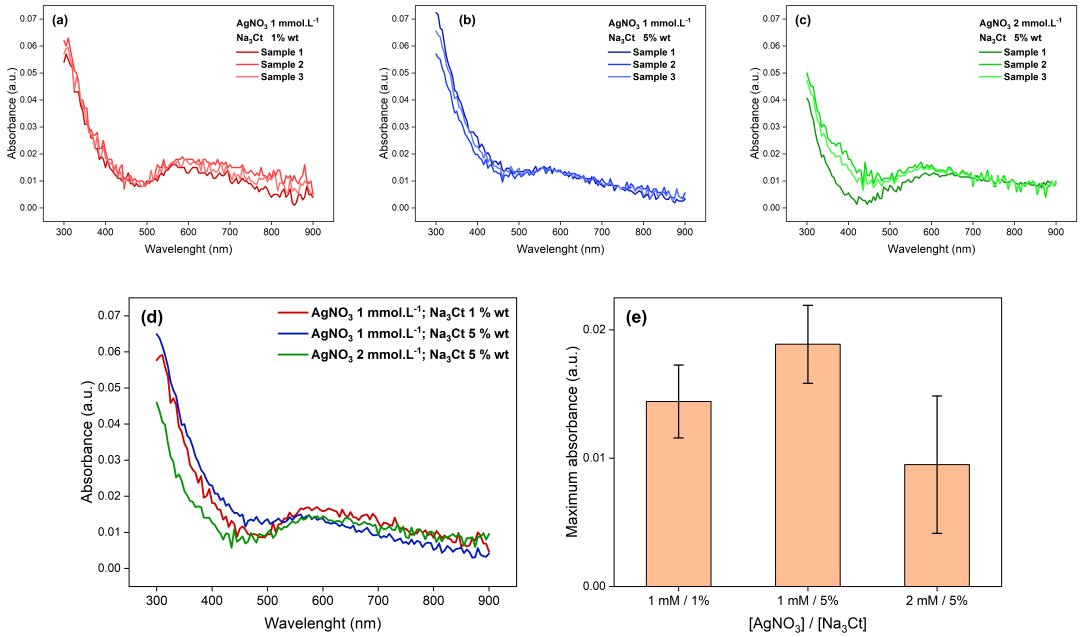

Figure 14 – UV-vis spectra for non-irradiated samples heated in the microfluidic system, with $AgNO_3$ and Na_3Ct concentrations of (a) 1 mmol.L^{-1} / 1% wt; (b) 1 mmol.L^{-1} / 5% wt and (c) 2 mmmol.L^{-1} / 5% wt, (d) Average spectra and (e) maximum absorbance for each sample

It is noteworthy that all the samples produced with the microfluidic approach presented an absorption band centered around to 580 nm. Although theiy present low intensity, these bands could not be ignored. According to the literature, an apparent shifts in LSPR bands can, in factm be assigned to the light absorption from to oligomeric particles, due to interaction between nucleophilic reagents and surface atoms of clusters (82). This reinforces the proposed mechanism of nanoparticles formation, with these detected clusters corresponding to an intermediate state before silver nanoparticles formation (26). Moreover, this absorption peak has been addressed to clusters containing few Ag atoms (83). Therefore, this seems to confirm that only nucleation takes place during the heating in the microreactor.

To further verify this hypothesis, the same procedure with the microreactor early described was repeated, but, in this case, with an irradiation (50 Gy) process after the chemical synthesis. The samples were then irradiated with the 48 kV beam. The individual spectra obtained are presented in Figure 15, with the average spectra and the maximum absorbance for each concentration.

As observed in the figures, the samples produced in the microreactor followed by exposition to x-rays present a characteristic LSPR band. It is clear that the previous heating in the microreactor is able to induce the production of a high amount of nanoparticles, which, in turn, lead to an intense SPR peak. It is noticeable that the peaks in Figure 15, related to samples produced in the microreactor, are much narrower than the ones in the

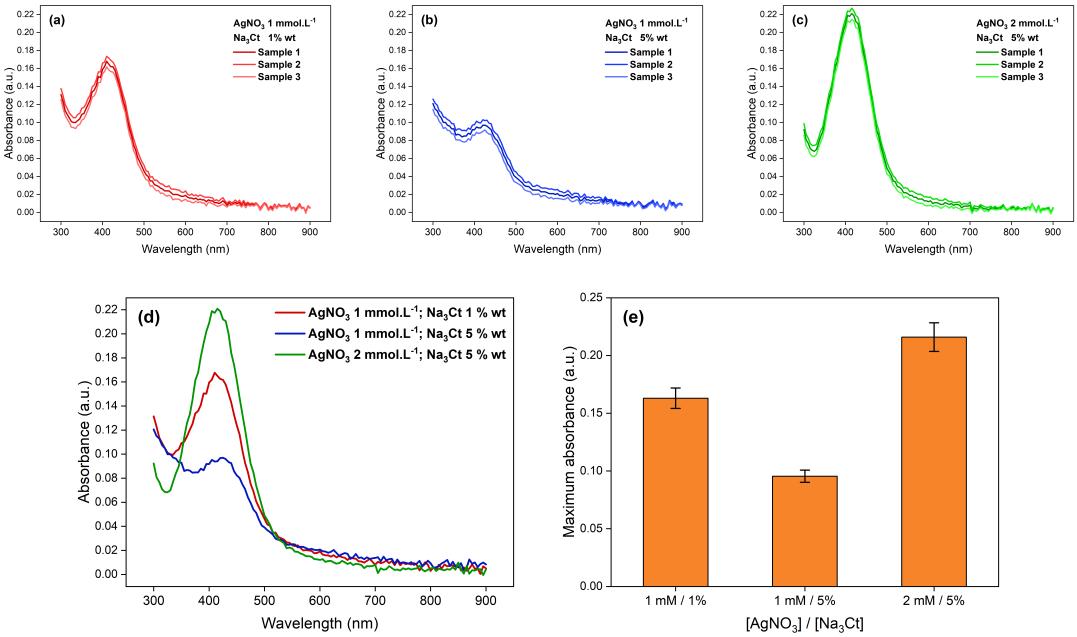

Figure 15 – UV-vis spectra for irradiated samples heated in the microfluidic system, with $AgNO_3$ and Na_3Ct concentrations of (a) 1 mmol.L^{-1} / 1% wt; (b) 1 mmol.L^{-1} / 5% wt and (c) 2 mmmol.L^{-1} / 5% wt. (d) Average spectra and (e) maximum absorbance for each sample

Figure 13, related to samples produced in a conventional flask. In fact, the FWHM of these samples are nrrower than the obtained for samples produced with the conventional method (137, 154 and 116 nm, for red, blue and green lines, respectively). This suggests a greater control of the particle size distribution prompted by the microfluidic method, once polydisperse nanoparticles leads to broader LSPR bands.

4.1.4 Comparison between the methods

After all, the methods for nanoparticle synthesis were compared with each other by the capability of the radiation to enhance the production of the particles and, therefore, to increase the absorbance band intensity. Figure 16 shows the comparison of the intensity of each absorbance peak. When the LSPR band was not clearly observed (for example, in the Figures 10 and 14), the maximum value on the LSPR peak interval (400 - 440 nm) was taken as representative of that absorbance.

The unheated samples presented higher intensities than the heated ones. However, as shown in the earlier sections, these samples presented a high background signal (Figures 10 e 11), which is undesired for dosimetric purposes. Samples produced with both conventional and microfluidic routes show a well-defined LSPR band, although their maximum intensities were reduced compared to the unheated samples. Also, the intensity of the absorbance peak, generally, increases significantly when the samples were irradiated.

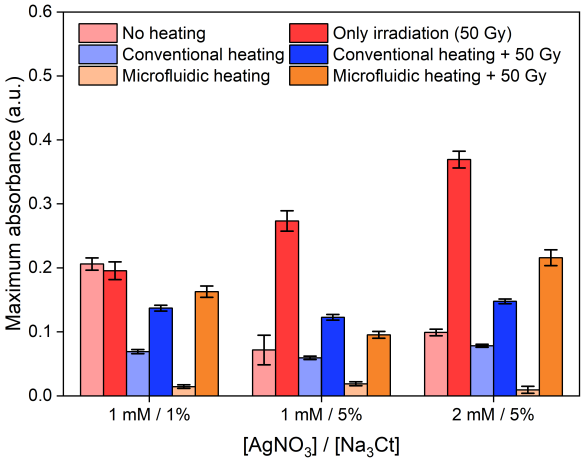

Figure 16 – Maximum absorbance observed for the synthesis with no heating; conventional heating; and microfluidic heating.

Figure 17 depicts the enhancement of the absorbance after irradiation for each sample and for each method. Basically, each bar in the graph correspond to the absorbance value in the LSPR spectral region of irradiated samples divided by the absorbance of the respectives non-irradiated samples.

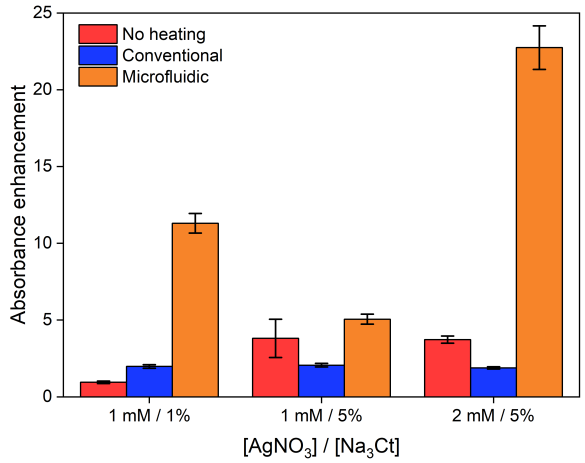

Figure 17 – Absorbance enhancement after irradiation (50 Gy) for the nanoparticles produced without heating, with conventional heating and with microreactor heating for each [Ag]/[Na_3Ct] proportion

Therefore, Figure 17 reveals that the microfluidic approach provides the largest absorbance enhancement, for all tested Ag and Na_3Ct concentrations. For dosimetric purposes, this could result expected to result in higher dosimetric sensitivities for radiation detection. The qualitative analysis indicates the same result, once the LSPR band is not observed in non-irradiated samples but is very intense and well-defined for the irradiated ones. The conventional approach has a qualitatively good behavior as well, but the gain is affected by the presence of a relatively intense LSPR band even without irradiation. This

band probably appears due a formation of nanoparticles caused during the slower cooling process in the flask.

All the results in this section show the importance of a previous heating process for the synthesis of silver nanoparticles. This step is capable to produce seeds which will be the basis for the particles growth. Moreover, the control of the heating and cooling processes is also very important. As the microfluidic reactor allows a faster cooling process (and, consequently, a shorter time at high temperatures), a better control of the nanoparticles size distribution is achieved, as indicated by the narrower LSPR bands. Next experiments will employ only samples heated before the irradiation

4.2 Ionizing radiation dosimetry with silver nanoparticles

The synthesis procedures studied in the previous section evidenced the importance of the microfluidic heating and cooling processes before the irradiation, opening new avenues for dosimetry. Therefore, we produced nanoparticles with doses varying from 0.5 to 50 Gy to study how the dose affects the nanoparticle synthesis.

The dispersions produced in those radiochemical routes (both conventional and microfluidic) present a characteristic feature in macroscopic scale. As the dose absorbed increases, more nanoparticles are synthesized and, due to the LSPR phenomenon, some of the wavelengths are absorbed. As a consequence, the dispersion becomes yellow, and this color is more intense as much as the dose is higher. Figure 18 presents a group of samples, irradiated with doses varying from 0 to 50 Gy, as an example.

Figure 18 – AgNP dispersions irradiated with doses from 0 to 50 Gy

For dosimetry purposes, we studied the angular coefficient of the dose response curve given in terms of absorbance, to verify which method is more efficient to constitute a radiation dosimeter.

For the conventional method, Figure 19(a) shows the curves for each dose from 0 to 50 Gy, obtained as the average of three irradiated samples with 2 mmol.L^{-1} $AgNO_3$ and 5% wt Na_3Ct. Figure 19(b) depicts the maximum absorbance and the respective standard deviation.

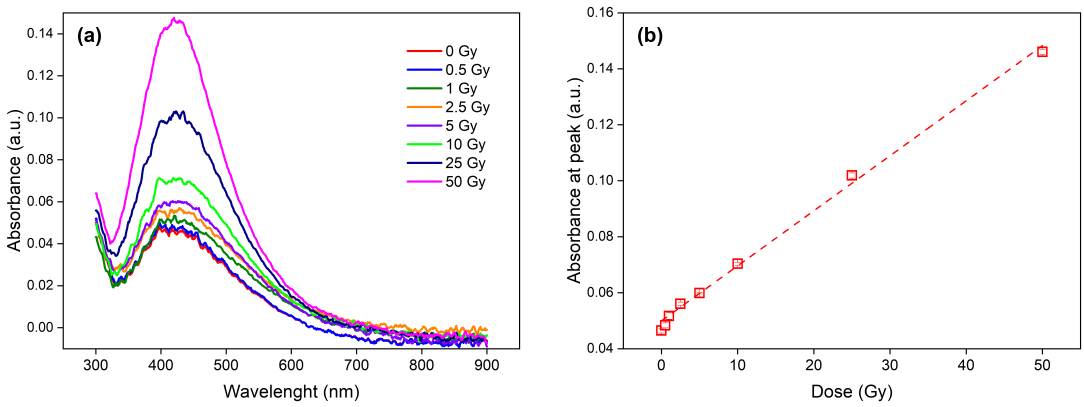

Figure 19 – (a) Average absorbance spectra for nanoparticles produced with the conventional method with irradiated with doses from 0 to 50 Gy; (b) Maximum absorbance at the plasmonic range as a function of dose, for sample with 2 mmol.L^{-1} $AgNO_3$ and 5% wt Na_3Ct

Both figures reveal the same behavior previously noticed: a significant signal even without irradiation, attributed to the complete formation of nanoparticles during the heating process. Because the solution was not quickly cooled, the thermal energy was enough to reduce a remarkable quantity of silver ions, thereby promoting both nucleation and growth processes.

The angular coefficient in the curve in Figure 19(b) is $(2.0 \pm 0.5) \times 10^{-3}$ a.u./Gy. This value could be taken as the sensitivity of the sensor, as it represents the change in absorbance due to the formation of more nanoparticles, i.e., the change in absorbance due to the absorbed dose. This sensitivity is close to the values obtained in the literature. Notably, the work published by Funaro et al. (24), which was the starting point of this work, produced silver nanoparticles by gamma-ray irradiation with sensitivity of 4.2×10^{-3} a.u./Gy from 0 to 120 Gy, with their approach. The observed differences in sensitivity could be attributed to different irradiation conditions and radiation quality (as we are using beams with lower energies, one could expect a different impact on nucleation and growt, but still with a linear behavior).

The results from figure 19 were analyzed in terms of the reliability of the signal and by determining the minimal detectable change (MDC). The reliability is a measurement of the results consistency (84), and can be obtained by the Standard Error Measurement (SEM), which quantifies the precision of individual measurements (85, 86). Then, the MDC can be obtained from SEM by equation 4.1 (86). In that equation, SEM is obtained by the Standard Error between all the measurements in the ground state (in this work, the

measurements at 0 Gy) and the value 1.96 is due to the z-score for 90% confidence level, which is our aim. The MDC, thus, represents the lowest measurable value (in our work, the absorbance intensity) that can not be accounted as a noise related to the standard sample (unirradiated).

$$MDC = SEM \times 1.96 \times \sqrt{2} \tag{4.1}$$

With the values obtained in this case, the MDC resulted in 0.005 a.u., which means that the significant measurements are those which are at least 0.005 absorbance units greater than the value for the 0 Gy one, which is 0.046. Thus, the lower significant value is 0.051 a.u.By interpolation with the results for 0.5 Gy (0.048) and 1 Gy (0.052) the minimal detectable dose (MDD) for this dosimeter was found to be 0.89 Gy.

After that, we did the same experiment with samples produced by the microfluidic approach. Figure 20(a) shows the curves for each dose from 0 to 50 Gy. As in the conventional method, the spectra are the average of three samples. Figure 20(b) depicts the maximum absorbance obtained in the LSPR region for each dose.

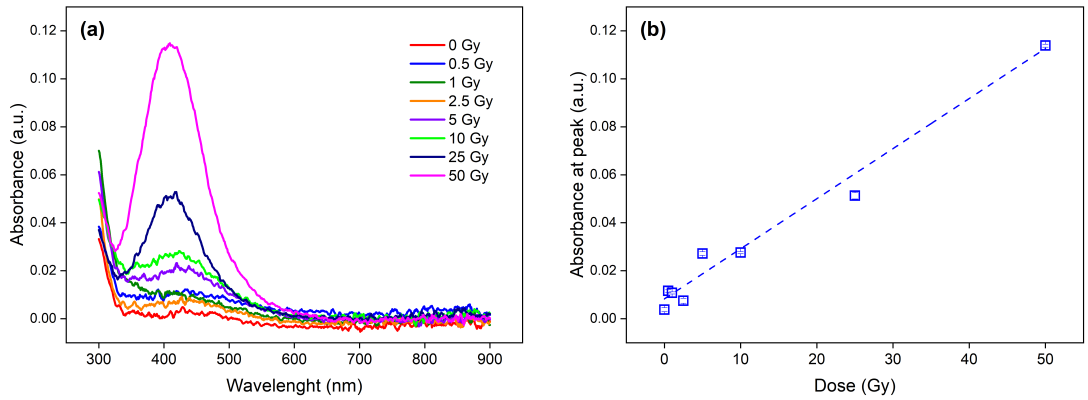

Figure 20 – (a) Average absorbance spectra for samples produced in the microreactor with irradiation from 0 to 50 Gy; (b) Maximum absorbance obtained at the plasmonic range as a function of dose, for sample with 2 mmol.L^{-1} $AgNO_3$ and 5% wt Na_3Ct

The first important aspect of this result is the absence of a significant signal in the LSPR region for the non-irradiated samples. As expected, the better control of the heating and cooling processes avoid nanoparticles formation before irradiation. Figure 21 brings our proposed mechanism on how the processes might be happening in each case. As discussed earlier, a significant number of particles are formed with the conventional route because nucleation and growth take place during the chemical step. The microfluidic protocol, however, prevents the early formation of nanoparticles, allowing that only nucleation happens in the chemical step and avoiding that particle growth occurs before the irradiation.

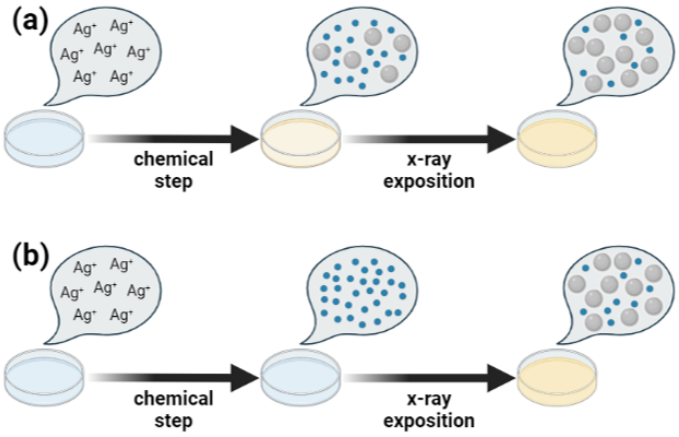

Figure 21 – Our hypothesis on how the nucleation and growth of silver nanoparticles occurs in (a) conventional and (b) microfluidic approaches. The blue balls represent the silver seeds and the grey ones the silver nanoparticles

For this methodology, the sensitivity was obtained by the same analysis. In this case, the slope was $(2.1 \pm 0.1) \times 10^{-3}$ a.u./Gy. The value is close to the one found for the conventional route, which means, at first glance, that, although the silver atoms are not consumed for particle growth before the irradiation, this actually did not impact the growth rate after irradiation. Figure 22 presents both curves obtained for each method and a third one representing the data and the fitting for the conventional method vertically shifted to remove the background relative to the 0 Gy signal and give a better representation of the sensitivities (i.e. the angular coefficients).

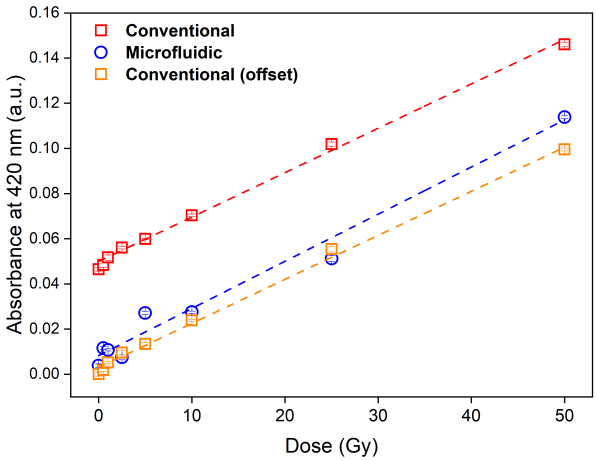

Figure 22 – Maximum absorbance for each dose from 0 to 50 Gy for the methods developed to synthesize nanoparticles: (red) conventional route, (blue) microfluidic route and (orange) conventional route (dislocated). The samples contained 2 mmol.L^{-1} $AgNO_3$ and 5% wt Na_3Ct

The MDC was calculated here by the same method described before, applying the standard deviation in equation 4.1. For the microfluidic route, the MDC was 0.002 a.u. Once 0 Gy signal is 0.004, the minimal significant absorbance is equal 0.006 a.u., which

means that the MDD in this method is equal to 0.63 Gy. In this sense, the microfluidic approach has proven to be more efficient than the conventional one on detection of lower doses.

4.2.1 Radiation dosimetry with silver nanoparticles in the 0 - 2.5 Gy dose region

As both methods were found to be applicable for dosimetry, a new challenge was detected: to obtain reliable measurements in the low dose region (from 0 to 2.5 Gy). A good performance within this interval is highly desirable because it is close to the radiation therapy range, thereby allowing applications in medical procedures. In fact, as observed in Figure 20, it seems that a different sensitivity would obtained in the 0 - 2.5 Gy range. Therefore, samples were irradiated with the same beam but with doses from 0 to 2.5 Gy. The same conditions and concentrations were used and the same analysis were carried.

Figure 23 show the absorbance spectra for the two methods applied to this lower dose interval. The same behavior previously described happens here. The spectra for the conventional method (23(a)) present a high background. Due to the noise in the curve, all the peaks presented almost the same intensity, revealing that the dosimeters are not sensitized by these lower radiation doses. However, a clear increase in absorbance is noticed for the samples produced by the microfluidic approach (23(b)), indicating that the microreactor improves the dosimetric sensitivity in the lower dose region.

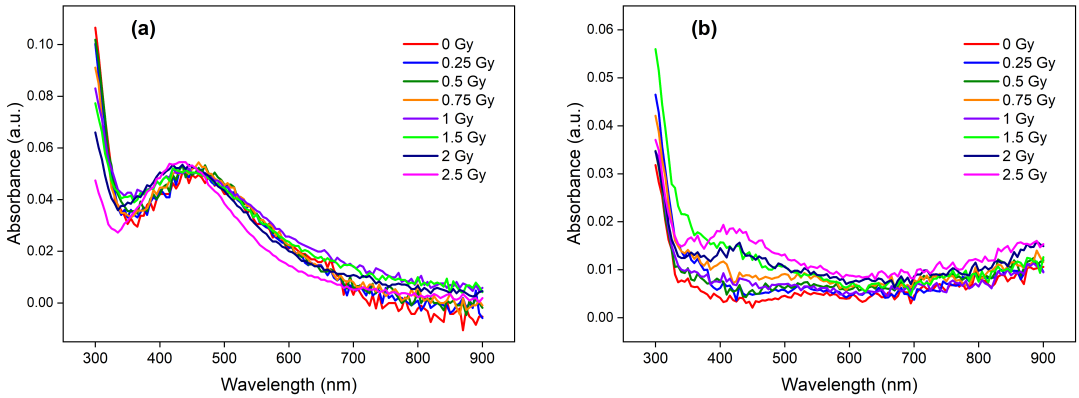

Figure 23 – (a) Average absorbance spectra of nanoparticles produced with the conventional method and irradiated with doses from 0 to 2.5 Gy; (b) Average absorbance spectra of nanoparticles produced by the microfluidic method and irradiated with doses from 0 to 2.5 Gy. The samples contained 2 mmol.L^{-1} $AgNO_3$ and 5% wt Na_3Ct

The maximum of each curve was taken considering the plasmonic range (400 to 440 nm). The intensity, for each dose is shown in Figure 24. The red and blue curves show

the results for the conventional and microfluidic approaches, respectively, and the orange curve represents the data from the red curve shifted in order to eliminate the background gap and allow a direct comparison with the blue one.

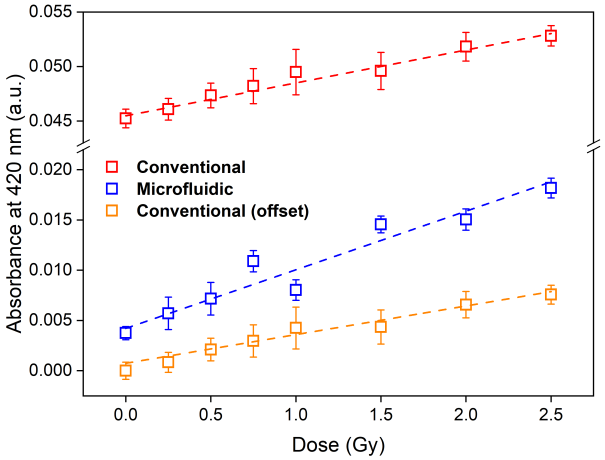

Figure 24 – Maximum absorbance for each dose from 0 to 2.5 Gy for the methods developed to synthesize nanoparticles: (red) conventional route, (blue) microfluidic route and (orange) conventional route (dislocated). The samples contained 2 mmol.L^{-1} $AgNO_3$ and 5% wt Na_3Ct

The slope for the blue line is clearly greater than the ones for the other lines, indicating that the sensitivity of this method (the microfluidic route) is greater than for the conventional one. In fact, the slope values are $(3.0 \pm 0.1) \times 10^{-3}$ a.u./Gy and $(5.8 \pm 0.6) \times 10^{-3}$ a.u./Gy for the conventional and microfluidic approaches, respectively. It is important to note that the sensitivities are greater for both methods in this interval (0 - 2.5 Gy), compared to the first one (0 - 50 Gy). Also, the sensitivity for dosimeters produced in the microreactor is twice the conventional one, clearly indicating the impact of the heating method. The effect is more pronounced for lower doses probably due to the higher availability of silver ions in solution, in samples irradiated with low doses. Upon increasing the dose, more nanoparticles are formed, consuming more silver ions, thereby decreasing the particle growth rate and, consequently reducing the dosimetric sensitivity in the higher dose range. The MDD for the conventional and microfluidic approaches, calculates from the Equation 4.1, were 0.66 and 0.20 Gy, respectively, thus demonstrating the higher efficacy of the microfluidic method.

The absorption around 580 nm was predominant in the UV-vis spectra for samples irradiated with doses below 1 Gy, suggesting that nanoclusters have a high contribution to the absorbance in this dose range, as depicted in Figure 25. For doses above 1 Gy, absorption due to the LSPR starts to take place and becomes predominant at for doses $\geq$ 1.5 Gy, indicating that silver nanoparticles are now present. This result reveals that, besides predominating during the microreaction process, nucleation still predominates in samples irradiated with doses up to 1 Gy. After that, growth prevails. Moreover, this result

clearly evidences the gradual growth of the nanoclusters into plasmonic nanoparticles.

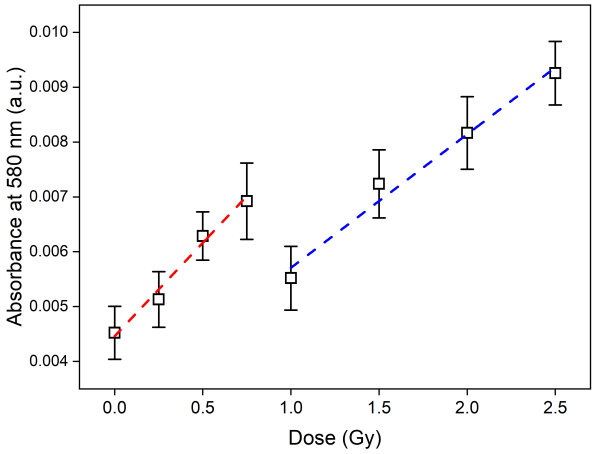

Figure 25 – Absorbance in 580 nm for each dose from 0 to 2.5 Gy for the methods developed to synthesize nanoparticles: (red) 0 to 0.75 interval and (blue) 1 to 2.5 interval. The samples contained 2 mmol.L^{-1} $AgNO_3$ and 5% wt Na_3Ct

For the 0 - 0.75 Gy interval, the calculated sensitivity is $(3.4 \pm 0.3) \times 10^{-3}$ a.u./Gy, with 98% confidence. The minimal detectable dose is 0.40 Gy. Therefore, both for plasmonic and the nanocluster wavelengths, the MDD values are lower than the obtained for the 0 - 50 Gy, thus presenting the efficiency of this dose interval.

4.2.2 Fluorescence dosimetry with nanoclusters

To further verify the presence of silver nanoclusters in the samples irradiated with the lower doses, fluorescence spectroscopy was performed. According to the literature, fluorescence emission from silver nanoparticles occurs in particles containing few atoms, as a result of quantized energy levels. For large nanoparticles, the energy levels are almost continuous, and the larger silver nanoparticles becomes less or even non-fluorescent (87, 88). The small nanoparticles are usually called "nanoclusters", referring to nanoparticles smaller thn 2 nm. Therefore, fluorescence emission from samples exposed to the lower doses could reveal the presence of nanoclusters.

Figure 26(a) shows the fluorescence spectroscopy results from samples synthesized by the microfluidic approach, with doses ranging from 0 to 2.5 Gy. Excitation and emission parameters were obtained from literature (89). Samples were excited with a 240 nm light, and the spectra were collected between 340 and 440 nm. As can be seen, the fluorescence intensity increases for doses up to 0.75 Gy and then diminishes until the end of interval. The Figure 26(b) shows the fluorescence intensity as a function of dose.

As previously discussed before, by employing the microfluidic route, the well-controlled heating and cooling processes allows that only nucleation takes place before

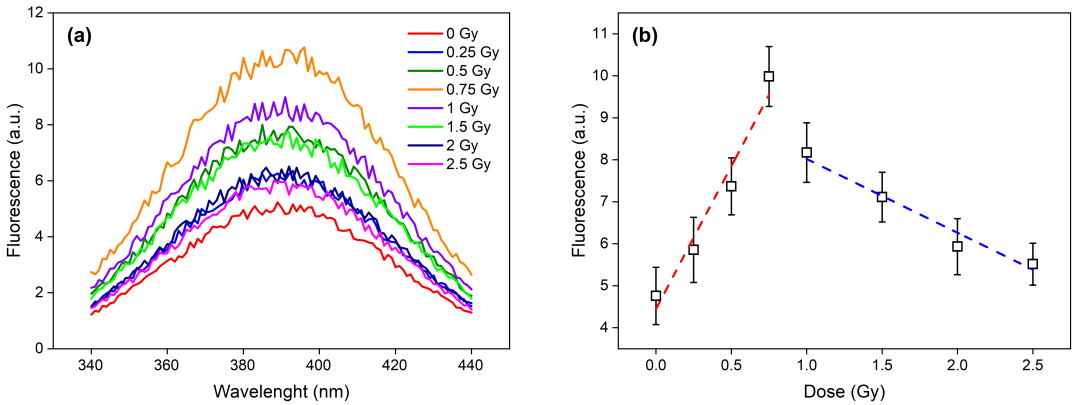

Figure 26 – (a) Fluorescence spectra of samples irradiated with doses from 0 to 2.5 Gy; (b) Maximum fluorescence intensity as a function of the absorbed dose.

irradiation. The fluorescence emission detected for the non-irradiated sample reinforces this hypothesis, suggesting that the nuclei formed in the chemical step are in the nanocluster size range. The increased fluorescence intensity for doses up to 0.75 Gy indicates that nucleation is still predominating over growth, leading to the production of more nuclei/nanoclusters in solution. Consequently, in the 0 to 0.75 Gy dose range, there is an increase in the amount of nuclei. As the dose increases, growth stars taking place, resulting in decreased fluorescence intensity due to the consumption or growth of the nanoclusters, leading to larger and non-fluorescent silver nanoparticles (above the nanocluster range). These results indicates that the nanoclusters plays an important and crucial role for particle growth as an intermediate nanoparticle state as well as for dosimetric applications, once there is a clear relationship between the nanocluster fluorescence intensity and the absorbed dose.

The data in the Figure 26(b) can be divided in two regions: the first one related to the increase in the fluorescence signal (in our hypothesis, associated formation of new nanoclusters) and the second one related to the decreased fluorescence (due to the consumption and/or growth of the nanoclusters to generate nanoparticles). It is worth noting that the dose range related to increased fluorescence intensity (0 - 0.75 Gy) coincides with the prevalence of nucleation (nanocluster formation) as pointed by Figure 23(b). Moreover, the dose range related to the decreased fluorescence intensity (1 - 2.5 Gy) coincides with the appearance of the LSPR band in the same figure, associated with the nanocluster growth and formation of plasmonic nanoparticles. Together, the UV-vis and fluorescence results undoubtably unveil the nucleation and growth mechanisms associated to the nanoparticle formation by this radiolytic microreaction besides allowing new possibilities for radiation detection and dosimetry.

Considering these two regions for dosimetry purposes, the sensitivity, linearity and MDC were estimated. The slope of the curve, in the first region (increased fluorescence), is 3.4 $\pm$ 0.5 a.u. The Standard Error for the background measurement (0 Gy) was 0.4 a.u.,

and the respective MDC is 1.1 units. Thus, the MDD is 0.20 Gy. Thus, the measurement at 0.25 Gy (6.114) is valid, and the "fluorescence dosimeter"presents a minimum detectable dose lower than the absorbance dosimeter, besides being more reliable for measuring low doses from 0.25 to 0.75 Gy. More importantly, this result reveals multimodal dosimeter never reported before, furnishing dosimetric information by both fluorescence and UV-vis spectroscopy.

Silver nanoclusters were extensively produced on glass substrates on the past years for several applications. The basic principle on their formation is based on the doping of glasses, such as silicate and zinc oxide, with silver atoms by ion exchange. Then, with an energy input from laser or gamma-irradiation, the silver ions reduce and aggregate, forming fluorescent clusters. This process, known as radiophotoluminescence, once the photoluminescence only takes place after irradiation with ionizing radiation, is largely used for ionizing radiation dosimetry. According to the literature, the Ag^+ ions in glasses present a characteristic emission band approximately at 375 nm, which is attributed to the transition $4d^9 5s \rightarrow 4d^{10}$ (90). Once this band is forbidden for free ions (91), we speculate that the fluorescence from our samples originates from Ag^+ ions in the clusters. Therefore our detectors could be thought as a radiophotoluminescent dosimeters based on aqueous dispersions instead of the glass, which has never been previously reported. Because water is the most abundant component in our system, due to its low effective atomic number, the dosimeter developed here can be considered as tissue-equivalent, great advantage compared t the glass-based radiophotoluminescent dosimeters. Future studies will focus on further increasing the dosimetric sensitivity to allow personal dosimetry.

4.3 Optimization of the parameters for dosimetry

Once the results obtained by the previous experiments were promising in terms of dosimetry, the synthesis and irradiation conditions were varied, such as precursor and reducing agent concentration, dose rate, and x-ray energy, employing the same setup and analysis, in an attempt to further optimize the radiation response. As the previous experiments found the best results for $[AgNO_3] = 2$ mmol.L^{-1} and $[Na_3Ct] = 5\%$ wt for both conventional and microfluidic approaches, these parameters were taken as the starting point for optimization procedures. The irradiation was carried out considering the interval from 0 to 50 Gy to be compared with the results obtained in the previous sections in this chapter.

4.3.1 Varying the precursor concentration

The concentration of the silver nitrate was varied from 1 to 6 mmol.L^{-1}, while the sodium citrate was kept as 5% wt. The samples were irradiated with doses between 0 and 50 Gy, with a dose rate equal to 2.054 Gy/min, in the Magnum X-ray source, 48 kVp. Figure 27 summarizes the absorbance spectra for each concentration and dose.

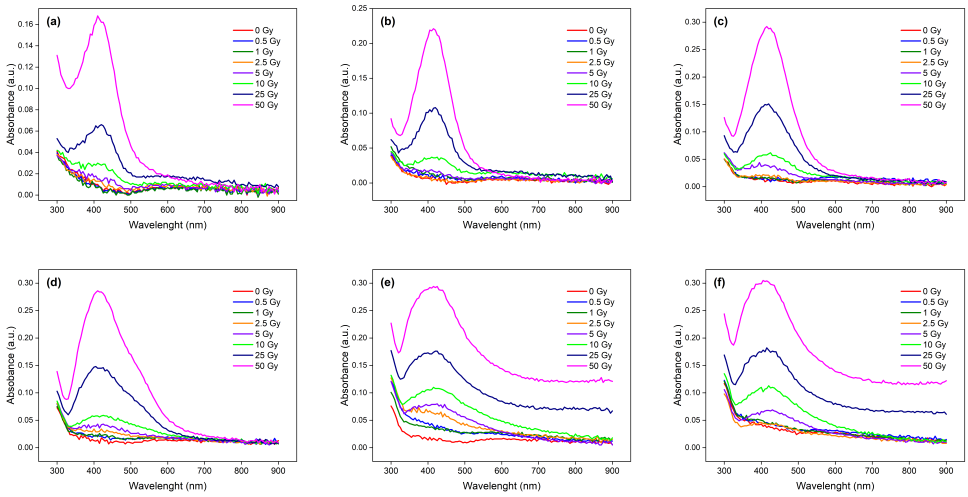

Figure 27 – Absorbance spectra for doses up to 50 Gy with silver nitrate concentrations of (a) 1 mmol.L^{-1}; (b) 2 mmol.L^{-1}; (c) 3 mmol.L^{-1}; (d) 4 mmol.L^{-1}; (e) 5 mmol.L^{-1} and (f) 6 mmol.L^{-1}. The Na_3Ct concentration was kept as 5% wt

Figure 28 presents the maximum absorbance obtained for each Ag precursor and dose. For each graph, the slope represents the sensitivity of the respective dosimeter.

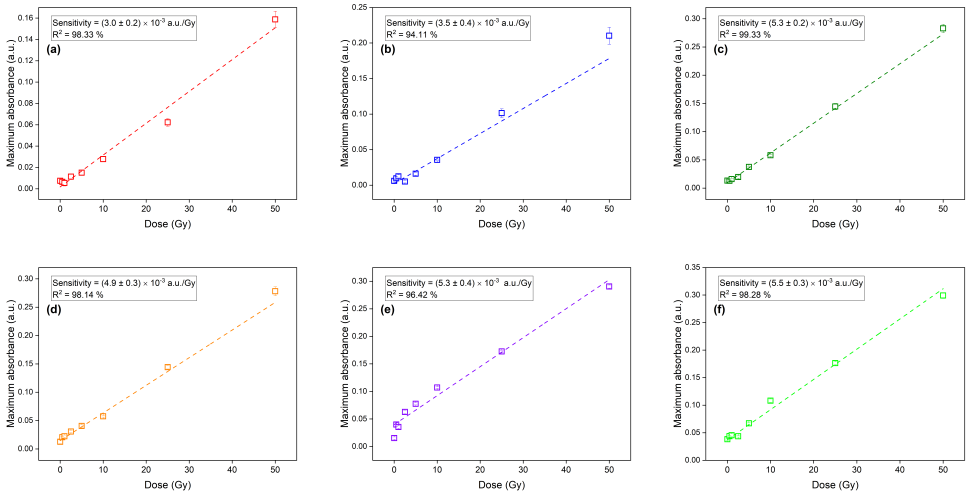

Figure 28 – Maximum absorbance for doses up to 50 Gy with silver nitrate concentrations of (a) 1 mmol.L^{-1}; (b) 2 mmol.L^{-1}; (c) 3 mmol.L^{-1}; (d) 4 mmol.L^{-1}; (e) 5 mmol.L^{-1} and (f) 6 mmol.L^{-1}. The Na_3Ct concentration was kept as 5% wt

Figure 29 shows the sensitivity (slope) and the linearity (R^2 index), for each precursor concentration. The sensitivity increases upon increasing precursor concentration up to 3 mmol.L^{-1} and then reaches a plateau. Once a higher quantity of silver ions is available in solution, the number of nanoparticles formed will also be higher. However, above this concentration (3 mmol.L^{-1}), the sensitivity stops increasing. One hypothesis to explain this result is that, although the quantity of available silver ions increased, the amount of energy deposited by the radiation remains almost constant (absorbed dose in water), so that the radiation dose becomes the limiting factor. In other words, for a concentration of 3 mmol.L^{-1}, the amount of silver ions is already enough to absorb all the products released by the water radiolysis. However, Figure 27 reveals that, upon increasing the silver concentration, the plasmon band becomes broader, indicating particle aggregation or the formation of larger and more polydisperse nanoparticles. The increased background (tail for longer wavelengths) reinforces this hypothesis. It is well known from the literature that larger and/or aggregated silver nanoparticles present weaker plasmon band intensities (lowe extinction coefficient) due to phase retardation of the electric field experienced by the free electrons at nanoparticle surface (92, 93, 94, 95). In this sense, we believe that the most likely hypothesis to explain the sensitivity plateau for $AgNO_3$ concentrations above 3 mmol.L^{-1} is the formation of larger and/or aggregated particles which, in turns, present lower extinction coefficient.

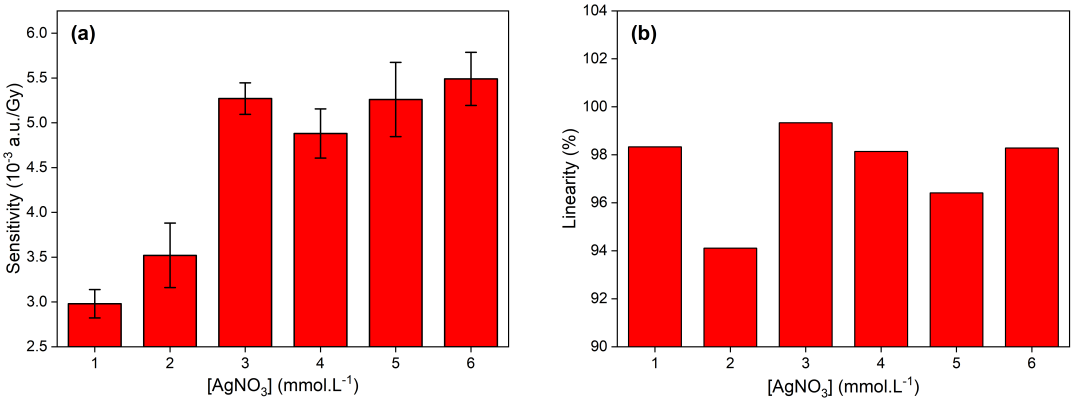

Figure 29 – (a) Sensitivity and (b) linearity of the dosimeters based on silver nanoparticles synthesis, according to the precursor concentration

Table 5 presents the values obtained for the MDC and the minimal detectable dose (MDD), as calculated by the Equation 4.1, revealing that the MDD value diminishes as the $AgNO_3$ concentration increases. The lower MDD values are probably related to the increased sensitivity. As the slope increases, the absorbance for a given dose also augments and, consequently, the signal-to-noise ratio increases, decreasing the SEM value. Therefore, the dosimetric response is reliable even for dosimeters irradiated with lower doses.

Table 5 – Sensitivity, linearity, minimal detectable change and minimal detectable dose for each precursor concentration

[$AgNO_3$]	Sens. (10^{-3} a.u./Gy)	Lin. (%)	MDC (a.u.)	MDD (Gy)
1 mmol.L^{-1}	3.0 ± 0.2	98.33	0.003	2.26
2 mmol.L^{-1}	3.5 ± 0.4	94.11	0.004	2.45
3 mmol.L^{-1}	5.3 ± 0.2	99.33	0.003	0.82
4 mmol.L^{-1}	4.9 ± 0.3	98.14	0.005	0.36
5 mmol.L^{-1}	5.3 ± 0.4	96.42	0.003	0.20
6 mmol.L^{-1}	5.5 ± 0.3	98.28	0.004	0.17

For the next experiments, the silver nitrate was used with 3 mmol.L^{-1}, as it allowed the higher linearity and one of the highest sensitivities with the lowest possible Ag concentration.

4.3.2 Varying the reducing agent concentration

Silver nitrate concentration was kept at 3 mmol.L^{-1}, and the irradiation parameters were kept as before. The reducing agent concentration was varied from 1 to 9% wt. Figure 30 shows the absorbance spectra obtained for each concentration and dose.

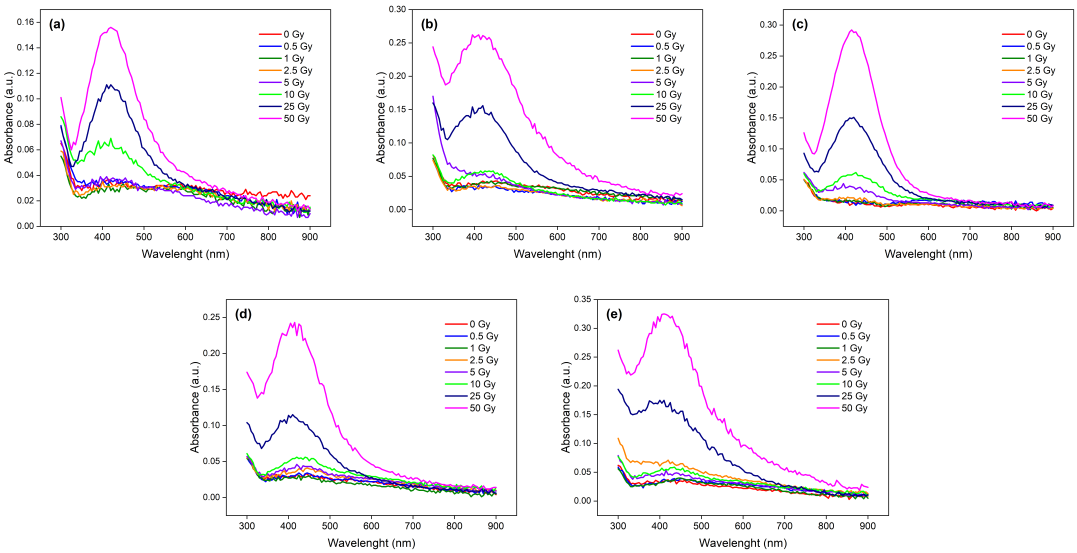

Figure 30 – Absorbance spectra for doses up to 50 Gy with sodium citrate on concentrations equal to (a) 1%; (b) 3%; (c) 5%; (d) 7% and (e) 9% wt. The $AgNO_3$ concentration was kept as 3 mmol.L^{-1}

Figure 31 presents the maximum absorbance for each sodium citrate concentration and dose. The slope represents the sensitivity for each dosimeter. Its value is presented in each graph, with the R^2 index.

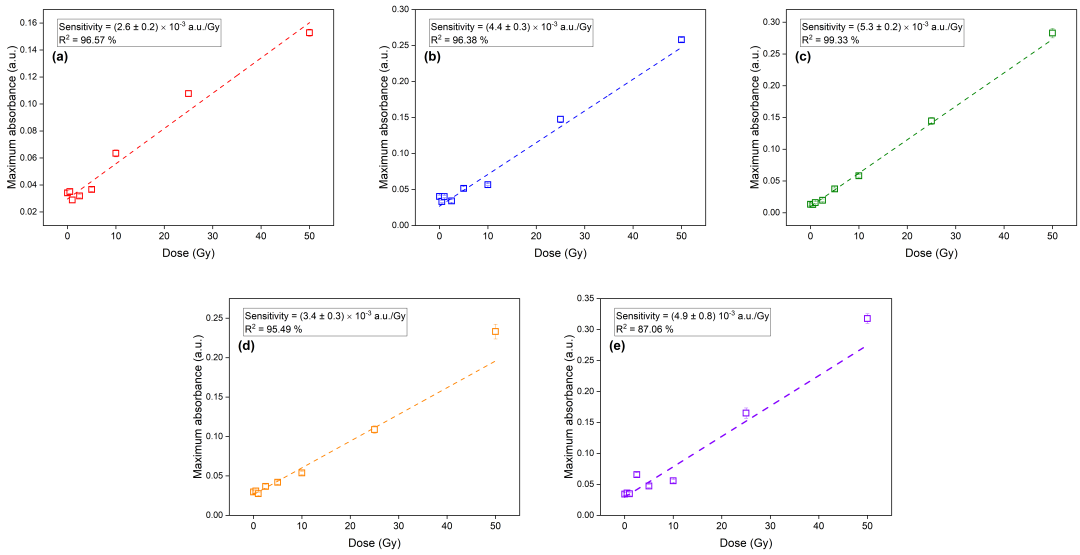

Figure 31 – Maximum absorbance for doses up to 50 Gy with sodium citrate on concentrations equal to (a) 1%; (b) 3%; (c) 5%; (d) 7% and (e) 9% wt. The $AgNO_3$ concentration was kept as 3 mmol.L^{-1}

The sensitivity increases for the concentrations up to 5% wt and then present a random behavior. The linearity (i.e. the R^2 index), however reaches a maximum for 5% wt. After that, it drastically decreases. This behavior suggests an suboptimal synthesis for high concentrations of the reducing agent, probably due to a limited nanoparticle nucleation and growth, hindered by Na_3Ct, which also acts as a capping agent in this synthesis (24, 96). For higher doses and Na_3Ct concentrations, a supralinear behavior is detected (Figures 31(d) and e) Therefore, samples with $Na_3Ct > 7\%$ wt are not suitable for dosimetry applications

Figure 32 shows the sensitivity (obtained from the slope) and the linearity (from the R^2 index) for each reducing agent concentration.

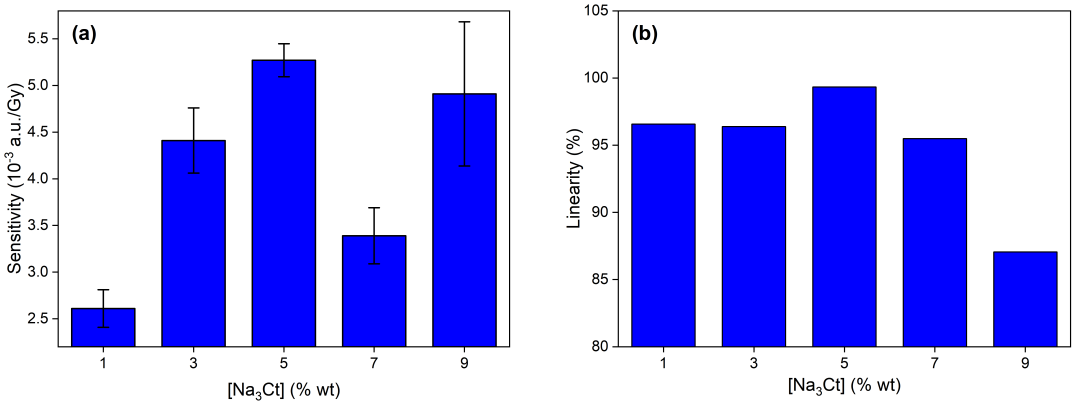

Figure 32 – (a) Sensitivity and (b) linearity of the dosimeters based on silver nanoparticles synthesis, according to the reducing agent concentration

Table 6 – Sensitivity, linearity, minimal detectable change and minimal detectable dose for each precursor concentration

[Na_3Ct]	Sens. ($\times 10^{-3}$ a.u./Gy)	Lin. (%)	MDC (a.u.)	MDD (Gy)
1%	2.6 ± 0.2	96.57	0.002	2.04
3%	4.4 ± 0.3	96.38	0.003	2.37
5%	5.3 ± 0.2	99.33	0.003	0.82
7%	3.4 ± 0.3	95.49	0.002	1.15
9%	4.9 ± 0.8	87.06	0.003	1.07

According to Table 6, the most reliable results are those with sodium citrate in concentrations above 5% wt. This concentration also presents the best sensitivity and linearity. Considering the previous section, the best combination is the one employing [$AgNO_3$] = 3 mmol.L^{-1} and [Na_3Ct] = 5% wt.

4.3.3 Varying the dose rate

With the chemical conditions optimized, the dosimeters response was analyzed upon varying dose rate. As the X-ray beam available was able to work with just one setup, the dose rate was varied by varying the distance between the tube and the sample. In our previous experiments, the distance used was 5 cm (2.054 Gy/min). Here, the distances employed were 3 cm (3.254 Gy/min), 5 cm (2.054 Gy/min) and 7 cm (1.236 Gy/min). The results regarding 5 cm were taken from the previous experiments

Figure 33 shows the spectra for each dose and dose rates used, revealing that the dose rate has a strong influence on the dosimetric response.

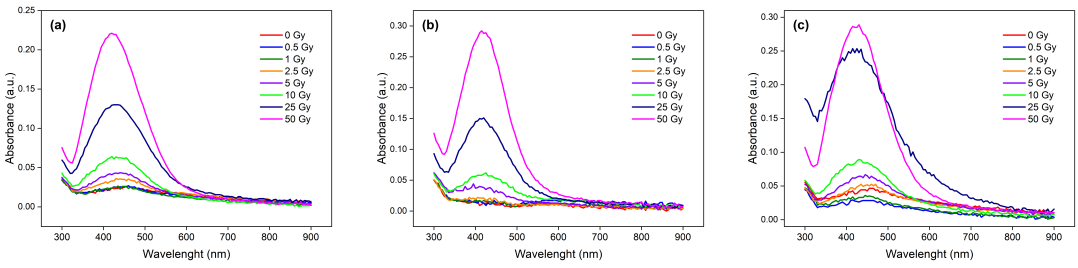

Figure 33 – Absorbance spectra for doses up to 50 Gy with dose rates of (a) 1.236 Gy/min; (b) 2.054 Gy/min and (c) 3.254 Gy/min. The samples contained 3 mmol.L^{-1} $AgNO_3$ and 5% wt Na_3Ct

Figure 34 present, for each dose rate, the maximum absorbance for each dose.

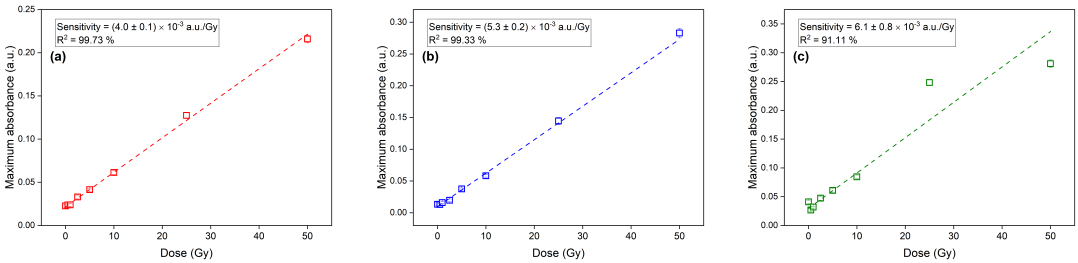

Figure 34 – Maximum absorbance for doses up to 50 Gy with dose rates of (a) 1.236 Gy/min; (b) 2.054 Gy/min and (c) 3.254 Gy/min. The samples contained 3 mmol.L^{-1} $AgNO_3$ and 5% wt Na_3Ct

The two lower dose rates produced dosimeters with lower sensitivities but with higher linearities (both have presented R^2 index greater than 99%). However, the dosimeter irradiated with the highest dose rate, altough presented the highest sensitivity, lacked linearity compared to the other ones. This result reveal that more particles are produced upon increasing the dose rate, probably because more Ag ions are simultaneously reduced, thereby favoring nucleation, i.e. once more nuclei are formed, larger amount of nanoparticles are produced. However, the higher Ag reduction rate seems to compromise the linearity.

Figure 35 and Table 7 show the sensitivity and the linearity for each dose rate. The table also presents the values obtained for MDC and MDD in each case. They show the difference between the sensitivities and linearities with more details and make the comprehension about them easier. The Table, specially, present how the MDC and MDD are strongly affected by the lineatity reduction, as the uncertainty becomes is higher. As a consequence, the dosimeters developed here are suitable for application involving dose rates below 2.054 Gy/min, but corrections should be implemented according the dose rate employed.

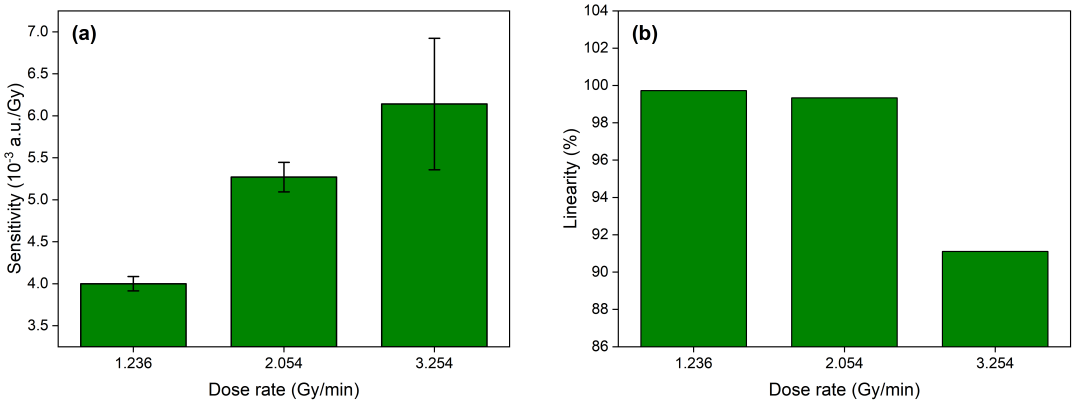

Figure 35 – (a) Sensitivity and (b) linearity of the dosimeters based on silver nanoparticles synthesis, according to the dose rate. The samples contained 3 mmol.L^{-1} $AgNO_3$ and 5% wt Na_3Ct

Table 7 – Sensitivity, linearity, minimal detectable change and minimal detectable dose for each precursor concentration

Dose Rate	**Sens. ($\times 10^{-3}$ a.u./Gy)**	**Lin. (%)**	**MDC (a.u.)**	**MDD (Gy)**
1.236 Gy/min	4.0 ± 0.1	99.73	0.002	1.11
2.054 Gy/min	5.3 ± 0.2	99.33	0.003	0.82
3.254 Gy/min	6.1 ± 0.8	91.11	0.004	0.87

4.4 Silver nanoparticle dosimeter for higher beam energies

Since the best conditions for the chemical step was determined, and the dosimetric application verified it becomes important to test the dosimeter response for different beam energies. Therefore, the efficiency of the dosimeter was evaluated for beam energies close to the radiodiagnosis range (tube voltage around 100 kVp).

First of all, to check if nanoparticles are produced when irradiated by beams provided by the Titan tube, with voltages of 60, 100 and 160 kVp (effective energies and dose rates are presented in Table 2), a 50 Gy irradiation was realized on samples with 3 mmol.L^{-1} $AgNO_3$ and 5 % wt Na_3Ct prepared by the microfluidic method. The distance between source and sample was equal to 30 cm. Figure 36 presents the absorption spectra for each kVp, revealing that, considering the experimental uncertainties, the SPR intensity does not vary with varying the tube voltage.

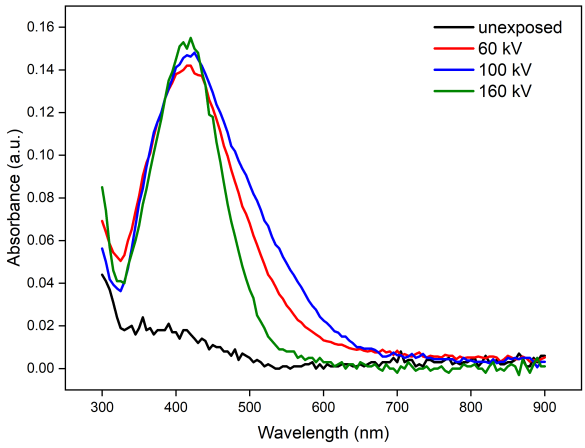

Figure 36 – Absorption spectra for the samples irradiated with 50 Gy on the Titan x-ray tube operating with different voltages. Samples contained 3 mmol.L^{-1} $AgNO_3$ and 5 % wt Na_3Ct and were prepared by the microfluidic method

On the next step, we have studied how the LSPR intensity varies with the dose. Figure 37 presents the absorption spectra for each voltage (between 60 and 160 kVp) and dose (between 0 and 50 Gy).

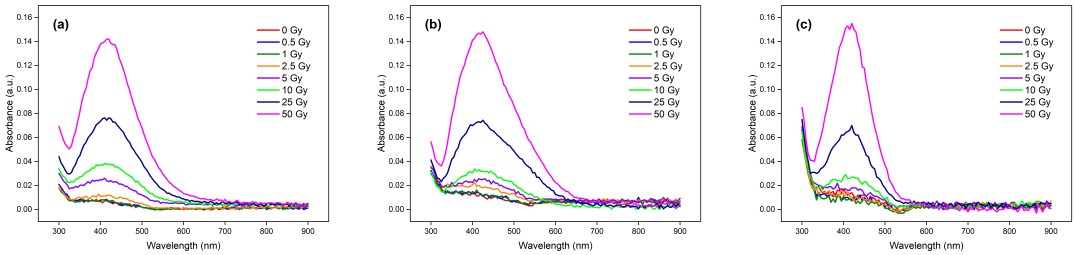

Figure 37 – Absorbance spectra for doses up to 50 Gy for the Titan tube with voltage of (a) 60 kVp; (b) 100 kVp and (c) 160 kVp. Samples contained 3 mmol.L^{-1} $AgNO_3$ and 5 % wt Na_3Ct and were prepared by the microfluidic method

Figure 38 presents the highest absorbance value obtained at the LSPR peak. The result is quite similar to the previous one, as it shows that the sensitivity, obtained from the slope in each figure, do not vary significantly with the voltage. The nanoparticles might be formed and capped rapidly, which means that the radiation is consumed for formation of new nanoparticles, instead of the growth of the existing ones. Because dose rate depends of kVp^2, the dosimetric response (LSPR intensity) seems to not depend on the dose rate for the energies used here.

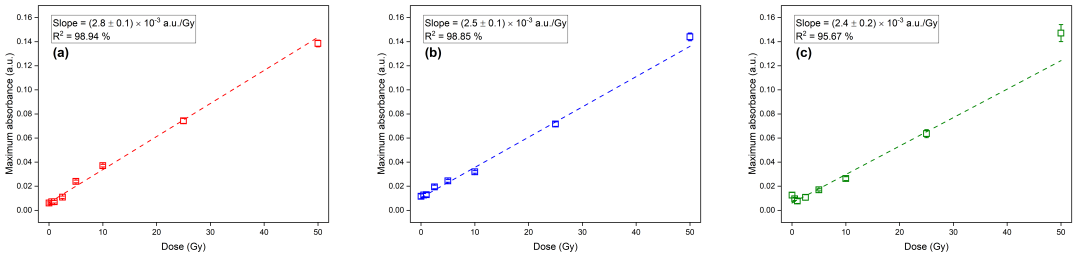

Figure 38 – Maximum absorbance for doses up to 50 Gy on the Titan tube with voltage of (a) 60 kVp; (b) 100 kVp and (c) 160 kVp. Samples contained 3 mmol.L^{-1} $AgNO_3$ and 5 % wt Na_3Ct and were prepared by the microfluidic method

4.5 Nanoparticle size dependence on beam energy

The size of the silver nanoparticles were analyzed by transmission electron microscopy to verify the influence of the beam energy on the nanoparticle size.

4.5.1 Method for analysis of the size distribution

The following images present, for each beam, the original TEM image, and the particle counter. The scale is presented for each case, in the respective caption.

4.5.2 Particle size distribution of the nanoparticles from samples irradiated with the Magnum X-ray source

Figure 39 shows the original TEM image obtained for the sample prepared by the microfluidic method, containing 3 mmol.L^{-1} $AgNO_3$ and 5 % wt Na_3Ct, and irradiated with the 48 kVp beam. The image presents a large population of small particles, with few nanometers radius, relatively near to each other, but individually detectable. There are many tiny nanoparticles relatively well distributed in the image, which could be associated to the clusters produced during the chemical stage. Finally, few particles with radius in the order of tens of nanometers are observed. The high amount of smaller particles indicates a predominance of the nucleation process over the growth, even with the latter having an influence on the final result.

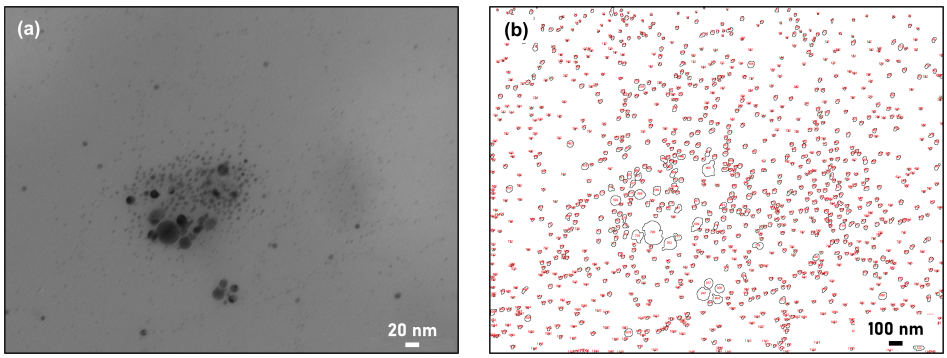

Figure 39 – TEM image from samples irradiated with the 48 kVp beam (a) original image and (b) particle analyzer image. Samples contained 3 mmol.L^{-1} $AgNO_3$ and 5 % wt Na_3Ct and were prepared by the microfluidic method

The particle size distribution (PSD) is presented in Figure 40. To this end, the area (A) of each nanoparticle was calculated by the ImageJ software, and the radius was obtained by Equation 4.2, considering the nanoparticles as spheres. There is an evident predominance of the very small nanoparticles (smaller than 5 nm) in the distribution, and few ones larger than 7 nm, which are those present in the agglomerate in the image.

$$r = (A/\pi)^{1/2} \tag{4.2}$$

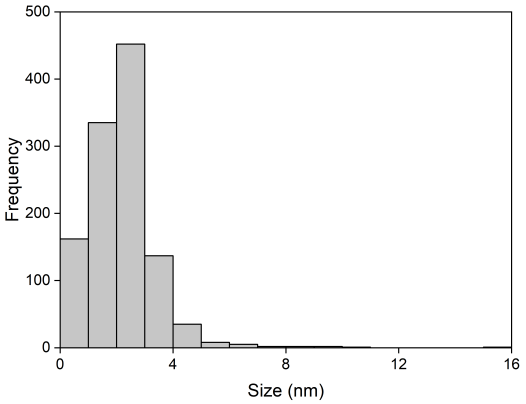

Figure 40 – Particle size distribution (PSD) of the nanoparticles produced in the 48 kVp beam

In order to find a more detailed distribution, the nanoparticles larger than 5 nm were removed from the counts, leading to Figure 41(a). Based on that distribution, the mean size of the nanoparticles was calculated by a Gaussian distribution, presented in Figure 41(b). The result shows that the size of the nanoparticles is around 3 ± 1 nm, with 96% of confidence. The distribution is highly dispersed, but composed mostly of nanoparticles smaller than 5 nm, as expected considering that the nucleation was found to dominate over the growth.

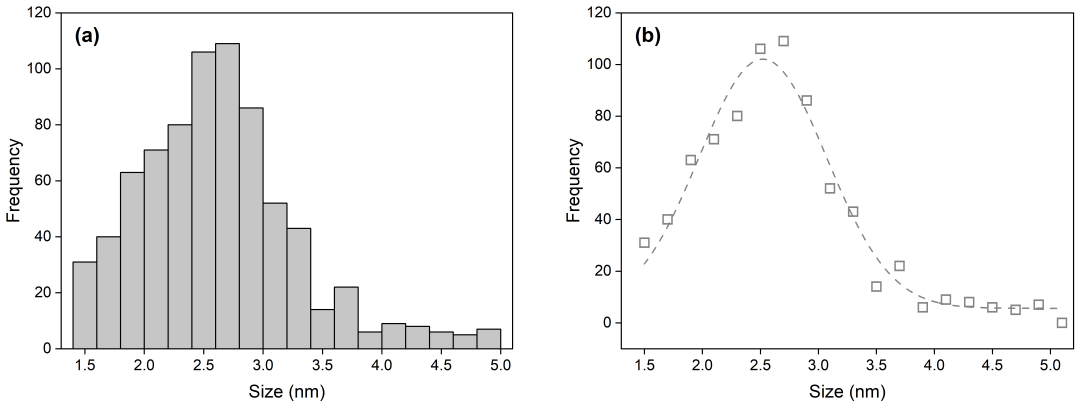

Figure 41 – (a) PSD of the nanoparticles from samples irradiated with the 48 kVp beam; (b) Gaussian distribution approximation of the nanoparticles size

4.5.3 Particle size distribution of the nanoparticles from samples irradiated with the Titan X-ray tube

The same methodology for treatment of the images and analysis of the size distribution were used for the Titan tube beams.

Figure 42(a) shows the image obtained for the sample irradiated with the Titan x-ray tube, operating with 60 kVp. Figure 42(b) show the nanoparticles counted. The synthesized nanoparticles agglomerate into islands, but each individual particle is still distinguished, suggesting the absence of coalescence processes. A significant portion of these agglomerated particles (without coalescence) in tree-like structures close to the copper grid walls (not shown).

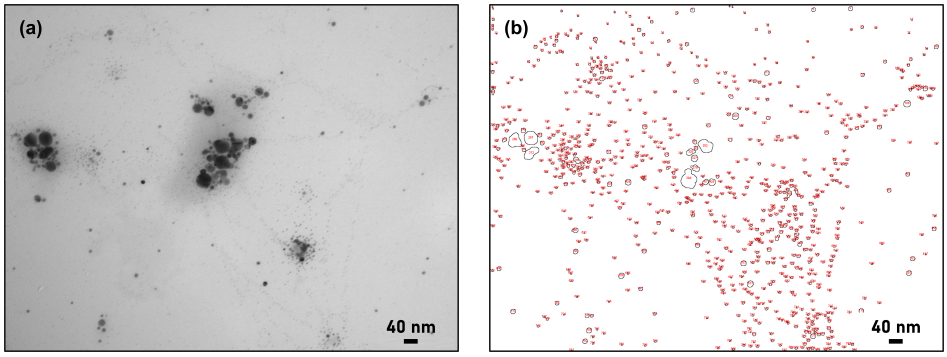

Figure 42 – TEM image obtained for size distribution analysis of the nanoparticles produced on the Titan x-ray tube with 60 kVp (a) original image; and (b) particle analyzer image. Samples contained 3 mmol.L^{-1} $AgNO_3$ and 5 % wt Na_3Ct and were prepared by the microfluidic method

Figure 43 show the size distribution of the nanoparticles. The sample is composed mainly for small nanoparticles (90% of them are smaller than 25%).

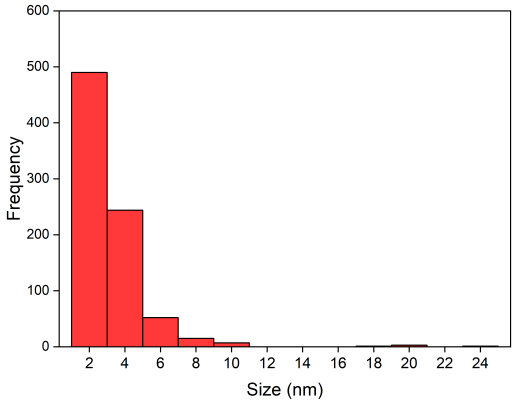

Figure 43 – Size distribution of the nanoparticles produced on the 60 kVp beam

As in the first case, it was necessary to limit the data to calculate the mean size. The Figure 44(a) shows the corrected distribution and the Figure 44(b) shows the counts per size, approximated by a Gaussian distribution. According to the fit, the mean size is 3 ± 1 nm, with 96% of confidence. This result supports what was seen on the image: the nanoparticles sizes are strongly concentrated on the lower values. This is an indication that the radiolytic species produced were homogeneously consumed on nanoparticle growth, leading to small particles.

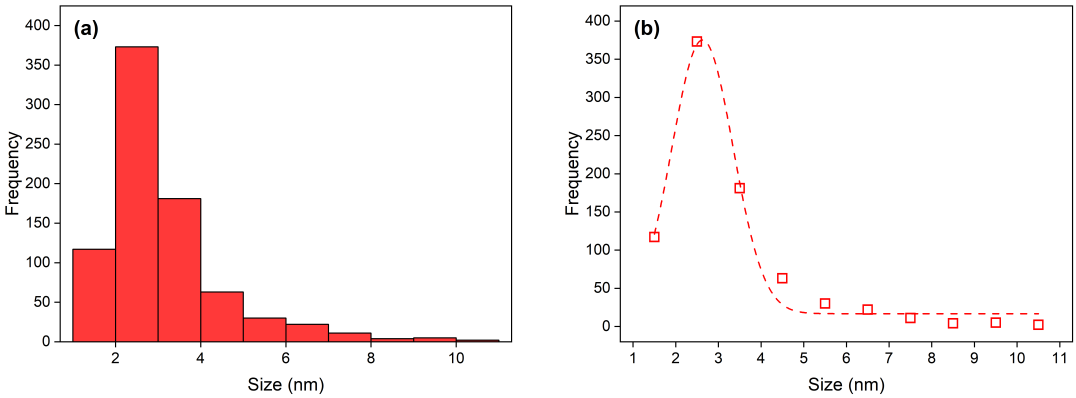

Figure 44 – (a) Size distribution of the nanoparticles produced on the 100 kVp beam and (b) Gaussian distribution approximation of the nanoparticles size

It is noteworthy that the number of detected nanoparticles reduced 15 % compared to the 48 kV beam. That result, and the increase on mean size, suggest that the synthesis with this higher energy favors growth and strongly coalescence. If this tendency is confirmed, an increased beam energy leads to increased growth rates.

For the sample irradiated with 100 kVp beam, Figure 45(a) shows the actual image obtained from the solution. These particles are well dispersed on the image, and no aggregation was found. Figure 45(b) presents the nanoparticles detected on the image by the method used. This image shows not only the good particle dispersity but also a higher polydispersity.

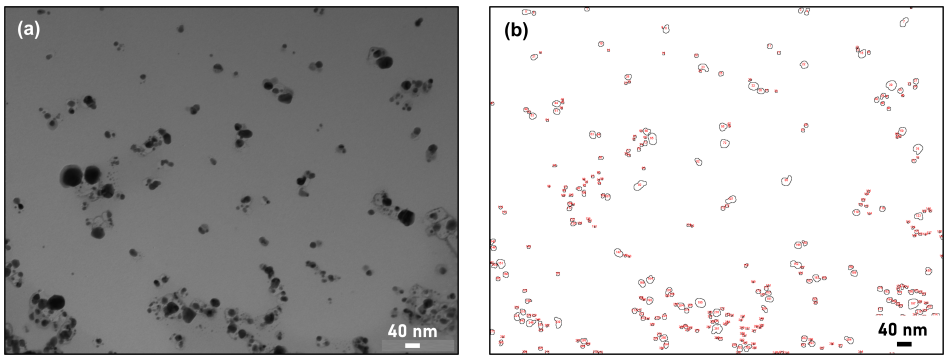

Figure 45 – TEM image obtained for size distribution analysis of the nanoparticles produced on the Titan x-ray tube with 100 kVp (a) original image; and (b) particle analyzer image. Samples contained 3 mmol.L^{-1} $AgNO_3$ and 5 % wt Na_3Ct and were prepared by the microfluidic method

Figure 46(a) shows the size distribution of the particles from the former images. As seen in the image, the size distribution is broad, with an average size of 4 $\pm$ 3 nm and 77 % confidence (Figure 46(b)). The fact that both the mean size and the PSD increased compared to the 60 kV beam suggests that increased energy and/or dose rate may favor growth.

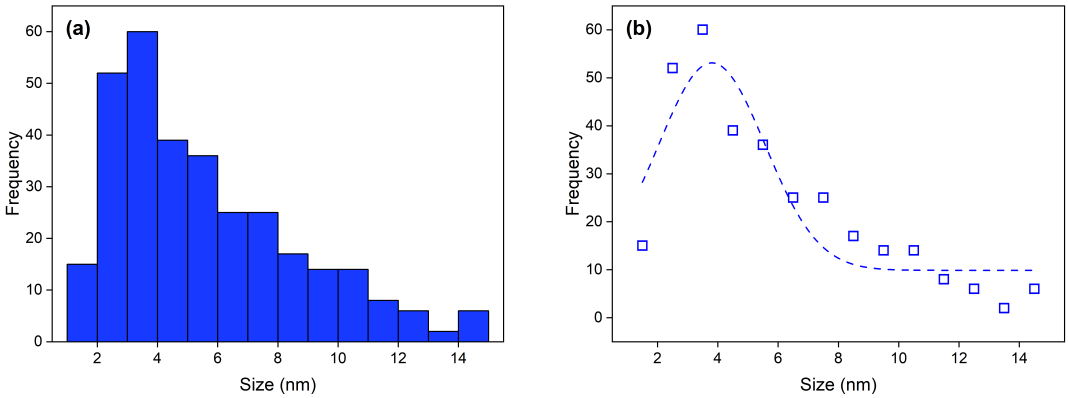

Figure 46 – (a) Size distribution of the nanoparticles produced on the 100 kVp beam and (b) Gaussian distribution approximation of the nanoparticles size

Finally, for the 160 kV beam, some nanometer sized agglomerates were found (like the one in Figure 47(a)). These aggregates are a strong evidence of our hypothesis, that the growth and/or agglomeration are favored by the increased energy and/or dose rate. The size distribution is presented in Figure 47(b).

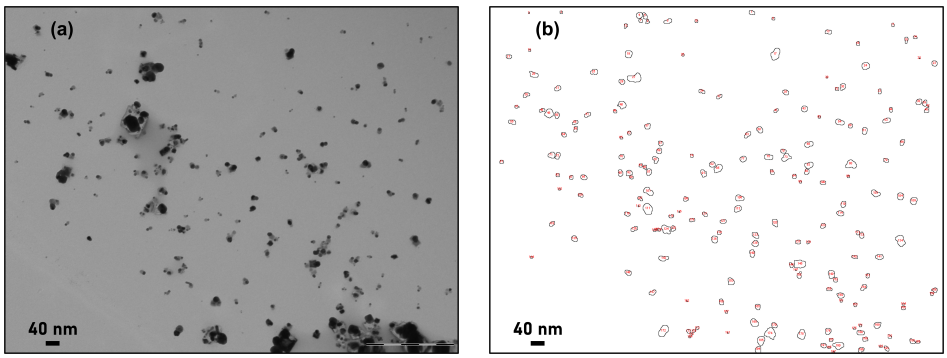

Figure 47 – TEM image obtained for size distribution analysis of the nanoparticles produced on the Titan x-ray tube with 160 kVp (a) original image; and (b) particle analyzer image. Samples contained 3 mmol.L^{-1} $AgNO_3$ and 5 % wt Na_3Ct and were prepared by the microfluidic method

The particles in this sample are large probably due to the favored growth process by employing higher dose rates and energy. Considering the quasi-spherical particles in the surroundings, outside and/or embedded in the aggregate - the distribution presented a well-defined mean value (Figure 48(a)). The PSD is analyzed on Figure 48(b). The value obtained is 6 ± 3 nm, with 96% of confidence.

These analyses led us to a strong hypothesis of the nanoparticle synthesis process influenced by irradiation: as the energy and dose rate increase, the growth process becomes more intense, leading to larger nanostructures. This could be a limitation on the use of X-ray beams with higher energies, although the sensitivity observed for each voltage do not vary significantly.

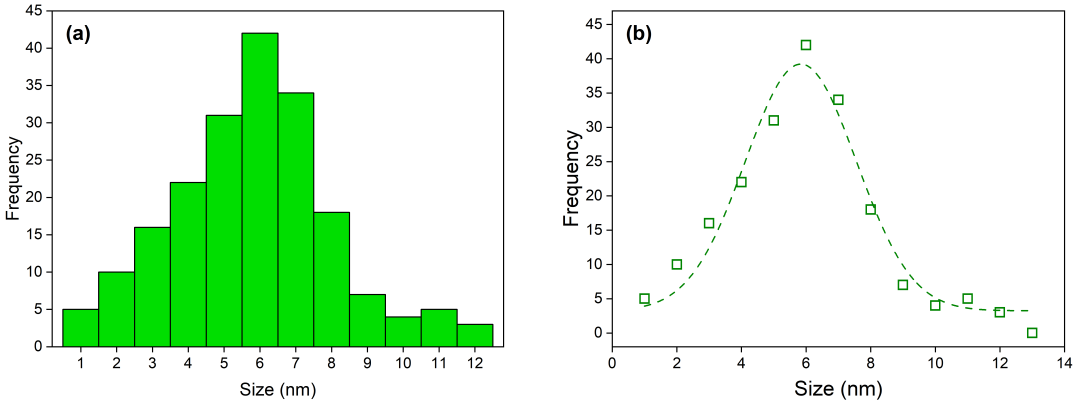

Figure 48 – (a) Size distribution of the nanoparticles produced bt the 160 kVp beam and (b) Gaussian distribution approximation of the nanoparticles size

4.6 Partial conclusions

The dosimeter based on silver nanoparticles (AgNP) was developed according to one of the simplest reported reactions for the synthesis of AgNP. The silver nitrate ($AgNO_3$) was used as a silver precursor and the trisodium citrate ($C_6H_5O_7Na_3$, or Na_3Ct) was employed as the reducing agent. Three techniques for the combination of the chemical reaction followed by an irradiation process were developed. In the first one, the reactants were mixed at room temperature before irradiation. In the second one, the reactants were mixed at approximately 100 °C and then let to cool down to room temperature. In the third one, the mixture occurred in a microfluidic reactor, in order to achieve a better control on the physical parameters that could affect the synthesis process.

As a result, an absorption band was observed for the three methods, around 420 nm, which is characteristic of silver nanoparticles. However, the first two methods could not avoid the presence of a LSPR band even without irradiation, indicating the nanoparticle formation during the chemical step. This is not desirable, because the dosimetric capability will be compromised by a strong background signal in non-irradiated samples. The third method was the one in which the absorbance from non-irradiated samples was absent while the signal generated after irradiation was intense, indicating the expected better control of the synthesis. This technique also provided the more sensitive dosimeter, and consequently was adopted for the optimization studies. The highest sensitivity was obtained for $[AgNO_3] = 3$ mmol.L^{-1}, $[Na_3Ct] = 5\%$. The dosimeter was then irradiated with higher energy beams. The sensitivity did not change upon varying the irradiation beam energy, indicating that the dosimeter is viable to several beam qualities commonly used in clinical applications.

An unexpected result with the microfluidic approach was the viability of dosimetry with silver nanoclusters. These clusters are probably an intermediate state before the formation of the silver nanoparticles, playing the role of seed to the formation of the

particles. The clusters were only detectable for samples produced by the microfluidic approach, probably due to the better temperature and reaction time control allowed by this method, avoiding the early formation of nanoparticles. The clusters were detectable when the samples were irradiated with low doses (up to 2.5 Gy), providing two ways to assess the radiation dose: UV-vis and fluorescence spectroscopies. By measuring the absorbance in the LSPR, the sensitivity for the lower dose range (up to 2.5 Gy) was higher than the obtained for the higher dose interval (up to 50 Gy): (5.8 *versus* 2.1 $\times$ $10^{-}3$ a.u./Gy), with MDD of 1 Gy, and decreased background, evidencing the importance of the microfluidic route implemented here. By fluorescence spectroscopy, a sensitivity of 3.4 $\pm$ 0.5 a.u./Gy was achieved for the 0.25 to 0.75 Gy dose range with a MDD = 0.25 Gy, even lower than the obtained for UV-vis spectroscopy.

5

Dosimetry based on the synthesis of gold nanoparticles

In this chapter, the main results on the radiation-induced synthesis of gold nanoparticles will be presented and discussed. In the first section, a synthesis developed for γ-ray dosimetry will be verified for dose assessment with x-ray beams. In the second section, the influence of synthesis parameters on the absorbance intensity and particle size distribution will be studied. Finally, the applicability of that synthesis for other energies will be evaluated.

5.1 Developing the synthesis route

The synthesis is based on the reduction of gold ions by ascorbic acid from trivalent to monovalent forms and then, the reduction to the neutral form upon irradiation with x-rays. In the first step, the gold precursor (chloroauric acid - $HAuCl_4$) was mixed with CTAB. The latter is responsible to template the former, and to provide the ionic changing, from Cl^- to Br^-. Finally, the ascorbic acid is used to partially reduce the ions before the irradiation. Figure 49 presents how the solution change as each step is realized. The yellow sample (a) corresponds to the solution after the mixture of the precursor and the CTAB. As the ascorbic acid is added, the solution change from yellow to colorless (b) and then, when irradiated, the sample acquires the purple color (c), which is characteristic of gold nanoparticles

The first experiments were concerned with the synthesis control and with the verification of the viability for irradiation with x-rays. A peak on approximately 510 nm is found when the samples are irradiated with gamma rays but, since we employed X-rays (i.e., lower energy), a change on the peak position could be expected. To verify this, two solutions were produced. The first one is composed by the gold precursor and CTAB (Figure 49 (a)). The second one is composed by these two components and the ascorbic

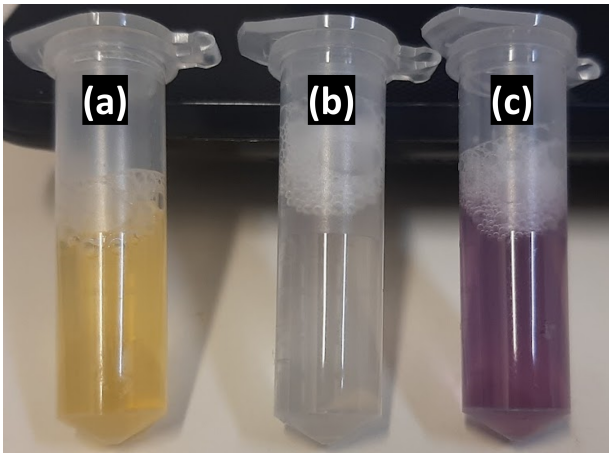

Figure 49 – Variation of the samples color after (a) mixture with CTAB; (b) addition of AA; and (c) irradiation with the 48 kVp X-ray beam

acid (Figure 49 (b)). Both the samples had its absorbance spectra measured and were irradiated with 50 Gy, at 2.054 Gy/min.

Figure 50 shows how the spectra of each solution changed before and after the irradiation. The yellow solution (without ascorbic acid) barely changed, and the obtained spectra were very similar. This happened because the direct reduction of Au^{+3} to Au^{0} is very difficult and must not occur with the low dose employed. The solution with ascorbic acid (i.e., the one where the reduction occur from Au^{+3} to Au^{+1}) changes drastically after irradiation, result in in a pronounced peak at 550 nm, characteristic of gold nanoparticles. The position of the peak for these nanoparticles is redshifted in relation to the reported nanoparticles irradiated with γ-rays (48) (which peak is at 510 nm). In this case, the redshift may indicate that larger nanoparticles were produced upon x-ray irradiation (97, 98).

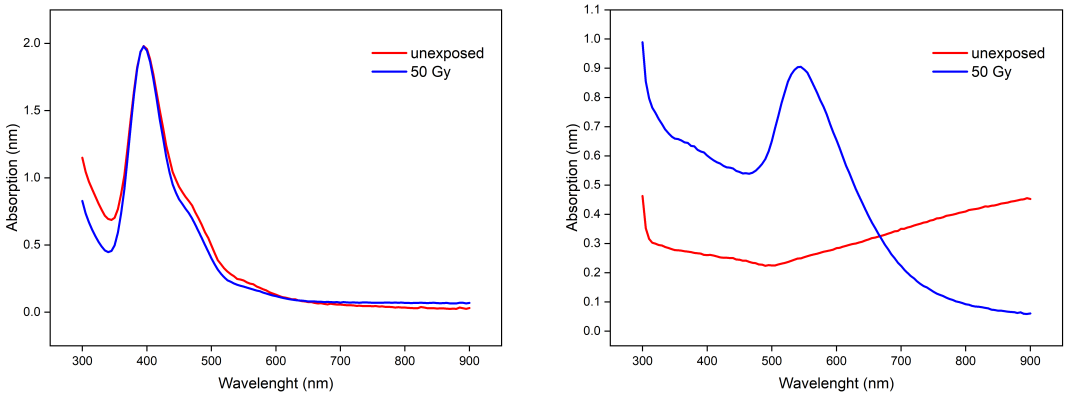

Figure 50 – Spectral variations upon irradiation of the samples containing (a) $HAuCl_4$ 10 mmol.L^{-1} and CTAB 50 mmol.L^{-1}; and (b) $HAuCl_4$ 10 mmol.L^{-1}, CTAB 50 mmol.L^{-1} and AA 10 mmol.L^{-1}

5.2 Optimizing synthesis parameters

Since nanoparticle formation is also possible upon x-ray irradiation it is important to verify the influence of the chemical and the irradiation parameters on the UV-vis spectra. To avoid a high consumption of the gold precursor, these experiments were carried out before the dosimetry tests. Once the best conditions are found, it would be able to study the use of this device for different doses.

5.2.1 Optimizing the gold precursor concentration

The concentration of $HAuCl_4$ was varied between 1 and 10 mmol.L^{-1}. All the other reactants concentrations were kept constant. For each Au concentration, the absorbance spectra and PSD were recorded. Figure 51(a) presents the spectra obtained for each concentration after a 50 Gy irradiation whereas Figure 51(b) depicts the maximum absorbance of the SPR peak. These figures reveal an increased absorbance as the concentration of $HAuCl_4$ increases, suggesting that more nanoparticles are produced when more gold is available.

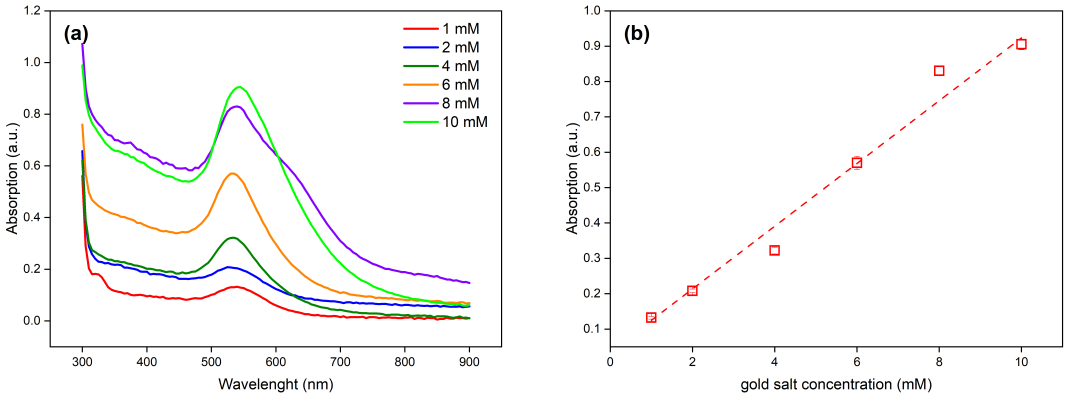

Figure 51 – Variation of the intensity of SPR band over change on gold precursor concentration (a) absorbance curves and (b) maximum absorbance on LSPR band. CTAB was kept in 50 mmol.L^{-1} and ascorbic acid was used in 10 mmol.L^{-1}

Figure 52(a) depicts the PSD and Figure 52(b) the average particle size obtained for each precursor concentration. The particle size diminishes upon increasing the Au concentration, probably because more gold ions are simultaneously reduced to Au^0, thereby favoring nucleation over growth. In this sense, more gold seeds will be available and, consequently, a larger quantity of particles will be formed, resulting in a rapid consume of the precursor and, consequently, smaller particle size.

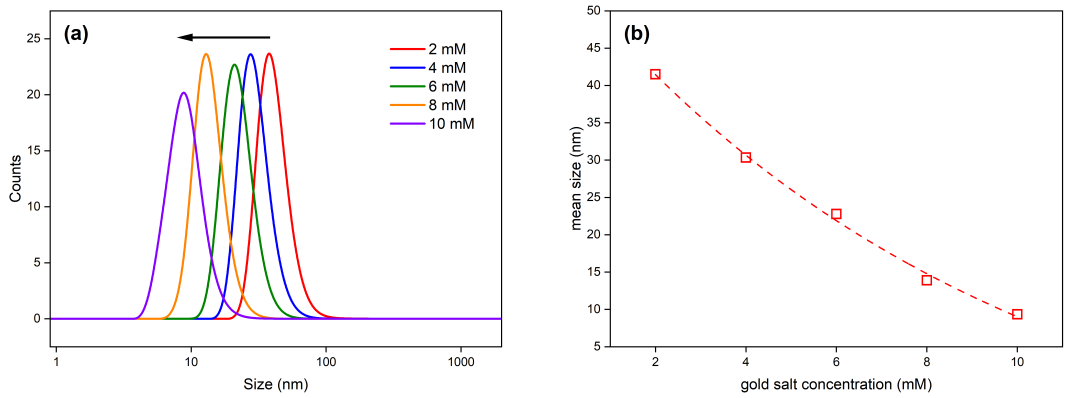

Figure 52 – (a) Size distribution of the nanoparticles produced, for each $HAuCl_4$ concentration; (b) Average particle size as a function of $HAuCl_4$ concentration

5.2.2 Optimizing the ascorbic acid concentration

The ascorbic acid concentration was varied between 2 and 10 mmol.L^{-1}. Figure 53(a) presents the spectra, and Figure 53(b) depicts the LSPR intensity for each AA concentration, revealing an increased absorbance upon increasing AA concentration, probably because the gold ions will be more likely to be reduced to Au^0.

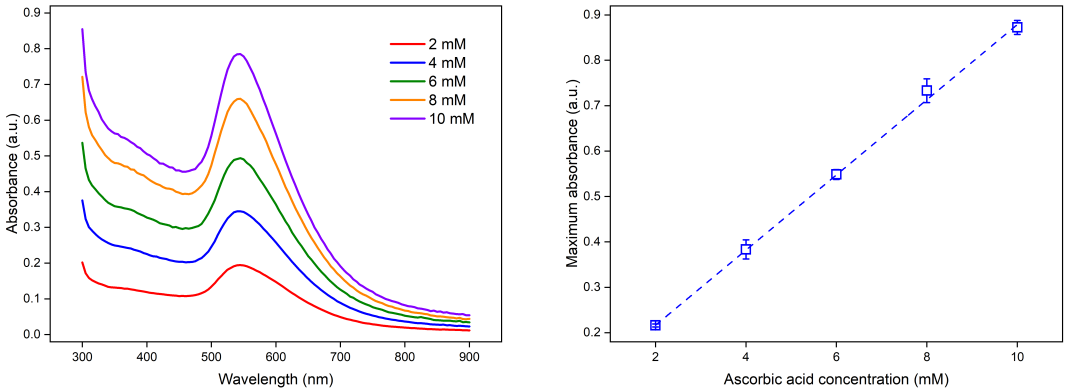

Figure 53 – (a) Absorption spectra of the nanoparticles, for each ascorbic acid concentration; (b) Maximum absorbance for each AA concentration. $HAuCl_4$ was used in 10 mmol.L^{-1}, while CTAB was used with 50 mmol.L^{-1}

Figure 54 reveals that the particle sizes decrease by increasing the AA concentration, in agreement with blue-shift observed in Figure 54(a). The particle size reaches a minimum value for a 6 mmol.L^{-1} AA concentration. After that, further increase in AA concentration does not alter the particle sizes.

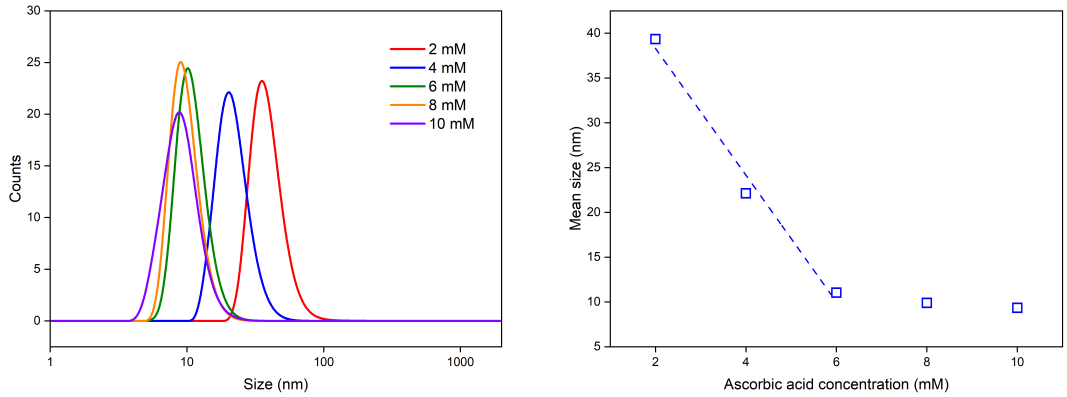

Figure 54 – (a) Size distribution of the nanoparticles produced, for each ascorbic acid concentration; (b) Variation of mean size with AA concentration

5.2.3 Optimizing the dose rate

The concentrations of the gold precursor and the ascorbic acid were kept at 10 mmol.L^{-1} and the dose rate was varied from 0.274 to 3.254 Gy/min. To this end, the distance between the beam and the sample was varied from 3 to 15 cm. Figure 55(a) presents absorbance spectra for the different dose rates employed. Figure 55(b) reveals that the absorbance increases when the dose rate is increased.

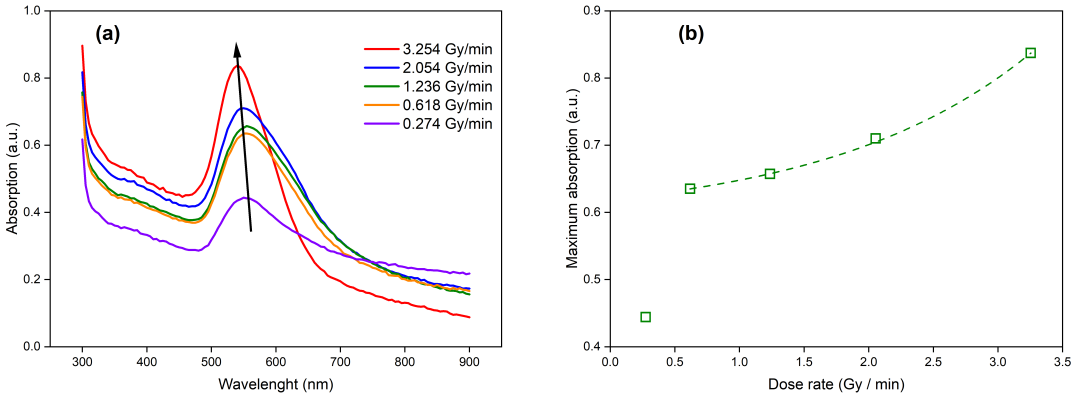

Figure 55 – (a) UV-vis spectra of the nanoparticles irradiated with the same radiation dose and energy, but under different dose rate; (b) Absorbance as a function of the dose rate

This result evidences the influence of the reduction rate on the nanoparticle formation. With more gold ions being simultaneously reduced, nucleation is favored and, consequently, more nanoparticles will grow. As a consequence, smaller particles should be formed, which is corroborated by the blue-shift upon increasing the dose rate, as observed in Figure 55(a). In the same sense, when the dose rate is lower, growth become more significative, leading to fewer particles of larger sizes. The reduced concentration of particles along with their larger sizes could drastically and synergistically reduce the

nanoparticles extinction coefficient, thereby explaining the abrupt absorbance reduction detected for the sample irradiated with the lowest dose rate (0.274 Gy/min), as observed in Figure 55(b)

This hypothesis is supported by the DLS results (Figure 56). When low dose rates are employed, larger nanoparticles are formed, indicating that the growth process predominates. Similarly, when high dose rates are used, the nanoparticles get smaller, as the nucleation process predominates over growth. The PSD also explains the shift in the absorbance peak for each dose rate: as the nanoparticles increases, the respective LSPR band shifts to red. This result is in agreement and reinforced the ones observed in the case of silver nanoparticles (section 4.3.3).

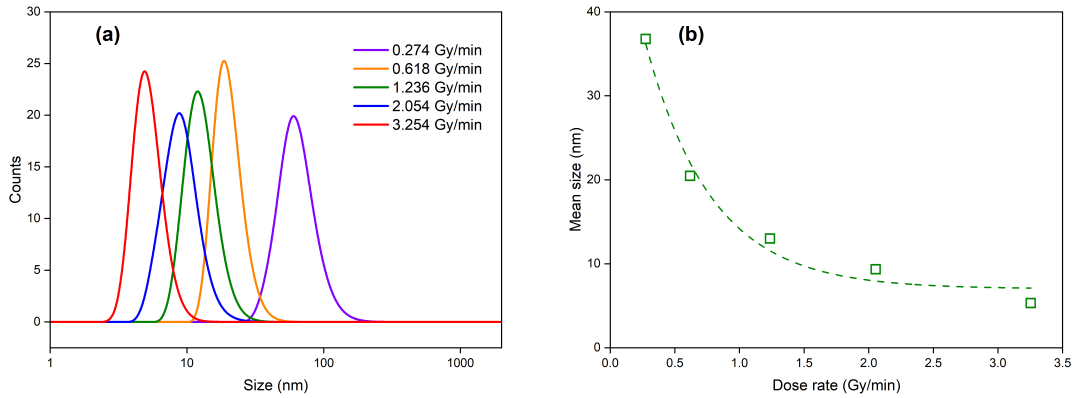

Figure 56 – (a) Particle size distribution of the nanoparticles produced under different dose rate; (b) Average particle size as a function of the dose rate

5.3 Application of the synthesis for different beam energies

Since the synthesis was verified to work with x-rays in tubes operating with tens of kilovolts, the industrial x-ray source was used to analyze how the voltage (energy) can impact the gold nanoparticles formation. The concentrations of all the precursors were used as on the first experiments. The voltage was changed from 60 to 160 kV (Table 2).

Figure 57 presents the absorption spectra for each energy and the respective maximum LSPR band. As expected, the LSPR band intensity increases upon increasing the beam energy, since the dose rate will also be augmented. The blue shift with the increasing energy is also verified, in agreement with the previous results. Finally, the maximum absorption (Figure 57(b)) were well-adjusted to a quadratic model.

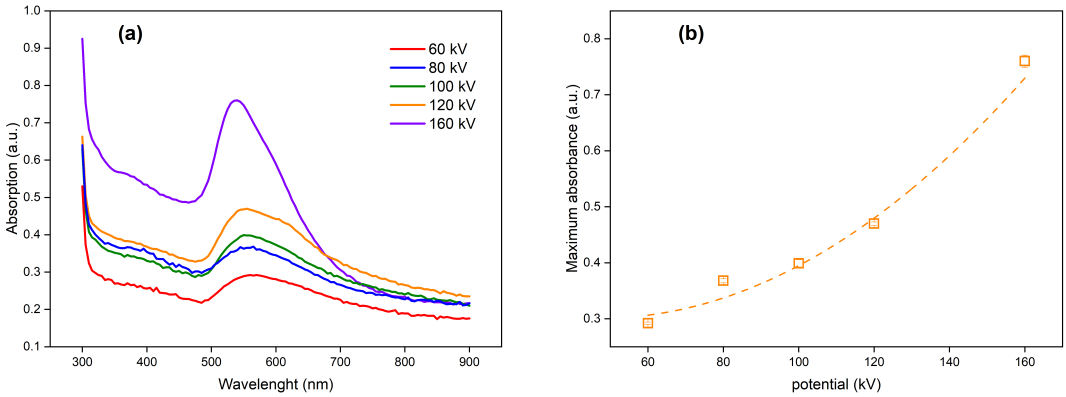

Figure 57 – (a) Absorption spectra of the nanoparticles, for each tube voltage; (b) Maximum absorbance for each tube voltage

Figure 58 presents the results for the DLS measurements. The expected behavior was a decreased mean size as the energy increases, which would support our previous results. However, an increase in the size was observed for the voltages up to 100 kV. Also, the function is not well completely fitted by any model (the polinomial fit exemplifies that). In this case, that behavior might be influenced by the impact of the tube voltage on nucleation and growth. For voltages up to 100 kV, the nucleation rate is probably increasing but the growth is predominant. As the tube voltage increases (and so do the dose rate), the nucleation becomes predominant and, as more nuclei are formed, their growth is limited, which could explain the decreased mean size.

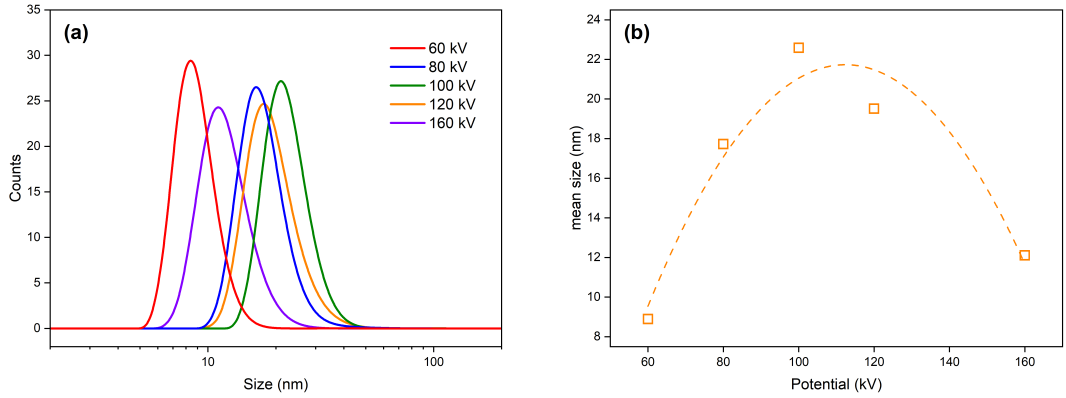

Figure 58 – (a) Size distribution of the nanoparticles produced, for each tube voltage; (b) Variarion of mean size with the tube voltage

5.4 Dosimetry with gold nanoparticles

As the synthesis of gold nanoparticles mediated by radiation was studied and the influence of each parameter was verified, we were able to measure dose with this sensor.

5.4.1 Dosimetry with the beam from the Magnum x-ray source

The dosimetric measurements were first carried out with the samples irradiated with the Magnum 48 kVp source. The dose was varied from 0 to 50 Gy. Figure 59 reveals that LSPR band is detected for doses as low as 0.5 Gy and its intensity increases up to 5 Gy, reaching a plateau after that. Also, it is worth noting that the position of the band did not significantly change, suggesting that particle size is kept constant.

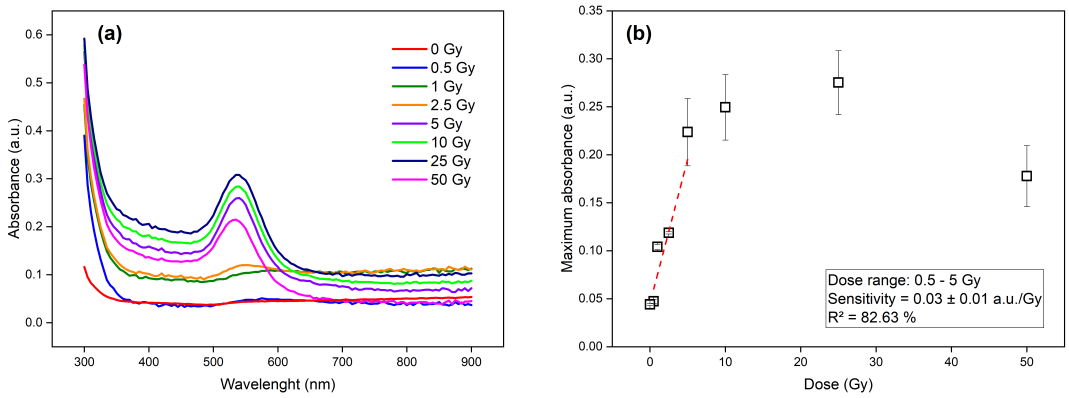

Figure 59 – (a) UV-vis spectra of the nanoparticles, for each dose; (b) Absorbance as a function of dose

Figure 60 present the size distribution for each dispersion (i.e., for each dose), obtained with DLS measurements.

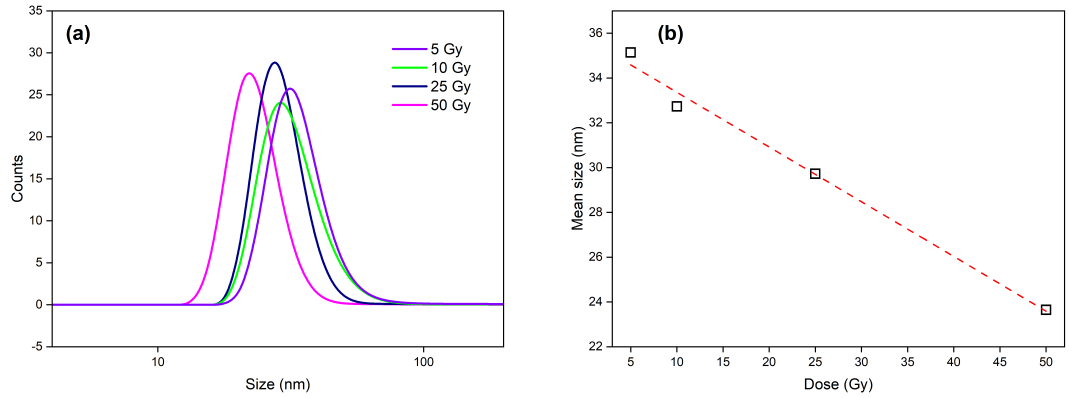

Figure 60 – (a) Size distribution of the nanoparticles produced, for each dose, on the Magnum source; (b) Variation of mean size with the dose

Figure 60 confirms that, in fact, nanoparticles size did not significantly change as a function of dose, in agreement with the UV-vis results. The average size is confined in a 10 nm interval and, even with a approximately linear relationship, this variation is not

significant, since the bands width are on the same order. The size distributions for doses lower than 5 Gy are not presented but also did not constitute any relationship with the dose. This suggests that the average size of the nanoparticles produced on this approach could be controlled only for doses higher than 5 Gy.

5.4.2 Dosimetry with the beam from the Titan x-ray tube

As the 160 kVp beam provided the highest absorbance, it was the voltage chosen to construct the dose response curve. The dose was varied from 0 to 50 Gy. Figure 61 depicts a shift to lower wavelengths when the dose increases, evidencing the influence of the dose on the nanoparticles size distribution. However, linearity is compromised at higher doses. Therefore, the radiation dosimetry is possible only for doses up to 10 Gy, with saturation occurring for 25 and 50 Gy. The sensitivity is higher for this beam than for the obtained with the Magnum source (0.07 versus 0.03 a.u./Gy), probably due to the higher dose rate.

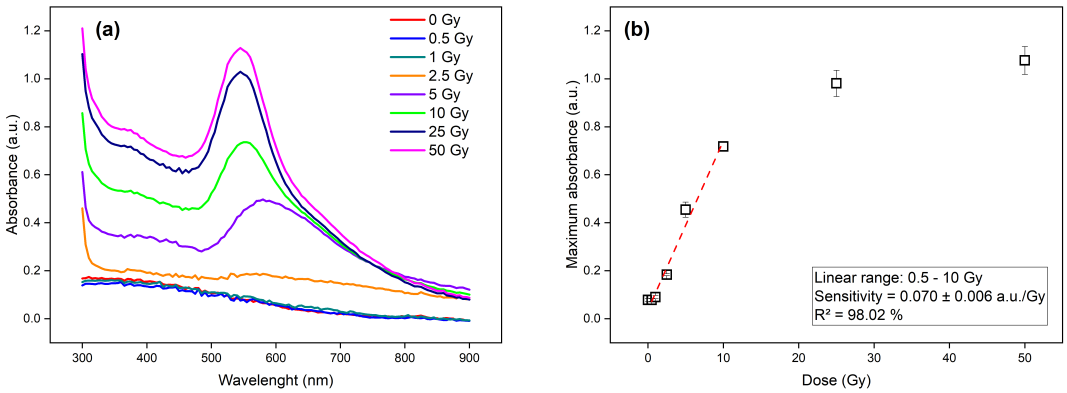

Figure 61 – (a) Absorption spectra of the nanoparticles, for each dose, on the industrial tube; (b) Maximum absorbance for each dose

Figure 62 indicates that the size of the nanoparticles actually changes when they are irradiated with different doses. Again, the size variation for the lower doses did not vary in a correlated way. However, the mean size could be an alternative parameter to infer the radiation dose for the higher dose interval (10 to 50 Gy), although with a non-linear behavior, as seen in Figure 62(b).

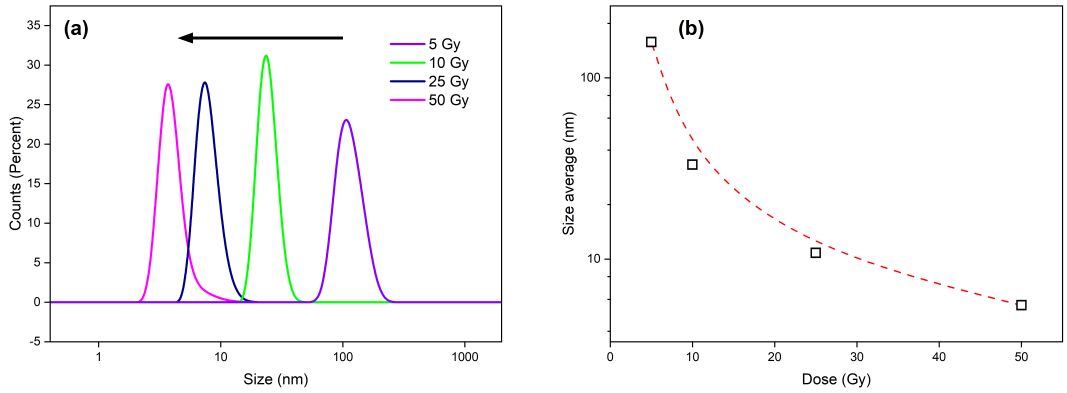

Figure 62 – (a) Size distribution of the nanoparticles produced, for each dose, on the Titan tube; (b) Variation of mean size with the dose

The variation for the Titan tube is notably higher than the obtained for the Magnum source. While the former has a variation on the order of 100 nm, the difference on the latter between the distributions for 5 and 5 Gy is approximately 10 nm. This suggests that, at the lower energy beam, the nucleation rate is not particularly affected by the total dose absorbed by the dispersion, while it plays a major hole for the higher energy beam. Thus, it seems that the Titan tube leads to more nanoparticles being synthesized. The absorbance for

5.5 Partial conclusions

The dosimeter based on the gold nanoparticles (AuNP) was developed inspired on a recent work (50). The chloroauric acid ($HAuCl_4$) was the gold precursor, ascorbic acid ($C_6H_8O_6$, or AA) was the reducing agent and CTAB was a template for the formation of the AuNP. The solution was mixed and irradiated at room temperature with doses up to 50 Gy. Firstly, the effectiveness of this approach was evaluated to x-rays, proving to be effective.

The next step consisted in verify the influence of the chemical and the irradiation parameters on the absorbance spectra and on the size distribution. The absorbance intensity was directly and the nanoparticle size inversely proportional to the concentration of both tested chemical components, which was attributed to a possible predominance of nucleation over growth. Thereafter, the synthesis was tested for other beam energies, confirming the previous analysis. As the voltage increases, the dose rate augments, generating more particles of smaller sizes, as pointed by the UV-vis (increased absorbance) and DLS (reducted particle size) results.

Finally, the dose response curve presented a linear behavior with the dose. However,

this linear tendency occurs only for doses up to 5 Gy, for the 48 kVp beam, with a sensitivity of 0.03 a.u./Gy, and up to 10 Gy for the 160 kVp beam, with 0.07 a.u./Gy sensitivity. This is an evidence of a tunable sensitivity according to the beam energy. More importantly, this result suggests that the inflection point of the dose response curve may be used to assess the radiation beam energy. Future experiments will be done to confirm this hypothesis. The size distribution of the nanoparticles was analyzed for doses from 5 to 50 Gy, being weakly changed by 48 kV beam, but strongly affected by the 160 kV beam, providing an alternative parameter to infer the radiation dose.

6

General conclusions

In this work, we investigated the application of nanoparticles for dosimetry of ionizing radiation and how the synthesis of these structures could be related to the absorbed dose during the process. We developed methods for synthesis of nanoparticles in which the radiation plays a key role to synthesize the particles. The main challenge was controlling the nanoparticle formation process in order to efficiently create conditions to allow that the radiation was the major factor of the synthesis while avoiding the early formation of the particles due to chemical reactions on the precursor solutions. Once we reached this control, the dosimeter could be developed. The dose dependence was established in terms of the surface plasmon resonance (SPR) band, characteristic of metal nanoparticles, such as gold and silver. Therefore, the main idea was to develop a dosimeter based on the reading of the absorbance intensity generated by the SPR phenomena.

The dosimeter based on silver nanoparticles (AgNP) was developed with silver nitrate as the metal precursor and trisodium citrate as the reducing agent. These reactants were used in a combination of one chemical and one radiolytic step. Three techniques for the combination of the chemical reaction with an additional irradiation process was developed, based on the presence of a heating and cooling processes during the chemical reaction. An absorption band at 420 nm was observed for irradiated samples produced by the three methods, which is characteristic of silver nanoparticles. The third method employed two microreactors to quickly heat and cool and allowed the best results: absent absorbance before irradiation and an intense signal after irradiation. This technique also provided the more sensitive dosimeter. The sensitivity did not change upon varying the tube voltage, indicating that the dosimeter could be viable to beam energies commonly used in clinic applications.

A unexpected result with the microfluidic approach was the possibility of dose assessment with silver nanoclusters besides the silver nanoparticles. The nanoclusters are probably the intermediate state before the silver nanoparticle growth, and was only observed when the microfluidic synthesis was used. They were formed for low doses (up to

2.5 Gy) and provided two ways to infer the radiation dose: by absorption spectroscopy, due SPR, and by fluorescence spectroscopy, due to internal electronic transitions in the clusters.

The dosimeter based on the gold nanoparticles (AuNP) was developed with chloroauric acid as the gold precursor, ascorbic acid (AA) as the reducing agent and CTAB as a template for the formation of the AuNP. The solution was mixed and irradiated at room temperature with doses up to 50 Gy. The technique proved to be effective, with the ascorbic acid being a major factor. Then we turned to verify the influence of the chemical and irradiation parameters on the absorbance spectra and on the size distribution. The observed behavior was attributed to the generation of a lot of seeds, which compete against the growth of the already formed clusters. Then, the synthesis was tested for other beam energies, in which our previous analysis was confirmed. The increase on tube voltage, for a given dose, led to an increase on the absorbance intensity accompanied by a decrease on the mean size of the particles, by favoring the nucleation over the growth. Once the synthesis was studied, the dosimeter based on absorbance intensity was developed. The signal increased linearly with the dose, indicating more nanoparticle formation. We have found an evidence of a tunable sensitivity according to the energy of the beam, which may be accounted in order to achieve a good measurement. The size distribution of the nanoparticles was analyzed for doses from 5 to 50 Gy. Its value is weakly changed by the 48 kV beam, but strongly affected by the 160 kV one, providing an alternative way to measure dose with this approach.

References

1 KREIBIG, U. *Optical Properties of Metal Clusters*. 1st. ed. [S.l.]: Springer, 1995.

2 SUGIMOTO, T. Underlying mechanisms in size control of uniform nanoparticles. *Journal of Colloid and Interface Science*, v. 309, n. 1, p. 106–118, 2007. ISSN 00219797.

3 BERGER, M. et al. *XCOM: Photon Cross Section Database (version 1.5)*. [S.l.]: http://physics.nist.gov/xcom, 2010.

4 XU, H. et al. Dosimetric effects of the kV based image-guided radiation therapy of prone breast external beam radiation: Towards the optimized imaging frequency. *Journal of Applied Clinical Medical Physics*, v. 20, n. 1, p. 212–219, 2019. ISSN 15269914.

5 BREITKREUTZ, D. Y.; WEIL, M. D.; BAZALOVA-CARTER, M. External beam radiation therapy with kilovoltage x-rays. *Physica Medica*, Elsevier Ltd, v. 79, n. July, p. 103–112, 2020. ISSN 1724191X. Disponível em: <https://doi.org/10.1016/j.ejmp.2020.11.001>.

6 HILL, R. et al. Advances in kilovoltage x-ray beam dosimetry. *Physics in Medicine and Biology*, v. 59, n. 6, 2014. ISSN 13616560.

7 MA, C. M. et al. AAPM protocol for 40-300 kV x-ray beam dosimetry in radiotherapy and radiobiology. *Medical Physics*, v. 28, n. 6, p. 868–893, 2001. ISSN 00942405.

8 ANDREO, P. Data for the dosimetry of low- A nd medium-energy kV x rays. *Physics in Medicine and Biology*, IOP Publishing, v. 64, n. 20, 2019. ISSN 13616560.

9 AUSTERLITZ, C. de et al. The use of fricke dosimetry for low energy x-rays. *Brazilian Archives of Biology and Technology*, v. 49, n. spe, p. 17–23, 2006. ISSN 1516-8913.

10 EBERT, M. A.; ASAD, A. H.; SIDDIQUI, S. A. Suitability of radiochromic films for dosimetry of low energy X-rays. *Journal of Applied Clinical Medical Physics*, v. 10, n. 4, p. 232–240, 2009. ISSN 15269914.

11 MCMANUS, M. et al. The challenge of ionisation chamber dosimetry in ultra-short pulsed high dose-rate Very High Energy Electron beams. *Scientific Reports*, v. 10, n. 1, p. 1–11, 2020. ISSN 20452322.

12 NASCIMENTO, C. R. et al. The performance of a multi guard ring (MGR) diode for clinical electron beams dosimetry. *Applied Radiation and Isotopes*, Elsevier Ltd, v. 141, n. July 2017, p. 112–117, 2018. ISSN 18729800. Disponível em: <https://doi.org/10.1016/j.apradiso.2018.07.002>.

13 IKI, N. Silver nanoparticles. *Analytical Sciences*, v. 34, n. 11, p. 1223–1224, 2018. ISSN 13482246.

References

14 EPIFANI, M. et al. Sol ? Gel Synthesis and Characterization of Ag and Au Nanoparticles in. *J. Am. Ceram. Soc*, v. 83, n. 10, p. 2385–2393, 2000. ISSN 00027820.

15 KING, J. G. et al. Magnetic properties of magnetite arrays produced by the method of electron beam lithography. *Geophysical Research Letters*, v. 23, n. 20, p. 2847–2850, 1996. ISSN 00948276.

16 REDDY, L. H. et al. Magnetic nanoparticles: Design and characterization, toxicity and biocompatibility, pharmaceutical and biomedical applications. *Chemical Reviews*, v. 112, n. 11, p. 5818–5878, 2012. ISSN 00092665.

17 GRAMMATIKOPOULOS, P. et al. Nanoparticle design by gas-phase synthesis. *Advances in Physics: X*, Taylor & Francis, v. 1, n. 1, p. 81–100, 2016. ISSN 23746149. Disponível em: <http://dx.doi.org/10.1080/23746149.2016.1142829>.

18 MURTY, B. S. *Textbook of Nanoscience and Nanotechnology*. 1st. ed. [S.l.]: Springer, 2013.

19 SHAW, D. J. *Introduction to Colloid and Surface Chemistry*. 4th. ed. [S.l.]: Elsevier Science, 1992.

20 THANH, N. T.; MACLEAN, N.; MAHIDDINE, S. Mechanisms of nucleation and growth of nanoparticles in solution. *Chemical Reviews*, v. 114, n. 15, p. 7610–7630, 2014. ISSN 15206890.

21 SOLOMON, S. D. et al. Synthesis and study of silver nanoparticles. *Journal of Chemical Education*, v. 84, n. 2, p. 322–325, 2007. ISSN 00219584.

22 HUANG, Z. et al. Continuous synthesis of size-tunable silver nanoparticles by a green electrolysis method and multi-electrode design for high yield. *Journal of Materials Chemistry A*, Royal Society of Chemistry, v. 3, n. 5, p. 1925–1929, 2015. ISSN 20507496. Disponível em: <http://dx.doi.org/10.1039/C4TA06782G>.

23 ABID, J. P. et al. Preparation of silver nanoparticles in solution from a silver salt by laser irradiation. *Chemical Communications*, v. 7, p. 792–793, 2002. ISSN 13597345.

24 FUNARO, M. et al. Dosimeter based on silver-nanoparticle precursors for medical applications with linear response over a wide dynamic range. *Micro and Nano Letters*, v. 6, n. 9, p. 759–762, 2011. ISSN 17500443.

25 TUKEVICH, J.; STEVENSON, P. C.; HILLIER, J. A study of the nucleation and growth processes in the synthesis of colloidal gold. *Discussions of the Faraday Society*, v. 55, n. 03, p. 55–75, 2014.

26 PILLAI, Z. S.; KAMAT, P. V. What factors control the size and shape of silver nanoparticles in the citrate ion reduction method? *Journal of Physical Chemistry B*, v. 108, n. 3, p. 945–951, 2004. ISSN 15206106.

27 KUMAR, S.; GANDHI, K. S.; KUMAR, R. Modeling of formation of gold nanoparticles by citrate method. *Industrial and Engineering Chemistry Research*, v. 46, n. 10, p. 3128–3136, 2007. ISSN 08885885.

28 SUN, K. et al. Preparation and characterization of gold nanoparticles using ascorbic acid as reducing agent in reverse micelles. *Journal of Materials Science*, v. 44, n. 3, p. 754–758, 2009. ISSN 00222461.

29 HUANG, D. et al. One-pot synthesis of dendritic gold nanostructures in aqueous solutions of quaternary ammonium cationic surfactants: Effects of the head group and hydrocarbon chain length. *ACS Applied Materials and Interfaces*, v. 4, n. 9, p. 4665–4671, 2012. ISSN 19448244.

30 ABEDINI, A. et al. A review on radiation-induced nucleation and growth of colloidal metallic nanoparticles. *Nanoscale Research Letters*, v. 9, p. 474–483, 2013.

31 WALKER, C. R. et al. Generation of polypeptide-templated gold nanoparticles using ionizing radiation. *Langmuir*, v. 29, n. 32, p. 10166–10173, 2013. ISSN 07437463.

32 PUIŠO, J. et al. Liquid radiation detectors based on nanosilver surface plasmon resonance phenomena. *Radiation Protection Dosimetry*, v. 139, n. 1-3, p. 353–356, 2010. ISSN 01448420.

33 KHARISOV, B.; KHARISSOVA, O.; MENDEZ, U. O. *Radiation Synthesis of Materials and Compounds*. [S.l.]: CRC Press, 2013. ISBN 9780429112669.

34 BELLONI, J. Metal nanocolloids. *Current Opinion in Colloid & Interface Science*, Current Science Ltd., v. 1, n. 2, p. 184–196, 1996. ISSN 13590294. Disponível em: <http://dx.doi.org/10.1016/S1359-0294(96)80003-3>.

35 HENGLEIN, A. Physicochemical properties of small metal particles in solution: "microelectrode" reactions, chemisorption, composite metal particles and the atom-to-metal transition. *The Journal of Physical Chemistry*, v. 97, n. 21, p. 5457–5471, 1993.

36 MARIGNIER, J. L. et al. Microaggregates of non-noble metals and bimetallic alloys prepared by radiation-induced reduction. *Nature*, v. 317, n. 6035, p. 344–345, 1985. ISSN 00280836.

37 BELLONI, J. Nucleation, growth and properties of nanoclusters studied by radiation chemistry: Application to catalysis. *Catalysis Today*, v. 113, n. 3-4, p. 141–156, 2006. ISSN 09205861.

38 SONG, Y.; HORMES, J.; KUMAR, C. S. Microfluidic synthesis of nanomaterials. *Small*, v. 4, n. 6, p. 698–711, 2008. ISSN 16136810.

39 ZHAO, C. X. et al. Nanoparticle synthesis in microreactors. *Chemical Engineering Science*, Elsevier, v. 66, n. 7, p. 1463–1479, 2011. ISSN 00092509. Disponível em: <http://dx.doi.org/10.1016/j.ces.2010.08.039>.

40 EDEL, J. B. et al. Microfluidic routes to the controlled production of nanoparticles. *Chemical Communications*, v. 2, n. 10, p. 1136–1137, 2002. ISSN 1364548X.

41 XU, L. et al. Droplet synthesis of silver nanoparticles by a microfluidic device. *Chemical Engineering and Processing: Process Intensification*, Elsevier B.V., v. 102, p. 186–193, 2016. ISSN 02552701. Disponível em: <http://dx.doi.org/10.1016/j.cep.2016.01.017>.

42 WAGNER, J.; KÖHLER, J. M. Continuous synthesis of gold nanoparticles in a microreactor. *Nano Letters*, v. 5, n. 4, p. 685–691, 2005. ISSN 15306984.

References

43 PATIL, G. A. et al. Continuous synthesis of functional silver nanoparticles using microreactor: Effect of surfactant and process parameters. *Chemical Engineering and Processing: Process Intensification*, Elsevier B.V., v. 62, p. 69–77, 2012. ISSN 02552701. Disponível em: <http://dx.doi.org/10.1016/j.cep.2012.09.007>.

44 LAZARUS, L. L. et al. Two-phase microfluidic droplet flows of ionic liquids for the synthesis of gold and silver nanoparticles. *ACS Applied Materials and Interfaces*, v. 4, n. 6, p. 3077–3083, 2012. ISSN 19448244.

45 BABER, R. et al. Synthesis of silver nanoparticles in a microfluidic coaxial flow reactor. *RSC Advances*, v. 5, n. 116, p. 95585–95591, 2015. ISSN 20462069.

46 EDGAR, J. A. et al. Formation of Gold Nanorods by a Stochastic ? Popcorn ? Mechanism. *ACSNano*, n. 2, p. 1116–1125, 2012.

47 CLIFFORD, D. M.; CASTANO, C. E.; ROJAS, J. V. Supported transition metal nanomaterials : Nanocomposites synthesized by ionizing radiation. *Radiation Physics and Chemistry*, v. 132, p. 52–64, 2017.

48 ANANDHAKUMAR, S.; RAJARAM, R.; MATHIYARASU, J. Unusual seedless approach to gold nanoparticle synthesis : application to selective rapid naked eye. *Analyst*, n. 139, p. 3356–3359, 2014.

49 JANA, N. R. et al. Seeding Growth for Size Control of 5 - 40 nm Diameter Gold Nanoparticles. *Langmuir*, n. 17, p. 6782–6786, 2001.

50 PUSHPAVANAM, K. et al. A Colorimetric Plasmonic Nanosensor for Dosimetry of Therapeutic Levels of Ionizing Radiation. *ACS Nano*, v. 9, n. 12, p. 11540–11550, 2015. ISSN 1936086X.

51 GHOSH, S. K.; PAL, T. Interparticle coupling effect on the surface plasmon resonance of gold nanoparticles: From theory to applications. *Chemical Reviews*, v. 107, n. 11, p. 4797–4862, 2007. ISSN 00092665.

52 HORVATH, H. Gustav Mie and the scattering and absorption of light by particles: Historic developments and basics. *Journal of Quantitative Spectroscopy and Radiative Transfer*, v. 110, n. 11, p. 787–799, 2009. ISSN 00224073.

53 BONAČIĆ-KOUTECKÝ, V.; KOUTECKÝ, J.; FANTUCCI, P. Quantum Chemistry of Small Clusters of Elements of Groups Ia, Ib, and IIa: Fundamental Concepts, Predictions, and Interpretation of Experiments. *Chemical Reviews*, v. 91, n. 5, p. 1035–1108, 1991. ISSN 15206890.

54 KOLWAS, K.; DERKACHOVA, A.; SHOPA, M. Size characteristics of surface plasmons and their manifestation in scattering properties of metal particles. *Journal of Quantitative Spectroscopy and Radiative Transfer*, Elsevier, v. 110, n. 14-16, p. 1490–1501, 2009. ISSN 00224073. Disponível em: <http://dx.doi.org/10.1016/j.jqsrt.2009.03.020>.

55 OLSON, J. et al. Optical characterization of single plasmonic nanoparticles. *Chemical Society Reviews*, v. 44, n. 1, p. 40–57, 2015. ISSN 14604744.

56 MARETTI, L. et al. Facile photochemical synthesis and characterization of highly fluorescent silver nanoparticles. *Journal of the American Chemical Society*, v. 131, n. 39, p. 13972–13980, 2009. ISSN 00027863.

References

57 XIE, Y. P. et al. Silver nanoclusters: Synthesis, structures and photoluminescence. *Materials Chemistry Frontiers*, v. 4, n. 8, p. 2205–2222, 2020. ISSN 20521537.

58 FERNANDO, A. et al. Quantum Mechanical Studies of Large Metal, Metal Oxide, and Metal Chalcogenide Nanoparticles and Clusters. *Chemical Reviews*, v. 115, n. 12, p. 6112–6216, 2015. ISSN 15206890.

59 MAITY, S.; BAIN, D.; PATRA, A. An overview on the current understanding of the photophysical properties of metal nanoclusters and their potential applications. *Nanoscale*, Royal Society of Chemistry, v. 11, n. 47, p. 22685–22723, 2019. ISSN 20403372.

60 DU, Y. et al. Atomically Precise Noble Metal Nanoclusters as Efficient Catalysts: A Bridge between Structure and Properties. *Chemical Reviews*, v. 120, n. 2, p. 526–622, 2020. ISSN 15206890.

61 YUAN, X. et al. Glutathione-protected silver nanoclusters as cysteine-selective fluorometric and colorimetric probe. *Analytical Chemistry*, v. 85, n. 3, p. 1913–1919, 2013. ISSN 00032700.

62 Le Guével, X. et al. Highly fluorescent silver nanoclusters stabilized by glutathione: A promising fluorescent label for bioimaging. *Nano Research*, v. 5, n. 6, p. 379–387, 2012. ISSN 19980000.

63 ASHENFELTER, B. A. et al. Fluorescence from Molecular Silver Nanoparticles. *Journal of Physical Chemistry C*, v. 119, n. 35, p. 20728–20734, 2015. ISSN 19327455.

64 DESIREDDY, A. et al. Ultrastable silver nanoparticles. *Nature*, Nature Publishing Group, v. 501, n. 7467, p. 399–402, 2013. ISSN 00280836. Disponível em: <http://dx.doi.org/10.1038/nature12523>.

65 QIAN, H. et al. Quantum sized gold nanoclusters with atomic precision. *Accounts of Chemical Research*, v. 45, n. 9, p. 1470–1479, 2012. ISSN 00014842.

66 YAU, S. H. et al. Ultrafast optical study of small gold monolayer protected clusters: A closer look at emission. *Journal of Physical Chemistry C*, v. 114, n. 38, p. 15979–15985, 2010. ISSN 19327447.

67 PELTON, M. et al. Long-lived charge-separated states in ligand-stabilized silver clusters. *Journal of the American Chemical Society*, v. 134, n. 29, p. 11856–11859, 2012. ISSN 00027863.

68 WU, Z.; JIN, R. On the ligand's role in the fluorescence of gold nanoclusters. *Nano Letters*, v. 10, n. 7, p. 2568–2573, 2010. ISSN 15306984.

69 PETTY, J. T. et al. DNA-Templated Ag Nanocluster Formation. *Journal of the American Chemical Society*, v. 126, n. 16, p. 5207–5212, 2004. ISSN 00027863.

70 SHANG, L.; DONG, S. Facile preparation of water-soluble fluorescent silver nanoclusters using a polyelectrolyte template. *Chemical Communications*, n. 9, p. 1088–1090, 2008. ISSN 13597345.

71 NARAYANAN, S. S.; PAL, S. K. Structural and functional characterization of luminescent silver - protein nanobioconjugates. *Journal of Physical Chemistry C*, v. 112, n. 13, p. 4874–4879, 2008. ISSN 19327447.

72 RICHARDS, C. I. et al. Oligonucleotide-stabilized Ag nanocluster fluorophores. *Journal of the American Chemical Society*, v. 130, n. 15, p. 5038–5039, 2008. ISSN 00027863.

73 JAIN, P. K. et al. Calculated absorption and scattering properties of gold nanoparticles of different size, shape, and composition: Applications in biological imaging and biomedicine. *Journal of Physical Chemistry B*, v. 110, n. 14, p. 7238–7248, 2006. ISSN 15206106.

74 ESTRADA-MENDOZA, T. A.; WILLETT, D.; CHUMANOV, G. Light Absorption and Scattering by Silver/Silver Sulfide Hybrid Nanoparticles. *Journal of Physical Chemistry C*, v. 124, n. 49, p. 27024–27031, 2020. ISSN 19327455.

75 LINK, S.; EL-SAYED, M. A. Spectral Properties and Relaxation Dynamics of Surface Plasmon Electronic Oscillations in Gold and Silver Nanodots and Nanorods. *Journal of Physical Chemistry B*, v. 103, n. 40, p. 8410–8426, 1999. ISSN 15206106.

76 LINK, S.; EL-SAYED, M. A. *International Reviews in Physical Chemistry Shape and size dependence of radiative , non- radiative and photothermal properties of gold nanocrystals*. [S.l.]: International Reviews in Physical Chemistry Shape and size dependence of radiative, 2010. ISBN 0144235005.

77 PLATT, U. et al. *Differential Optical Absorption Spectroscopy*. [S.l.]: Springer, 2008. v. 174. 135–174 p. ISBN 9783540757764.

78 Senthil Kumar, P.; Grace Pavithra, K.; NAUSHAD, M. *Characterization techniques for nanomaterials*. Elsevier Inc., 2019. 97–124 p. ISBN 9780128133378. Disponível em: <http://dx.doi.org/10.1016/B978-0-12-813337-8.00004-7>.

79 CHIRAYIL, C. J. et al. *Instrumental Techniques for the Characterization of Nanoparticles*. Elsevier Inc., 2017. v. 3. 1–36 p. ISBN 9780323461450. Disponível em: <http://dx.doi.org/10.1016/B978-0-323-46139-9.00001-3>.

80 PALCHOUDHURY, S.; BAALOUSHA, M.; LEAD, J. R. *Methods for Measuring Concentration (Mass, Surface Area and Number) of Nanomaterials*. Elsevier, 2015. v. 8. 153–181 p. ISSN 1876276X. ISBN 9780080999487. Disponível em: <http://dx.doi.org/10.1016/B978-0-08-099948-7.00005-1>.

81 HARB, M. et al. Optical absorption of small silver clusters: Agn, (n=4-22). *Journal of Chemical Physics*, v. 129, n. 19, 2008. ISSN 00219606.

82 HENGLEIN, A.; MULVANEY, P.; LINNERT, T. Chemistry of Ag, Aggregates in Aqueous Solution: Non-metallic Oligomeric Clusters and Metallic Particles . *Faraday Discussions*, n. 92, p. 31–44, 1991.

83 TREGUER, M. et al. Fluorescent silver oligomeric clusters and colloidal particles. *Solid State Sciences*, v. 7, n. 7, p. 812–818, 2005. ISSN 12932558.

84 DONTJE, M. L. et al. Reliability, minimal detectable change and responsiveness to change: Indicators to select the best method to measure sedentary behaviour in older adults in different study designs. *PLoS ONE*, v. 13, n. 4, p. 1–16, 2019. ISSN 19326203.

85 OVEREND, T. et al. Relative and absolute reliability of physical function measures in people with end-stage renal disease. *Physiotherapy Canada*, v. 62, n. 2, p. 122–128, 2010. ISSN 03000508.

86 RIES, J. D. et al. Test-Retest Reliability and Minimal Detectable Change Scores for the Timed Up and Go Test, the Six-Minute Walk Test, and Gait Speed in People With Alzheimer Disease. *Physical Therapy and Rehabilitation Journal*, v. 89, n. 6, p. 569–579, 2009.

87 STRANIK, O. et al. Optimization of nanoparticle size for plasmonic enhancement of fluorescence. *Plasmonics*, v. 2, n. 1, p. 15–22, 2007. ISSN 15571955.

88 SWIFT, J. L.; CRAMB, D. T. Nanoparticles as fluorescence labels: Is size all that matters? *Biophysical Journal*, v. 95, n. 2, p. 865–876, 2008. ISSN 15420086.

89 LIU, C. et al. Preparation of silver nanoparticle and its application to the determination of ct-DNA. *Sensors*, v. 7, n. 5, p. 708–718, 2007. ISSN 14248220.

90 BOURHIS, K. et al. Femtosecond laser structuring and optical properties of a silver and zinc phosphate glass. *Journal of Non-Crystalline Solids*, v. 356, n. 44-49, p. 2658–2665, 2010. ISSN 00223093.

91 BELHAROUAK, I. et al. Silver aggregates in photoluminescent phosphate glasses of the 'Ag2O-ZnO-P2O5' system. *Journal of Non-Crystalline Solids*, v. 244, n. 2, p. 238–249, 1999. ISSN 00223093.

92 KUMBHAR, A. S.; KINNAN, M. K.; CHUMANOV, G. Multipole plasmon resonances of submicron silver particles. *Journal of the American Chemical Society*, v. 127, n. 36, p. 12444–12445, 2005. ISSN 00027863.

93 AMENDOLA, V.; BAKR, O. M.; STELLACCI, F. A study of the surface plasmon resonance of silver nanoparticles by the discrete dipole approximation method: Effect of shape, size, structure, and assembly. *Plasmonics*, v. 5, n. 1, p. 85–97, 2010. ISSN 15571955.

94 GUIDELLI, E. J. et al. Microwave-Assisted Growth of Silver Nanoparticle Films with Tunable Plasmon Properties and Asymmetrical Particle Geometry for Applications as Radiation Sensors. *Plasmonics*, Plasmonics, v. 15, n. 6, p. 1551–1564, 2020. ISSN 15571963.

95 GUIDELLI, E. J.; RAMOS, A. P.; BAFFA, O. Optically Stimulated Luminescence Under Plasmon Resonance Conditions Enhances X-Ray Detection. *Plasmonics*, v. 9, n. 5, p. 1049–1056, 2014. ISSN 15571963.

96 La Spina, R. et al. Synthesis of citrate-stabilized silver nanoparticles modified by thermal and ph preconditioned tannic acid. *Nanomaterials*, v. 10, n. 10, p. 1–16, 2020. ISSN 20794991.

97 C. Martínez, J. et al. Alternative Metodology for Gold Nanoparticles Diameter Characterization Using PCA Technique and UV-VIS Spectrophotometry. *Nanoscience and Nanotechnology*, v. 2, n. 6, p. 184–189, 2013. ISSN 2163-257X.

98 HAISS, W. et al. Determination of Size and Concentration of Gold Nanoparticles from UV - Vis Spectra. *Analytical Chemistry*, v. 79, n. 11, p. 4215–4221, 2007.